Engineering the Cardiac Fuel Supply:
Elevation of 2-deoxy-ATP for Myofilament-Targeted Treatment of Heart Failure

Sarah G. Nowakowski

A dissertation
submitted in partial fulfillment of the
requirements for the degree of

Doctor of Philosophy

University of Washington
2014

Reading Committee:
Michael Regnier, Chair
Valerie Daggett
Charles E. Murry

Program Authorized to Offer Degree:
Bioengineering
University of Washington

University of Washington

Abstract

Engineering the Cardiac Fuel Supply:
Elevation of 2-deoxy-ATP for Myofilament-Targeted Treatment of Heart Failure

Sarah G. Nowakowski

Chair of the Supervisory Committee:
Professor Michael Regnier
Bioengineering

Heart failure is a syndrome characterized by the inability of the heart to fill with, or eject, blood. There are many causes of heart failure including toxins (e.g. alcohol, chemotherapy), inherited cardiomyopathies, viral infections, and coronary artery disease. All of these conditions can impair left ventricular function, which initiates a cascade of compensatory events as the heart attempts to maintain cardiac output. While initially beneficial, these compensatory responses eventually become maladaptive, and ultimately lead to heart failure. Because the majority of patients with heart failure have impaired systolic dysfunction that initiates the cycle of decompensation, therapeutic approaches to prevent or reverse heart failure are aimed at improving left ventricular function. Despite advances in therapy, however, the five-year mortality for heart failure is ~50%. In an effort to increase the contractility of myocardium and improve left ventricular function, we propose novel, myofilament-targeted inotrope to treat heart failure. Using reductionist techniques, we have shown that dATP is a more effective substrate than ATP for contraction of cardiac muscle, increasing force and the rate of force development. Our biochemical and mechanical analysis suggests that dATP increases the rates of myosin binding and product release, translating to enhanced contractility and, perhaps, relaxation. This project spans from molecular mechanisms to translational research, determining how dATP improves myosin function and how this translates to improved cardiac function in normal and damaged hearts. The research presented in this dissertation (1) characterizes the effects of increased dATP in vivo on cardiac function in both normal hearts and those following injury (myocardial infarction), and (2) details the effects of dATP binding on the structure of myosin, which elucidates a molecular mechanism by which increased dATP concentration results in contractile enhancements. Life-long elevation of [dATP] in transgenic mice and cardiac-specific, viral-mediated elevation in [dATP] overexpression increased performance in healthy mice *ex vivo*. The performance improvement in healthy mice motivated us to examine the therapeutic potential of RR overexpression in an infarct model. Preliminary

echocardiography measurements showed that AAV-mediated RR overexpression improved *in vivo* performance in infarcted mice. MD simulations of myosin in the showed that dADP.Pi altered the conformation of the nucleotide binding pocket, the cleft, and the actin binding surface on myosin, stabilizing a conformation of myosin that binds actin more favorably than the stable conformation of myosin bound to ADP.Pi. These studies provide a potential mechanism that underlies the dATP-mediated increase in contractility observed. Elevating cardiac dATP may be a viable therapy to improve performance in patients suffering systolic dysfunction. This approach is being commercialized and pre-clinical, large animal studies are underway.

TABLE OF CONTENTS

LIST OF FIGURES

LIST OF TABLES

ACKNOWLEDGEMENTS

A number of people contributed significant time and effort to completing the work presented here. First, I would like to sincerely thank my advisor, Dr. Michael Regnier. His mentorship, support, and guidance enabled me to succeed, and I value the impact that Mike has had on me as an individual, as a leader, and as a scientist. I would also like to thank the other members of my supervisory committee, Valerie Daggett, Charles Murry, and William Mahoney. I appreciate all of their mentorship and their contributions to this work.

I had the privilege of collaborating with a number of incredible scientists, and am tremendously grateful for their work. In particular, I would like to thank Masha Razumova, Galina Flint, Charles Luo, Farid Moussavi-Harami, and Steve Korte. They took a lot of time to teach me how to perform more rigorous research, to think critically, and to ask good questions. I would like to thank them for the hours they spent helping me complete studies and talking through problems with me. I have learned so much from each of them, and cannot imagine life in the HAMM Lab without them. I would also like to thank all of the other HAMMies who have passed through the lab over the past six years for their support, for sharing their knowledge with me, and for making me laugh. I would also like to thank a number of collaborators from other labs around UW. Specifically, I would like to acknowledge the contributions of Guy Odom, Steve Kolwicz, Sarah Dupras, Amy Martinson, and Anna Naumova. I greatly appreciate the time they spent contributing to this body of work, and for all of the questions they have answered. I admire them all as people and as scientists. I would like to thank the Daggett Lab for welcoming me into the group. Their support enabled me to extend my knowledge into a new field. I would especially like to thank Michelle McCully, Claire-Louise Towse, Jonathan Cheng, Denny Bromley, Steve Rysavy, and Gene Hopping for answering so many of my questions.

Finally, I would like to thank my family and friends for their endless support and love. My parents, Ken and Lisa Nowakowski, taught me the importance of being curious, asking questions, and learning every day. I also learned from them how to work hard for success. They provide an amazing example and inspire me to achieve great things. I look up to both of them and am so thankful for all that I have learned from them. I would also like to acknowledge my brother, Sam, who has always encouraged me to be better and can always make me laugh. Thank you for being there. I would specifically like to thank two friends, Eryn Gallagher and Crissy Haley. They have been by my side throughout, have given so much advice, and have never stopped cheering me on. Lastly, I would like to thank my fiancée, Jeff Chamberlain. Jeff has taught me to appreciate all that I have and to be present, and has shown me that I have so much to be thankful for. His drive inspires me, he challenges me, and he makes me better. I am incredibly grateful for all that Jeff has done to support me throughout graduate school, and I can't wait for all that lies ahead.

DEDICATION

To Tessa

You inspire me to learn more, to be a better person, and to smile often. I admire how you cherished every day; you showed me how to be passionate about gaining knowledge, how to love and care for friends and family, and how important it is to laugh. I miss you always, but I am so grateful for all that you have taught me and for the time we had together. Love you forever, Beaner.

CHAPTER 1. INTRODUCTION

1.1 Problem Statement

Cardiovascular disease is the leading cause of morbidity and mortality worldwide, contributing to 30% of deaths in 2008 [1]. Heart failure, the most severe manifestation of cardiovascular disease affects approximately 6 million people in the United States, and approximately 500,000 new cases are diagnosed each year [2, 3]. Heart failure is the most common diagnosis of hospitalized patients over 65 and accounts for over 12M medical office visits each year [3]. As such, the estimated direct and indirect medical costs of heart failure were estimated to be $34.4B in the U.S. alone, an economic burden that is predicted to increase to $55.9B by 2020 [4].

Heart failure is a syndrome characterized by the inability of the heart to fill with, or eject, blood. There are many causes of heart failure including toxins (e.g. alcohol, chemotherapy), inherited cardiomyopathies, viral infections, and coronary artery disease. All of these conditions can impair left ventricular function, which initiates a cascade of compensatory events as the heart attempts to maintain cardiac output. While initially beneficial, these compensatory responses eventually become maladaptive, and ultimately lead to heart failure. Because the majority of patients with heart failure have impaired systolic dysfunction that initiates the cycle of decompensation, therapeutic approaches to prevent or reverse heart failure are aimed at improving left ventricular function. Despite advances in therapy, however, the five-year mortality for heart failure is ~50% [2, 5].

There are a number of approaches to improve left ventricular performance that are in different stages of development, including surgical intervention, regenerative therapy, and inotropic drugs. While the implantation of implantation of Left Ventricular Assist Devices (LVADs) or whole heart transplantation can successfully improve cardiac function, they are invasive and expensive, and serve only a small fraction of those patients suffering from heart failure. Several novel therapies to treat heart failure that are currently under development are focused on repairing damaged heart tissue using regenerative techniques. Both cell- and tissue- based therapies are being studied to assess the ability of implanted cells/tissue to incorporate into the host myocardium and regenerate viable cardiac tissue. There are significant challenges, however, that face the field of regenerative medicine such as achieving successful engraftment, cell survival, vascularization, coupling, and mature contraction of implanted material [6, 7]. Inotropic agents decrease filling pressures and increase cardiac output, and therefore they seem like

excellent candidates to treat patients with heart failure. However inotropes in current use have been shown to increase mortality [8, 9]. This lack of success is largely due to off-target effects associated with their mechanism of action, increasing intracellular calcium handling [10]. Presented here is work characterizing a novel, myofilament-targeted inotropic agent that improves contractility without increasing intracellular calcium.

1.2 Proposed Solution

In an effort to increase the contractility of myocardium, the Regnier lab has been investigating 2-deoxy ATP (dATP), an ATP analog used in DNA synthesis, and its ability to act as an energy substrate for myosin. The Regnier lab [11–14] and others [15–23] have shown that striated muscle myosin can use most naturally occurring nucleotides to support cross-bridge cycling and contraction to varying degrees. While most are not as effective as ATP, our lab has demonstrated that dATP is a more effective substrate than ATP for contraction of demembranated cardiac muscle, augmenting force and the rate of force development [14]. Our detailed biochemical and mechanical analysis suggests that dATP increases the rates of both myosin binding and product release (steps 2 and 3 in Figure 1.2), which in a cooperative system like the heart, translates to enhanced contractility [12].

More recently we reported that adenoviral-mediated overexpression of Ribonucleotide Reductase (RR), the enzyme that converts ADP to dADP (which is rapidly phosphorylated to become dATP), increases the dATP content in cultured adult and neonatal rat cardiomyocytes. This significantly enhanced the magnitude and rate of shortening and increased the rate of relaxation, without affecting the magnitude of intracellular Ca^{2+} transients [24]. This increase in contractile function was correlated with a ~10-fold increase in cellular dATP content. We also showed that this amount of dATP was sufficient to significantly increase force production of demembranated cardiac muscle at all levels of calcium measured [24]. These data suggest that dATP may be a viable therapy that could be used to improve cardiac performance in patients suffering systolic dysfunction.

1.2.1 Overall Hypothesis and Project Goals

In an effort to lay the groundwork for preclinical and clinical studies, the focus of my Ph.D. thesis is two-fold: (1) to characterize the effects of increased dATP *in vivo* on cardiac function in both normal hearts and those following injury (myocardial infarction), and (2) to determine the effects of dATP binding on the structure of myosin in order to elucidate a molecular mechanism by which increased dATP

concentration results in contractile enhancements. The research described in this dissertation details the studies performed to characterize the effects of elevated dATP on cardiac function in rat and mouse animal models as well as the development of Molecular Dynamics (MD) simulations used to examine the molecular mechanism by which dATP alters cardiac function. Based on our previous data that demonstrate this level of elevation of dATP is sufficient to increase contractile function *in vitro*, we hypothesize that chronic elevation of dATP concentration *in vivo* will result in persistent increases in cardiac function. Furthermore, on a molecular level, we hypothesize that there will be structural and dynamic alterations to both the nucleotide binding site and the actin binding surface that are induced by the binding of dADP.Pi (the hydrolysis products of dATP), and that these structural changes underlie the observed functional enhancements elicited by dATP. This hypothesis was investigated with two project goals that are outlined below.

Aim 1: Evaluation of the effects of elevated dATP concentration on normal and infarcted hearts.

We have previously demonstrated that an acute increase in dATP concentration (via RR overexpression) positively impacted contractility of cardiomyocytes *in vitro* (described in A.2 above) [24]. It is not clear, however, whether this elevated function would: (1) occur *in vivo,* (2) persist over the long-term (with or without compensation), (3) elicit negative effects on myocardial energetics and/or cardiac function, and (4) improve contractile performance in myocardium from injured or diseased hearts. This aim is focused on the characterization of the effects of dATP elevation *in vivo* in order to assess its therapeutic potential.

First, to determine whether dATP therapy would be clinically viable, we must demonstrate that its effectiveness can persist over time without pathological consequences. These studies will be the first describing an animal model with enhanced cardiomyocyte cross-bridge chemomechanical cycling via manipulation of the adenosine triphosphate nucleotide pool in healthy animals. We will use a transgenic mouse line developed by a collaborator, Robert Weiss, which globally overexpresses both the large (Rrm1) and small (Rrm2) subunits of RR (TgRR) as compared to their wild-type littermates (WT) [25]. Ylikallio *et al.* reported that skeletal muscle dATP content was increased approximately 10-fold in TgRR mice versus WT controls [25], which is similar to the level of elevation we achieved in cultured adult cardiomyocytes transduced with adenoviral vectors to elevate RR [24]. Based on our previous data that demonstrate this level of elevation of dATP is sufficient to increase contractile function *in vitro*, we hypothesize that chronic elevation of dATP concentration *in vivo* will result in persistent increases in

cardiac function. Furthermore, this unique model of persistent dATP elevation allows us to characterize the effect of chronic increases in cardiac contractility on baseline myocardial energetics as well as cardiac responsiveness to β-adrenergic stimulation. In this portion of Aim 1 (Chapter 2), we will use TgRR animals and characterize their *in vivo* and *in vitro* cardiac function, myocardial energetics, and cardiomyocyte contractile properties to assess the effect of chronic, global overexpression of RR (and thus increased dATP) on cardiac function. In addition to providing physiological insights into the effects of long-term RR overexpression, these studies allow for the characterization of any pathology or detrimental effects that are associated with chronic elevation in dATP, a necessary step to take before moving dATP toward the clinic.

In the second portion of this aim (Chapter 3 and Chapter 4), we will determine the therapeutic potential of elevated dATP concentration by virally overexpressing RR in the hearts of both healthy mice and those who have undergone myocardial infarction (MI). While our previous work *in vitro* used adenoviral-mediated overexpression of RR to elevate dATP concentration, in this aim, we will use an adeno-associated virus, AAV6-RR to overexpress RR and elevate dATP concentration *in vivo.* Adeno-associated viruses mediate long-term transgene expression [26], have high cardiac transfection efficiency [27, 28], and offer lower immunogenicity than adenovirus [26]. We hypothesize that delivery of AAV6-RR via systemic injection will significantly and reproducibly improve cardiac function following MI. For these studies we will administer virus systemically (retro-orbital injection) and follow animals via echocardiography to assess cardiac function. Mice that will get treated following MI will undergo permanent ligation of the left anterior descending (LAD) coronary artery prior to treatment. Virus will be administered four weeks following MI to ensure a depression in cardiac function prior to treatment. Cardiac function will be monitored *in vivo* for the duration of the study using echocardiography, and in the case of healthy animals, *ex vivo* at the end of the study using Langendorff perfused heart preparation. The work in this aim will provide critical information that will inform the path to pre-clinical, large animal experiments.

Aim 2: To determine atom-level differences in pre-powerstroke myosin structure and dynamics resulting from dADP.Pi (vs. ADP.Pi) binding that underlie dATP activation of myosin.

The Regnier lab has focused on studying both the chemomechanical effects of dATP on the cross-bridge cycle and the effect of dATP on the rate and magnitude of force production *in vitro*. While these data (described in 1.2 above) demonstrate the therapeutic potential of dATP, and provide insight into how dATP dramatically changes cross-bridge kinetics, little is known about the molecular mechanism by

which dATP effects these functional enhancements. The chemomechanical data offer insight as to where in the cross-bridge cycle the changes may occur (strong binding of myosin to actin/availability of "primed" myosin heads, as well as dADP release from myosin); and since myosin translates the chemical energy to the mechanical force through conformational changes, we expect that alterations in the myosin structure as a result of deoxy-nucleotide binding underlie the chemo-mechanical alterations. We hypothesize that there will be structural and dynamic alterations to both the nucleotide binding site and the actin binding surface that are induced by the binding of dADP.Pi (the hydrolysis products of dATP), and that these structural changes underlie the observed functional enhancements elicited by dATP.

The biochemical data [12] have informed us that cross-bridge attachment and detachment are the primary steps of the cross-bridge cycle affected by dATP binding. This work is focused on studying cross-bridge attachment, which is most dramatically altered by dATP binding [11–13] . As such, we have chosen to use Molecular Dynamics (MD) to simulate the pre-powerstroke state of myosin (which correlates to the myosin conformation during cross-bridge attachment) with Mg(d)ADP.Pi bound as the energetic substrate. A high-resolution x-ray crystallographic structure of myosin is used as starting structure, and is simulated with explicit solvent for 50 ns. Once simulated, analyses will be performed to assess: (1) how myosin interacts with the nucleotide in the binding pocket, (2) the chemistry of the actin binding surface on myosin, and (3) characterization of the allosteric modification that mediates changes to the actin binding surface.

These simulations will allow us to analyze the structure and dynamics of myosin with ADP vs. dADP in the pre-powerstroke state to determine how dADP alters the conformation of myosin to better understand the mechanism by which the deoxy nucelotide alters the cross-bridge cycle.

An additional set of simulations was performed on a mutated myosin bound to ADP.Pi to characterize the effects of a disease-linked mutation on the myosin conformation. The mutation selected, R397Q (correlates to R403Q in human myosin), is implicated in severe hypertrophic cardiomyopathy. Studies performed to analyze the cross-bridge cycling with this mutated myosin have demonstrated that while cross-bridge detachment is the primary rate affected by mutation, the rate of myosin attachment to actin is increased with this mutation [29]. Interestingly, the magnitude of this increased cross-bridge attachment is less than that induced by dATP binding. Thus, we are interested to examine the conformation of R397Q myosin vs. WT myosin bound to ADP as well as to WT myosin bound to dADP to

determine whether the conformation of myosin correlates with the functional parameters observed *in vitro*. Chapter 6 explores the simulations performed on mutated myosin bound to ADP and explores the relationship between myosin conformation and function.

1.3 Background and Significance

1.3.1 Heart Failure

Heart failure is most commonly the result of depressed left ventricular function [3], and can cause by conditions such as congenital disease, cardiomyopathy, viral infection, or a myocardial infarction (MI). In patients with impaired left ventricular function, a number of compensatory mechanisms are activated in order to maintain cardiac output and blood pressure: the Frank-Starling mechanism, neurohormonal compensation, and ventricular remodeling. Although these pathways are beneficial in the short term, chronic activation of these systems can have severely detrimental effects on cardiac performance. The Frank-Starling mechanism enables the heart to respond to increased end diastolic volume with increased stroke-volume, but this increase in stroke volume is only marginal in severe cases. Large increases end-diastolic volume and pressure can also lead to pulmonary congestion and edema. Neurohormonal responses such as, prolonged β-adrenergic activation increases intracellular calcium, decreases the heart's sensitivity to catecholamines, and eventually depletes energetic reserves, and chronic elevation of aldosterone and angiotensin II can result in adverse remodeling [3]. Remodeling of the ventricle can occur in response to alterations in hemodynamics to counteract increases in wall stress that are associated with heart failure. The pathway of remodeling can differ depending on the symptoms of failure (i.e. whether there is pressure or volume overload) and serve to maintain cardiac output in the short-term. Continued functional decline ultimately leads to dilation of the ventricle and continued deterioration into failure. Ultimately, formerly compensatory mechanisms eventually catapult the heart into a cycle of decompensation whereby the heart becomes unable to respond to increased demand. This dysfunction underlies the hearts inability to pump sufficient amounts of blood to the body.

The compensatory mechanisms described above are activated in an effort to improve cardiac output and blood supply to the body. As such, we hypothesize that therapies to improve cardiac function can prevent decompensation and can restore heart function to normal levels. By targeting the myofilament directly we aim to improve cardiac function without altering calcium handling, a novel approach to improve left ventricular function.

Limitations with current therapies

The most common treatment strategies used to treat patients with heart failure are pharmacologic and/or surgical. Each has significant limitations; while some pharmacological treatments can improve mortality, many are wrought with off-target effects [30]. In particular, currently used inotropic agents increase intracellular calcium levels, which can lead to adverse events such as cardiac ischemia, arrhythmia, or remodeling [10, 31]. Surgical treatments can ultimately improve cardiac function, but they are invasive and only serve a small fraction of the patient population suffering from heart failure [32, 33].

Cell- and tissue-based therapies that are currently in development focus on implanting donor cells into injured myocardium to promote wound healing and regeneration of damaged/dead heart tissue with the goal of improving cardiac function. These therapies face challenges of integration with the host: surviving in an avascular environment, electrically coupling, maturing, and producing meaningful amounts of force that can improve overall organ function [6, 7, 34, 35].

Small-molecule therapies are also being assessed for their capacity to activate contraction. Cytokinetics has developed a small-molecule that directly activates myosin and thus mimics certain properties of positive inotropes. This small molecule, however, does not result in increased intracellular calcium and does not require increased myocardial oxygen consumption [36, 37]. A primary concern with this approach, however, is that due to the achieved prolongation of systole there could be inadequate diastolic filling time. Like Cytokinetics' small-molecule, dATP increases the rate of myosin binding to actin. An advantage of dATP, however, is that dATP also increases the rate of myosin detachment from actin, which ultimately reduces the time spent in the force-generating state for myosin heads that are bound to dATP. Because dATP increases the rate of attachment more than it increases the rate of detachment, however, there is an increase in force production observed. This can be understood by exploring a two-state cross-bridge model, which is described in detail below (Section 1.3.2). Furthermore, enhanced actin-myosin interaction of a few cross-bridges can cooperatively recruit additional cross-bridge formation in the system to achieve global increases in force-producing cross-bridge interactions [38–40].

Yet another approach currently under investigation is cardiac gene therapy. The most successful gene therapy effort to date has been one aimed at improving calcium resequestration by overexpressing the

sarco-endoplasmic reticulum calcium ATPase (SERCA). This approach, using an adeno-associated virus (AAV), has achieved success through Phase IIa trials. Celladon and its founder Hajjar et al. have shown that AVV-mediated overexpression of SERCA2A is sufficient to maintain long-term (12 month) reduction in major cardiac events without adverse effects [41–43]. Although this therapy has been effective to date, it has been shown that modifications to the calcium handling apparatus can lead to unwanted off-target effects such as protease activation and/or pro-arrhythmogenic activity [44]. We propose, therefore, to use a similar method of delivery (AAV gene transfer), but to target the myofilament instead of the sarcoplasmic reticulum.

1.3.2 dATP synthesis and the effects of elevated dATP on the cross-bridge cycle and contractile function

Ribonucleotide reductase produces dATP

dATP is a naturally occurring nucleotide that is used in DNA synthesis. Its production is catalyzed by a well-conserved enzyme, ribonucleotide reductase (RR), which removes the 2' oxygen from ADP to create dADP. dADP is rapidly phosphorylated by creatine phosphokinase (CK) to create dATP (that can then be used by myosin (M) for contraction) (Figure 1.1). RR is made up two dimeric subunits, Rrm1 and Rrm2, which together catalyze the formation of deoxynucleotides. Rrm1 contains binding sites for allosteric regulation that allow it to have substrate specificity and maintain balanced nucleotide pools in the cell. Rrm2 contains the catalytic ferric iron center with a tyrosyl free radical that is required for catalysis. RR is tightly regulated via transcriptional, translational, and allosteric mechanisms [45].

Figure 1.1. Schematic of dADP synthesis via RR. R1R2 activity is tightly regulated *in vivo*, in part by allosteric inhibition from dATP. The naturally occurring enzymes that regulate ATP/ADP ratios also regulate dATP/dADP ratios.

Cross-bridge cycle

The chemo-mechanical cycle is critical to understand how cardiomyocytes use energy to develop tension and shortening. Figure 1.2 outlines a simplified model of the cross-bridge cycle that will be referenced through this document. Step (1) ATP bound to detached myosin is hydrolyzed, Step (2) myosin (in the pre-powerstroke conformation) binds to actin and undergoes the power-stroke associated with inorganic phosphate (Pi) release, tension development, and shortening (myosin is now

in the post-powerstroke conformation), Step (3) ADP is released from myosin, and Step 4) ATP binds and precipitates myosin detachment from actin.

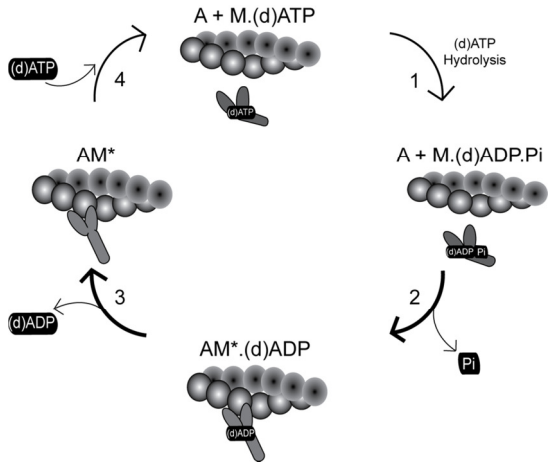

Figure 1.2. Scheme illustrating a four-step cross-bridge model of contraction. Major transitions are labeled. Dark arrows indicate transitions that we hypothesize to be enhanced when dATP is used as a substrate for contraction rather than ATP. Figure published in Ref [92].

Alterations to the dynamics of cross-bridge cycling can modify the force of contraction; increasing the probably of myosin attachment to actin (Figure 1.2, Step (2), increasing intracellular calcium, and increasing the calcium sensitivity of the thin filament proteins are examples of changes to the system that could potentially enhance contraction via increased cross-bridge binding. In addition to the number of cross-bridges bound at any given time, the rates of cross-bridge attachment and detachment are important factors of contractility [40].

In a further simplified model of the cross-bridge cycle, the two state model introduced by Brenner in 1988 [46] (Figure 1.3), the rate of myosin attachment that leads to force-generating cross-bridges is described by the apparent rate constant, f_{app}. The rate of cross-bridge attachment occurs with the apparent rate constant, g_{app}. Furthermore, the amount of force produced by the system is proportional to $f_{app}/(f_{app} + g_{app})$. This can be rewritten as $f_{app}/(1 + (g_{app}/ f_{app}))$. Therefore, the ratio of f_{app} to g_{app} describes whether an increase or a decrease in force is expected due to any perturbation in these rates. For example, in a system where f_{app} increases more than g_{app} does, an increase in force would be expected. Alternatively, if g_{app} increases more than f_{app} does, a decrease in force would be expected. When dATP is used as an energy substrate, we have observed a dramatic increase in the rate of cross-bridge attachment (f_{app}), which suggests based on this model, that at a ny given time, more cross-bridges are bound to actin, and thus we observe an increase in force (force/cross-bridge is unchanged).

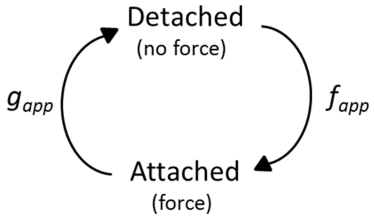

Figure 1.3. Two state cross-bridge model. First introduced by Brenner, 1988 [46], the two state model groups all force-generating states (A-M attached) into one state and all non-force generating states (mostly A-M detached) into another.

Cooperative activation of the contractile apparatus is another factor that plays a critical role in impacting contractility. The underlying principles of cooperativity are that cross-bridge binding is either facilitated by other bound cross-bridges (myosin binding prevents tropomyosin from sliding back across the thin filament, thus keeping myosin binding sites on actin exposed) or that initial cross-bridge binding recruits neighboring cross-bridges and propagates activation along the filament [40, 47, 48]. The effect of cooperativity on function can be profound; changing the kinetics of a small portion of myosin heads can dramatically enhance overall myofilament kinetics and systolic function [38, 39]. This same premise underlies the effect of dATP on the contractile properties of the heart because increasing dATP concentration to make up 2% of the nucleotide pool is sufficient to increase force and shortening by 20-40%. In *in vitro* experiments on skinned trabeculae and isolated myofibrils, we have shown that dATP-bound myosin heads increase $f_{app,}$ which results in more bound cross-bridges (discussed above). We propose that the increased rate of binding and increased number of heads bound enables force production even after calcium has dissociated from the thin filament due to the steric interference of bound myosin heads with tropomyosin. Thus, together, the increase in f_{app} and cooperative activation of the thin filament underlie the dATP-mediated increase in force production.

dATP increases the rate of cross-bridge attachment and detachment and enhances contractility in striated muscle.

Dr. Regnier has previously shown that dATP elicits faster hydrolysis and unloaded shortening velocity than ATP in skeletal muscle myosin [11–13]. In cardiac muscle, dATP binding to myosin resulted in a 40% increase in force generation at physiological levels of calcium activation (Figure 1.4) [24]. Table 1.1 summarizes many of the results from these studies, demonstrating that dATP alters the myofilament-mediated contractile properties of both cardiac and skeletal muscle [11–14, 49, 50]. Experiments assessing the biochemistry underlying the mechanical observations demonstrated that dATP binding to myosin increases both the rate of cross-bridge attachment (Figure 1.2, Step 2: M.(d)ADP.Pi (pre-powerstroke myosin) + Actin) as well as the rate of cross-bridge detachment (Figure 1.2, Step 3: ADP release from myosin is presumed to be the rate-limiting step in A-M detachment) [12] (Figure 1.2, Table 1.1).

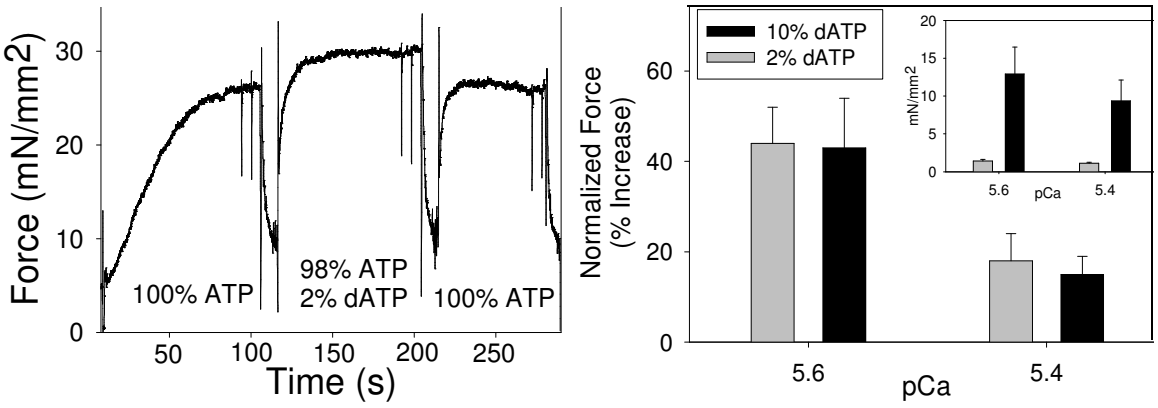

Figure 1.4. 2% dATP is sufficient to increase force in cardiac muscle. A) Example force trace at pCa 5.4 that demonstrates 2% dATP enhances force production in cardiac trabecula. (B) Quantification of force production at pCa 5.6 and 5.4 (physiological range in the heart) demonstrate the enhanced force production in the presence of 2% dATP. Inset shows absolute force (nN/mm^2) increases. Figure adapted from Ref [24].

Table 1.1. dATP increases various contractile properties in both cardiac and skeletal muscle. Summary of *in vitro* data from references [11–14, 43, 44].

Parameter Tested	Fast Skeletal Muscle	Cardiac (α-MHC)	Cardiac (β-MHC)
Maximal calcium activated force (F_{max})	+0%	+40%	+40%
Maximal rate of force redevelopment (K_{tr})	+10%	+30-60%	+30-50%
Maximal unloaded shortening velocity (V_u)	+25%	+50-75%	+70-100%
Calcium sensitivity of force (pCa_{50})	+0.15 pCa	+0.13 pCa	+0.26 pCa

While thin filament activation in the skeletal muscle system results in maximal force production, thin filament activation in the cardiac system is sub-maximal (even at high calcium concentrations) [47]. We hypothesize, therefore, that in cardiac muscle dATP binding to myosin enables increased thin filament activation by enhancing cross-bridge-mediated cooperative activation, which explains the dramatic increases force production in the cardiac system versus the skeletal muscle system (discussed in detail in Section 1.3.2, above). Additionally, it has been shown that cross-bridges in the strong-binding state can increase calcium binding to the thin filament in cardiac muscle and aid in keeping myosin binding sites on actin open [47, 51], which could further propagate the effects of elevated dATP. Combined, both of these mechanisms may be positive feedback loops that potentiate the effects of small increases in dATP concentration on force production in a highly cooperative system.

Importantly, previous work from a collaborator, Dr. Frank Brozovich, demonstrates that while dATP enhances striated muscle function, it does not have a significant impact on smooth muscle (which could deleteriously impact vascular tone and/or blood pressure). He measured contraction of WT mouse aortic muscle strips with complete replacement of ATP for dATP. Figure 1.5 demonstrates that there was no significant difference in the mechanical parameters measured for skinned aortic smooth muscle activated with 5mM ATP versus 5mM dATP; the rate of force development, and the maximal calcium activated force. LC_{20} phosphorylation did not differ between groups (data not shown). These data demonstrate that while striated muscle contraction can be significantly enhanced with increased dATP concentration, smooth muscle contraction is unchanged. These studies are discussed in further detail in Sections 2.2.5 and 2.2.6.

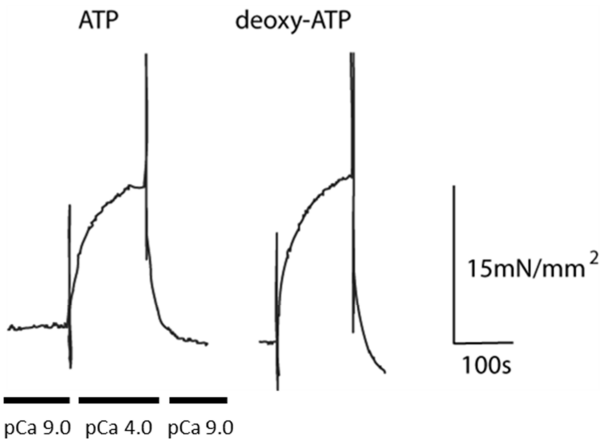

Figure 1.5. Smooth muscle contraction is not disrupted in WT mice with full exchange of dATP for ATP. An example trace from smooth muscle contraction assay is shown. Maximum force was not different between two groups: WT mouse smooth muscle strips with either 5mM ATP or 5mM dATP. Vertical lines prior to force development and immediately following plateau are noise resulting from switching calcium solutions. Figure published in Ref [92].

1.3.3 Viral-mediated overexpression of dATP

Adenoviral-mediated RR overexpression elevates dATP concentration and enhances contractility.

Recently, the Regnier lab demonstrated that adenoviral-mediated overexpression of RR (AV-RR) increases the dATP content in cultured adult and neonatal rat cardiomyocytes. This significantly enhanced the magnitude and rate of shortening and increased the rate of relaxation, without affecting the magnitude of intracellular Ca^{2+} transients (Figure 1.6 a,b) [24]. This was correlated with an overexpression of R1 and R2 and a 10-fold increase in cellular dATP content, which accounts for <1-2% of the adenosine triphosphate nucleotide pool (Figure 1.6 c,d).

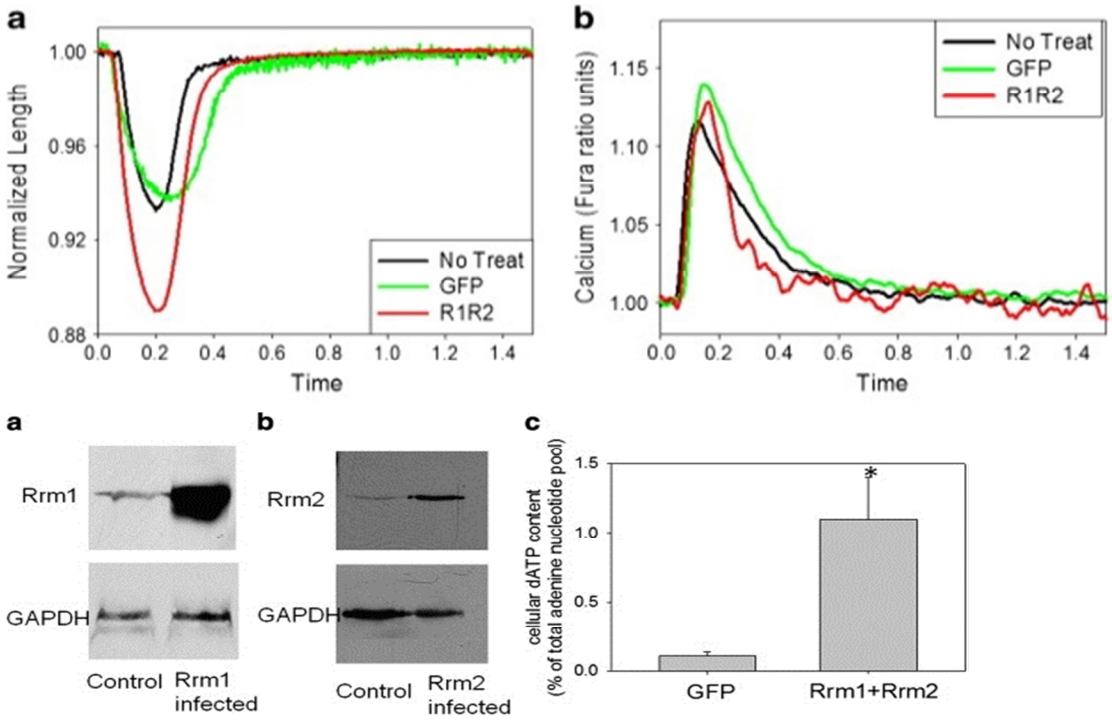

Figure 1.6. Adenoviral-mediated RR overexpression increased the rate and magnitude of shortening and relaxation without altering the calcium transient. A) Representative traces of adult rat cardiomyocyte (ARC) shortening demonstrate increased rate and magnitude of both contraction and relaxation following AV-RR transduction vs. control and AV-GFP transduced cells. (B) Viral transduction of AV-RR and AV-GFP has negligible effects on the calcium transient. (C) AV-RR transduction increases expression of R1 and R2 in ARCs, which results in a 10-fold increase in dATP (D) Figure published in Ref [24].

In a subsequent preliminary study, adult rat cardiomyocytes isolated from control rats or rats that had undergone a ligation of the left anterior descending (LAD) coronary artery were treated with AV-RR. Isolation occurred four weeks following ligation of the LAD, and transduced with AV-RR for 48hrs. As can be seen in Figure 1.8 untreated cells from infarcted rat hearts had impaired shortening, slower relaxation, and blunted calcium release. These alterations were not only reversed with treatment, but the rate and magnitude of shortening as well as the rate of relaxation were all increased in infarct + treatment cells vs. control, healthy cells. Interesting, even though AV-RR rescued the depressed calcium transient in infarcted cells, it did not increase the amount of calcium released compared to control, healthy cells. This is important to note, as we hypothesize that elevated dATP is a myofilament-targeted inotrope that does not increase intracellular calcium concentration above control levels.

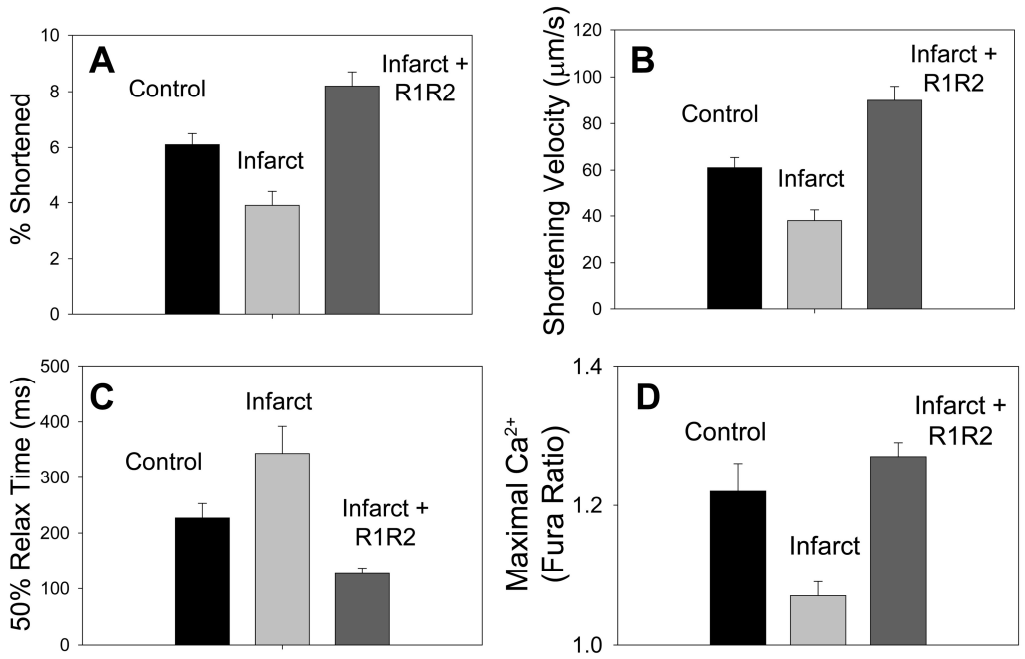

Figure 1.8. Isolated cardiomyocyte shortening measurements from control, infarcted, and infarcted + AV-RR treatment. (A) Magnitude of cell shortening (%), shortening velocity, (C) time to 50% relaxation, and (D) maximal fura 2 fluorescence, which is used as a surrogate measure of calcium release. Figure courtesy of the Regnier Lab.

In a preliminary experiment to test the effects of RR overexpression *in vivo*, healthy mice underwent either tail vein or direct cardiac injections of and adenovirus expressing RR and GFP, AV-RR-GFP, or one expressing GFP alone, AV-GFP. Four days following injection, fractional shortening in the mice that received AV-RR-GFP were increased 60-75% over those that received GFP alone (Figure 1.7). The difference in fractional shortening in these mice was attributable to increased ventricular contraction and not to ventricular dilation, as the LV inner diameter during systole was significantly reduced in the AV-RR-GFP mice. Not only did these experiments demonstrate that AV-mediated injections (both systemic and direct cardiac administration) improve baseline contractile function, but they also demonstrate that small clusters of cells with elevated dATP concentration may be sufficient to dramatically enhance cardiac function.

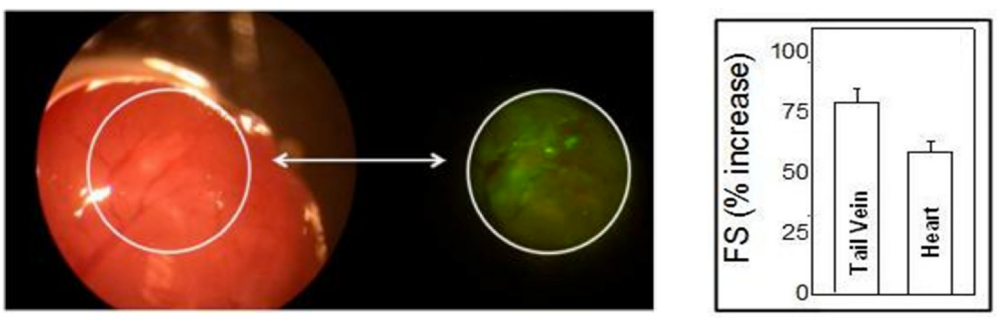

Figure 1.7. Both direct and tail vein injections of AV-RR-GFP increase fractional shortening in mouse hearts. Successful adenoviral transduction unregulated R1R2 (demonstrated by GFP+ myocardium) significantly enhanced contractile function in mouse hearts. Figure courtesy of the Regnier Lab.

Adendo-assocaited viral (AAV)-mediated overexpression of RR

Adeno-associated viral (AAV) vectors offer distinct advantages over other viral vectors in the context of cardiac gene therapy. Upon transduction, these vectors elicit sustained and long-term expression of the target gene, and generally result in few immunological complications [26, 28]. Recent work has demonstrated that AAV serotype 6 offers a unique advantage for cardiac therapies as it favors transduction into the myocardium following systemic delivery, without affecting function or inducing inflammation [27]. While they are slower to reach steady-state expression than adenoviruses (AAV's onset of expression approaches 2-3 weeks), work with AAV2 has shown that despite this lag time, AAV2 vectors expressing a therapeutic gene were able to preserve cardiac function following IR in a porcine model [28]. AAV systems are discussed in more detail in Section 3.1.

1.3.4 Known characteristics of transgenic mice overexpressing RR

A collaborator, Robert Weiss, has developed a transgenic mouse line that globally overexpresses both Rrm1 and Rrm2 (TgRR) via the chicken β-actin promoter and cytomegalovirus enhancer. Ylikallio *et al.* reported that Rrm1 and Rrm2 were overexpressed in both cardiac -- 33.7 ± 7.6 (Rrm1) and 23.7 ± 3.4 (Rrm2) fold greater than wild type (Rrm1 and Rrm2 null, WT) mice -- and in skeletal muscle -- (3.3 ± 2.1 (Rrm1) and 35.7 ± 11.1 (Rrm2) fold increases compared to WT. While cardiac dATP concentration was not directly quantified, the dATP content in the skeletal muscle of TgRR mice was increased approximately 10-fold as compared to their WT littermates [25]. The 10-fold increase in dATP concentration observed here agrees with what we have observed *in vitro* in cardiomyocytes transfected with AV-RR (Figure 1.6, above) [24]. This transgenic mouse model of global dATP overexpression provides the opportunity to study the effects of chronic dATP overexpression, potential adaptive responses, and pathology that may be associated with long-term elevation of RR expression and dATP concentration.

1.3.5 Computational studies of the structure and dynamics of myosin

Molecular Dynamics (MD) simulations offer unique insight into structure-function relationships of biomolecules [52, 53]. Atom-level resolution, dynamic simulations allow for better understanding of how conformational changes, mutations, and surface chemistry result in and physiological and functional alterations. The high-resolution computational study of myosin is still nascent. Until recently, the computational resources available have precluded long time scale simulations at atom-level

resolution of such a large protein. Furthermore, the field has been limited to few high-resolution structures that don't capture all physiologically relevant conformational states of myosin.

Myosin structure and function

Understanding the different conformations of myosin and how they integrate into the cross-bridge cycle is critical to determine the molecular mechanism of dATP. Since dATP binds directly to myosin, we hypothesize that the functional alterations observed in our mechanical analyses are attributable to structural changes in the myosin head (elicited by dATP binding) that translate into altered cross-bridge cycling.

The chemomechanical cycle (cross-bridge cycle), first illustrated by Lymn and Taylor [54], describes the different stages of the cycle in terms of the actin-myosin interaction. Through a series of weakly and strongly bound states, myosin binds and hydrolyzes ATP, binds actin, releases phosphate and initiates the powerstroke to develop tension or shortening, releases ADP, releases actin, and finally binds a new ATP (Figure 1.2). Each of these states is associated with a unique conformation of myosin, which have only been partially characterized at an atomic level. Insights into myosin's structure have come from a combination of experimental studies examining proteolytic fragments and decorated actin, as well as crystallographic and electron microscopy-based techniques.

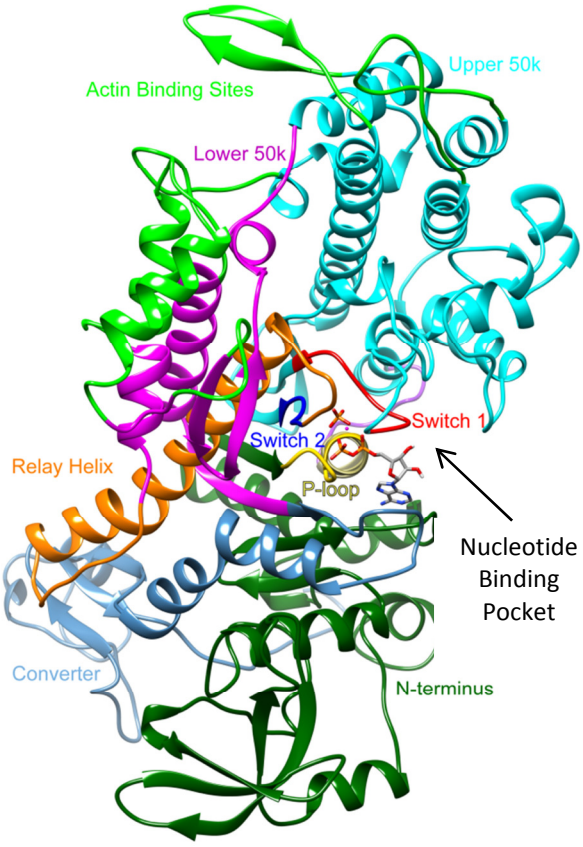

Figure 1.9. Structure of dictyostelium discoideum myosin S1 head. Functional regions highlighted in different colors: Upper 50k, cyan; Lower 50k, magenta; actin binding sites, bright green; P-loop, yellow; Switch 1, red; Switch 2, blue; Relay helix, orange; Converter, light blue; N-terminal, dark green.

The S1 head of myosin is composed of 843 residues and contains one heavy chain and two light chains and contains all of the enzymatic activity of the protein. Early studies examining the proteolytic fragments of myosin

S1 head (Figure 1.9) demonstrated that it can be broken up into three primary fragments that are named after their apparent molecular weights, N-terminal 25k domain (Figure 1.9, dark green), Middle 50K domain (divided further into Upper - and Lower-50k domains), and C-terminal 20k domain. More detailed functional studies further demonstrated that the myosin head is composed of a seven-stranded β-sheet with associated α-helices that together form a cleft that separates the Upper- and Lower- 50k regions (Figure 1.9, cyan and magenta, respectively). Both of these regions are thought to be involved in actin binding (Figure 1.9, bright green). Approximately 30 Å away from the actin binding sites near the apex of the cleft is the nucleotide binding site. This pocket is composed of a P-loop motif (Figure 1.9, yellow) as well as two switch regions (SW1 Figure 1.9, red; SW 2 Figure 1.9, blue) that resemble those observed in G-proteins. SW2 connects the lower 50k region to the relay helix (Figure 1.9, orange). The relay helix is anchored to the converter domain (Figure 1.9, light blue), which connects to the lever arm of myosin that attaches myosin to the thick filament and binds the light chains (not shown) [55, 56].

Each of these domains in myosin is involved in translating the chemical energy from nucleotide hydrolysis to the mechanical power-stroke, and each step through the cross-bridge cycle involves major conformational changes to myosin that are translated throughout the protein. Geeves and Holmes describe these changes in detail, which are beyond the scope of this introduction [55]. In the context of understanding how dATP effects cross-bridge cycling, we will focus on the immediate conformational alterations dATP binding makes to the nucleotide binding site in addition to how those changes in the binding site effect the actin binding surface of myosin.

CHAPTER 2. TRANSGENIC OVEREXPRESSION OF RIBONUCLEOTIDE REDUCTASE IMPROVES CARDIAC PERFORMANCE

Nowakowski SG, Kolwicz SC, Korte FS, Luo Z, Robinson-Hamm JN, Page JL, Brozovich F, Weiss RS, Tian R, Murry CE, Regnier M. (2013) Transgenic overexpression of ribonucleotide reductase improves cardiac performance. Proc Natl Acad Sci U S A 110:6187–92.

2.1 Introduction

A wide variety of cardiac pathologies such as myocardial infarct, dilated cardiomyopathy, and congestive heart failure involve reduced systolic function of ventricles that often results from altered ATP-mediated actin-myosin (cross-bridge) cycling [40, 57–59]. The schematic shown in Figure 1.2 outlines the basic components of this chemo-mechanical cycle that are critical to understand how cardiomyocytes use energy to develop tension and shortening; 1) ATP bound to detached myosin is hydrolyzed to ADP and inorganic phosphate (Pi), 2) myosin binds to actin and undergoes the power-stroke associated with Pi release, tension development and shortening, 3) ADP is released from myosin, and 4) ATP binds and enables myosin detachment from actin.

We [11–14] and others [15–23] have reported that striated muscle myosin can use most naturally occurring nucleotides to support cross-bridge cycling and contraction to varying degrees. While most are not as effective as ATP, we found that 2 deoxy-ATP (dATP) is more effective than ATP as a substrate for contraction of demembranated cardiac muscle, augmenting both force and shortening at all levels of Ca^{2+} mediated contractile activation [11–14]. Our detailed biochemical and mechanical analysis suggests that dATP increases the rates of both myosin binding and product release (steps 2 and 3 in Figure 1.2) [12]. More recently we reported that adenoviral overexpression of Ribonucleotide Reductase (RR), the enzyme that converts ADP to dADP (which is rapidly phosphorylated to become dATP), increases the dATP content in cultured adult or neonatal rat cardiomyocytes ~10-fold. This significantly enhanced the magnitude and rate of shortening and increased the rate of relaxation, without affecting the magnitude of intracellular Ca^{2+} transients [24]. Interestingly, the 10-fold increase in cellular dATP content still represents <1-2% of the adenosine triphosphate nucleotide pool, and we also showed that this amount was sufficient to significantly increase force production of demembranated cardiac muscle at levels of Ca^{2+} measured during cardiac twitch contractions [24].

Although we demonstrated that acute increases in [dATP] (via RR overexpression) positively impacted contractility of cardiomyocytes *in vitro*, it was not clear if this elevated function would occur *in vivo*.

Additionally, it is not known whether chronically elevated dATP would have negative effects on myocardial energetics and/or cardiac function. Here we report the first description of an animal model with enhanced cardiomyocyte cross-bridge chemo-mechanical cycling via manipulation of the adenosine triphosphate nucleotide pool of healthy animals. We studied a transgenic mouse line that globally overexpresses both the large (Rrm1) and small (Rrm2) subunits of RR (TgRR), as compared to their wild-type (WT) littermates (named $Rrm1^{Tg}$+$Rrm2^{Tg}$ in reference [25]). In this study, TgRR and WT animals were characterized for *in vivo* and *in vitro* cardiac function, myocardial energetics, and cardiomyocyte contractile properties to assess the effect of chronic, global overexpression of Rrm1 and Rrm2 (and thus increased dATP) on cardiac function. We found that left ventricular (LV) function is elevated in TgRR mice vs. WT under basal conditions, but is similar during β-adrenergic challenge. The enhanced cardiac function was associated with an increased magnitude and rate of contraction and relaxation of isolated cardiomyocytes, without an increase in Ca^{2+} transient amplitudes. Furthermore, the improved cardiac function occurred at a normal energetic cost and with no effect on smooth muscle contraction. These data suggest that manipulation of the adenosine triphosphate nucleotide pool to increase cardiomyocyte intracellular dATP concentration merits further investigation as a potential therapeutic option for treatment of systolic heart failure.

2.2 Materials and Methods

2.2.1 Animal Model

Transgenic mice that over-express *both* the Rrm1 and Rrm2 subunits of ribonucleotide reductase via the chicken β-actin promoter and cytomegalovirus enhancer (referred to as TgRR mice hereafter) have been previously described [60]. WT mice used in this study were transgenic animals bred on the same background (FVB/N) as TgRR mice. All animal experiments were approved by the University of Washington (UW) Animal Care Committee and were carried out in accordance with federal guidelines. Animals were housed in the Department of Comparative Medicine at the UW and were taken care of in accordance with the US NIH Policy on Humane Care and Use of Laboratory Animals.

2.2.2 Histology

Adult mice were euthanized by carbon dioxide asphyxiation. Tissues for histological analysis were excised, fixed overnight at room temperature in 10% buffered formalin, processed, and sectioned at 5μm thickness prior to staining with hematoxylin and eosin (H&E) or Masson's trichrome. Sample

dehydration, embedding, sectioning, and staining were conducted by the Histology Core Facility in the College of Veterinary Medicine at Cornell University.

2.2.3 Echocardiography

Echocardiography was carried out on mice 3-5 months old. The animals were lightly anesthetized using 1% isofluorane. Images were collected with a GE Vivid 7 system using 13MHz linear transducer (General Electric Healthcare). Left ventricular end-diastolic (LVEDD) and left-ventricular end-systolic (LVESD) dimensions were determined using M-mode measurements obtained by short-axis views at the mid-papillary level. All data were averaged from at least three cardiac cycles. Fractional shortening was calculated from these data using the formula: (LVEDD-LVESD)/LVEDD x 100. All echocardiography was carried out by a single reader who was blinded to the genotype of the animals.

2.2.4 RNA Isolation and Real Time PCR

Total RNA was isolated from frozen heart tissue using the RNeasy Mini Kit (Qiagen) and cDNA was synthesized using the Omniscript RT kit (Qiagen) according to manufacturer's guidelines. Real time PCR was performed using iQ SYBER Green Supermix (Bio-Rad) with the following primer sequences:
myh6: F: GGCAAAGTCACTGCGGAAACTGAA, R: TCTTGTCGAACTTGGGTGGGTTCT; myh7: F: GCAGCTGTGCATCAACTTCACCAA, R: TCCACTCAATGCCCTCCTTCTTGT; anp: F: ATTGACAGGATTGGAGCCCAGAGT, R: TGACACACCACAAGGGCTTAGGAT; bnp: F: GCCAGTCTCCAGAGCAATTCA, R: GGGCCATTTCCTCCGACTT.

2.2.5 Smooth Muscle Contractile Studies

All solutions and the methods for tissue preparation have been described in detail [61–64]. Briefly, the mouse aorta was removed and placed into Ca^{2+} free PSS solution (140mM NaCl, 4.7mM KCl, 1.2mM $NaH_2PO_4x7H_2O$, 2.0mM MOPS, 0.02mM EDTA, 1.2mM $MgCl_2x6H_2O$, 5.6mM glucose, and 0.5mM EGTA, pH=7.0), cleared of connective tissue, then cut into strips approximately 400-500μm long, 200μm wide, and 50μm thick and mounted between aluminum foil T-clips. Strips were then transferred to a mechanics workstation (Model 600, Aurora Scientific, Aurora, Canada) and mounted between a force transducer (Akers AE 801, MEMSCAP, San Jose, USA) and servomotor (Aurora Scientific, Aurora, Canada). The tissue was stretched to a level sufficient to just develop tension and then an additional 30%, defining the length for maximum force (Lo). Following stretching, tissue strips were skinned by transferring the preparation into a 1% Triton solution for 15-20min. Strips were then returned to pCa9

and maximally activated with Ca^{2+} (pCa 4). The effects of dATP were investigated in solutions containing either 5mM ATP or 5mM dATP.

Calcium solutions were prepared using a computer program designed to give a set of free ion concentrations that are adjusted for both temperature and ionic strength. The ionic strength for all solutions was 200mM and the experiments were carried out at a temperature of 22^{o}C. Solutions used were: relaxing (pCa9.0) containing (in mM): 25 BES, 10 EGTA, 0.02 $CaCl_2$, 7.2 $MgCl_2$, 5.5 ATP or dexoy ATP, 25 creatine phosphate, 56.5 KMS, pH to 7.0 with 1M KOH; and activating (5 mM ATP or 5 mM deoxyATP, pCa4): 25 BES, 10 EGTA, 10.22 $CaCl_2$, 6.97 $MgCl_2$, 5.6 ATP/deoxyATP, 25 creatine phosphate, 34.6 KMS, pH to 7.0 with 1M KOH. Creatine kinase was added prior to each experiment and all solutions contained 250u/ml calmodulin.

2.2.6 LC_{20} Phosphorylation

LC_{20} phosphorylation was determined as previously described [61–64]. Briefly, tissue strips were skinned and then placed in pCa9 solution (5 mM MgATP or deoxy-MgATP) for 20 min. Strips were either kept in pCa9 or transferred into pCa4 solution (5 mM MgATP or deoxy-MgATP) for an additional 15 min. The tissue was then denatured in 15% (v/v) trichloroacetic acid in acetone for 30 min in liquid nitrogen. Following denaturation, strips were washed four times with acetone and air dried. LC_{20} was solubilized in PAGE sample buffer containing 6M urea, 20mM glycine, 22mM Tris-HCL, pH 8.6, and 1mM EDTA. Glycerol (5% v/v) and bromophenol blue (0.1% w/v) were added to the samples prior to loading. The samples were resolved by a 19:1 (acrylamide : bisacrylamide) 10% polyacrylamide gel containing 40% (v/v) glycerol, 4M urea and polymerized in a gel buffer containing 20mM glycine and 22mM Tris-HCl, pH 8.6. Resolved proteins were transferred to nitrocellulose membrane and the phophorylated and unphosphorylated LC_{20} were identified by immunoblotting using a LC_{20} mAb (Sigma). The percentage of LC_{20} phosphorylated was defined as the ratio between the LC_{20} band versus the total LC_{20} (phosphorylated + unphosphorylated forms) identified by the mAb.

2.2.7 Isolated Perfused Mouse Heart Preparation and ^{31}P NMR Spectroscopy

Myocardial energetics and LV function were measured in Langendorff isolated heart preparations combined with ^{31}P nuclear magnetic resonance (NMR) spectroscopy as previously described [65–67]. In brief, excised mouse hearts were perfused at a constant pressure of 80mmHg with a modified Krebs Henseleit (KH) buffer consisting of (mmol/L): 118 NaCl, 25 $NaHCO_3$, 5.3 KCl, 2.0 $CaCl_2$, 1.2 MgSO4, 0.5

EDTA, 5.5 glucose, and 0.5 pyruvate, equilibrated with 95% O_2 and 5% CO_2 (pH 7.4). Temperature was maintained at 37.5°C throughout the protocol. After 20 minutes of equilibration, baseline function was monitored for 10 minutes at a fixed end diastolic pressure (EDP) of 8-10mmHg by way of a water-filled balloon inserted into the left ventricle (LV). After baseline, dobutamine (DOB) was infused at 5% of the coronary flow at a final concentration of 300nM for 20 minutes. Dynamic changes in high energy phosphate content (phosphocreatine, PCr; ATP, and inorganic phosphate, Pi) were monitored using ^{31}P NMR spectroscopy simultaneously with continuous recording of LV function via a data acquisition system (PowerLab, ADInstruments, Colorado Springs, CO) during the entire perfusion protocol.

^{31}P NMR spectra were acquired on a 14T magnet interfaced with an Avance III console and TopSpin V2.1 software (Bruker Biospin, Billerica, MA). Spectra were obtained by averaging 120 free induction decays (FID) over a time period of 5 minutes at a pulse angle of 60°, acquisition time of 0.4 sec, and recycle time of 2.14 sec. Frequency-domain NMR spectra were obtained by Fourier transformation of the FIDs and analyzed using 20 Hz exponential multiplication and zero and first order phase corrections. The average of γ- and β-ATP peak areas obtained at baseline was set to 100% and used as the reference value for all peaks in the ^{31}P NMR spectra. Intracellular pH was determined by comparison of the chemical shift of inorganic phosphorous and PCr.

2.2.8 Adult mouse cell isolation and contractile assessment

Adult mouse cardiomyocytes (CMs) were isolated by enzymatic digestion from 3-5 month old mice as previously described [68] in accordance with AfCS protocol. Briefly, the hearts were rapidly excised and cannulated through the aorta and perfused with a calcium-free buffer to arrest the heart. Myocytes were dissociated via a collagenase-based solution. The ventricles were then removed, minced, and placed in fresh digestion buffer. The digestion reaction was stopped and cells were reintroduced to calcium by multiple re-suspensions in solutions with increasing calcium concentrations. Finally, cells were re-suspended in 37°C standard media (DMEM) supplemented with penicillin G (100U/ml) and streptomycin (100 µg/ml).

Contractile assessment of cells was carried out on the same day as isolation. Cells were treated with Fura-2 AM (1 µl/ml of media) and ultimately resuspended in Tyrodes buffer (in mmol/L: CaCl2 1.8, MgCl2 1.0, KCl 5.4, NaCl 140, HEPES 10, NaH2PO4 0.33, glucose 5; pH 7.4) and plated on 25 mm^2 glass coverslips (1.0 thickness). Cell shortening and re-lengthening was recorded and measured using IonOptix

SarcLen system video microscopy (IonOptix, Milton, MA, USA). A 40x objective lens (Olympus uWD 40) and 25x intermediate lenses were used for video microscopy, and all measurements were performed on a heated stage set to 37°C. Cells were not measured if they did not respond to field stimulation 1:1 and/or if their resting sarcomere lengths were below 1.70 μm. Field stimulation was performed with a 4ms square supra-threshold (10V) pulse at 1, 3, and 5Hz through parallel platinum electrodes. Cell shortening was recorded by illuminating the myocytes with red transmitted light (> 600 nm). Calcium transients were measured in Fura-2 loaded myocytes using IonOptix equipment as previous described [24]. Briefly, calcium transients were recorded by measuring Fura-2 fluorescence (IonOptix spectrophotometer with stepper switch) passed through a 510 nm emission filter to a photomultiplier tube using the interpolated pseudo-ratiometric method with a 380 nm excitation during, and a 360 nm excitation at the beginning and the end of, 20 second recording events. The cell and sarcomere length measurements were recorded simultaneously with Fura-2 fluorescence by computer acquisition and were subsequently analyzed using the proprietary IonOptix software. Experiments were performed by 4 different experimentalists, and were analyzed in duplicate by 2 different analysts. No differences were observed between mice, experimentalists, or analysts

2.2.9 Statistical Analysis

Statistical differences for echocardiography, sarcomere length, and calcium transients were performed using students' t-test (SPSS v.18). Summary *ex vivo* function data (Figure 2.3 and Figure 2.4) were assessed using a 2-way ANOVA with a Bonferroni *post-hoc* analysis. Figure 2.3 and Figure 2.5 data was analyzed using 2-way ANOVA with repeated measures with a Bonferroni *post-hoc* analysis (Graph Pad/Prism Version 5.01). p-values < 0.05 were considered significant. Data is displayed as mean ± SEM.

2.3 Results

2.3.1 Heart Size and Histology

At 3-5 months of age, body weight (BW), heart weight (HW), and HW relative to BW (HW/BW) were obtained for TgRR mice and littermate controls (WT). No significant differences were noted in these measures (Table 2.1). The similar HW and HW/BW values suggest there is no overt hypertrophy (at least to 3-5 months of age) resulting from the chronic inotropic state induced by elevated dATP. Histological assessment of TgRR and WT hearts showed no appreciable difference in myocyte size, organization, or fibrosis between groups at both 3 months and 12 months of age, which further demonstrates that TgRR hearts are not morphologically different than controls (Figure 2.1).

Table 2.1. Descriptive statistics of animal phenotype. Body weight (BW), heart weight (HW), and HW/BW ratio from WT and TgRR animals between 3-5 months of age. Data are presented as mean ± SEM (WT n=6, TgRR n=6).

	WT	TgRR
BW (g)	27.91 ± 0.87	26.02 ± 1.11
HW (mg)	115.32 ± 8.52	106.00 ± 3.64
HW/BW (mg/g)	4.19 ± 0.19	4.36 ± 0.15

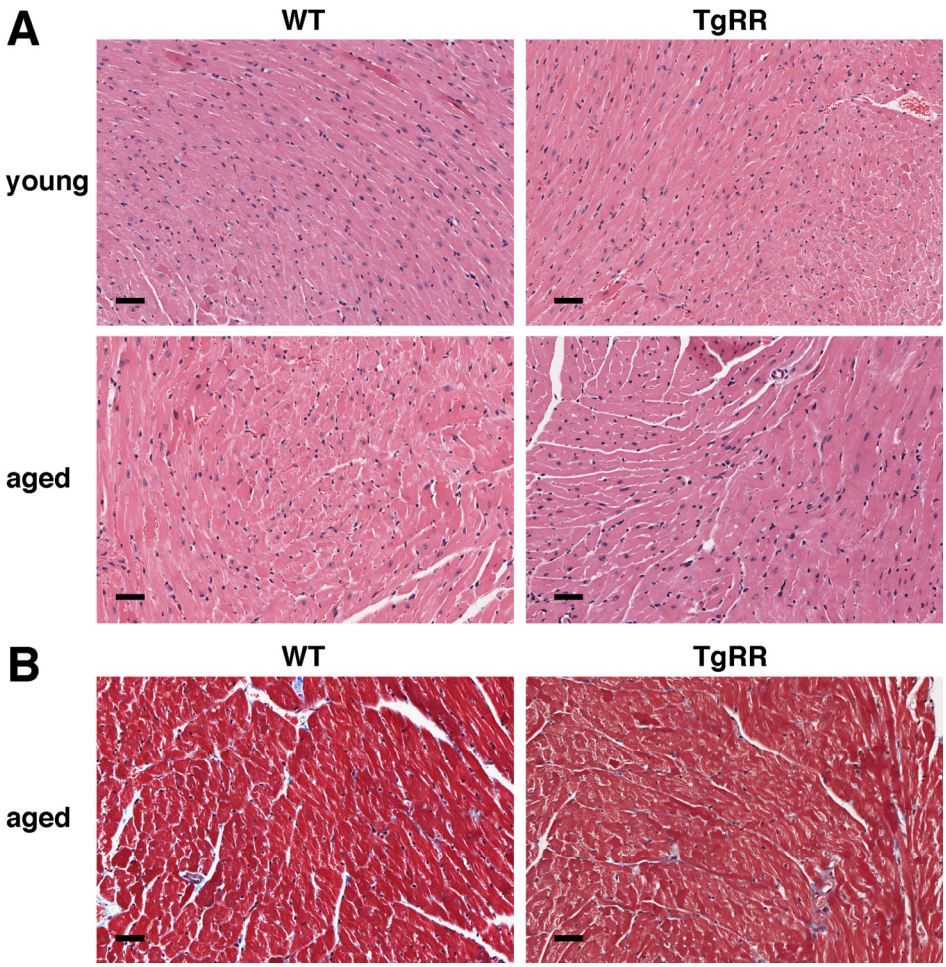

Figure 2.1. Histological assessment of WT and TgRR hearts. Cardiac muscle morphology in TgRR and WT control mice. Tissues from young (3-month-old) or aged (12-month-old) mice were stained with (A) H&E or (B) with Masson's trichrome. Scale bar equals 25 µm.

2.3.2 Echocardiography

In vivo cardiac function was assessed via echocardiography for both WT and TgRR mice (Table 2.2). TgRR mice had significantly increased fractional shortening (from 34.6 ± 2.2% to 43.5 ± 1.4%, $p<0.05$), ejection fraction (70.1 ± 2.8% to 80.7 ± 1.4%, $p<0.05$)), and cardiac output (from 30.0 ± 3.2 ml/min to 41.0 ± 2.8 ml/min, $p<0.05$) at similar heart rates. Neither LV internal dimension (LVID;d) nor LV posterior wall thickness (LVPW;d) was altered in the transgenic animals (Table 2.2). These data suggest that increased cellular concentration of RR and dATP can result in a beat-to-beat elevation of cardiac performance in vivo. Combined with the similar HW/BW ratio for TgRR and WT mice, these data support the idea that enhanced ventricular function did not result in cardiac hypertrophy. Importantly, there were no significant differences in diastolic dimensions, suggests no evidence of LV dilation. This indicates that increased cardiac output is achieved by increased contractile force and not attributable to changes in LV filling volume. These findings, combined with the HW/BW and histological observations described above, demonstrate that there is little or no compensatory adverse cardiac remodeling in TgRR mice.

Table 2.2. Echocardiography measurements. Echocardiographic measures obtained in WT and TgRR animals. LVPW;d: LV posterior wall thickness in diastole, LVID;d: LV internal dimension in diastole, LVPW;s: LV posterior wall thickness in systole, LVID;s: LV internal dimension in systole, FS: fractional shortening, EF: ejection fraction, HR: heart rate, CO: cardiac output. Data are presented as mean ± SEM (WT n=5, TgRR n=10). *$p < 0.05$.

	WT	TgRR
LVPW;d (mm)	0.70 ± 0.12	0.81 ± 0.04
LVID;d (mm)	3.22 ± 0.11	3.30 ± 0.14
LVPW;s (mm)	1.04 ± 0.07	1.21 ± 0.04 *
LVID;s (mm)	2.10 ± 0.09	1.72 ± 0.10 *
FS (%)	34.58 ± 2.17	43.54 ± 1.43 *
EF (%)	70.65 ± 2.75	80.68 ± 1.45 *
HR (bpm)	454.20 ± 28.57	497.10 ± 21.67
CO (ml/min)	30.00 ± 3.16	41.00 ± 2.77 *

2.3.3 Ex Vivo + ^{31}P NMR Spectroscopy

To quantitatively assess the effects of increased Rrm 1 and Rrm2 (RR) and dATP on myocardial energetics and cardiac work, we measured high energy phosphate content with ^{31}P NMR spectroscopy in Langendorff isolated heart preparations. Consistent with *in vivo* echocardiography data, TgRR hearts demonstrated a ~30% increase in LV developed pressure (LVDevP; $p < 0.05$, Figure 2.2 A, S2A) at a similar heart rate at baseline (HR; Figure 2.2 B, Figure 2.3 B). Overall myocardial performance (or work) was assessed by the rate-pressure product (RPP), the product of LVDevP and HR. This was also significantly elevated in TgRR compared to WT under normal workload conditions (Figure 2.2 C, Figure 2.3 C) with equivalent coronary flows (Figure 2.2 D, Figure 2.3 D). A marker of the rate of contractility, +dP/dt, was approximately 35% higher in TgRR mice ($p < 0.05$ vs. WT at BL; Figure 2.2 E, Figure 2.3 E) while –dP/dt, a marker of ventricular relaxation rate, appeared faster but was not significantly different (Figure 2.2 F, Figure 2.3 F).

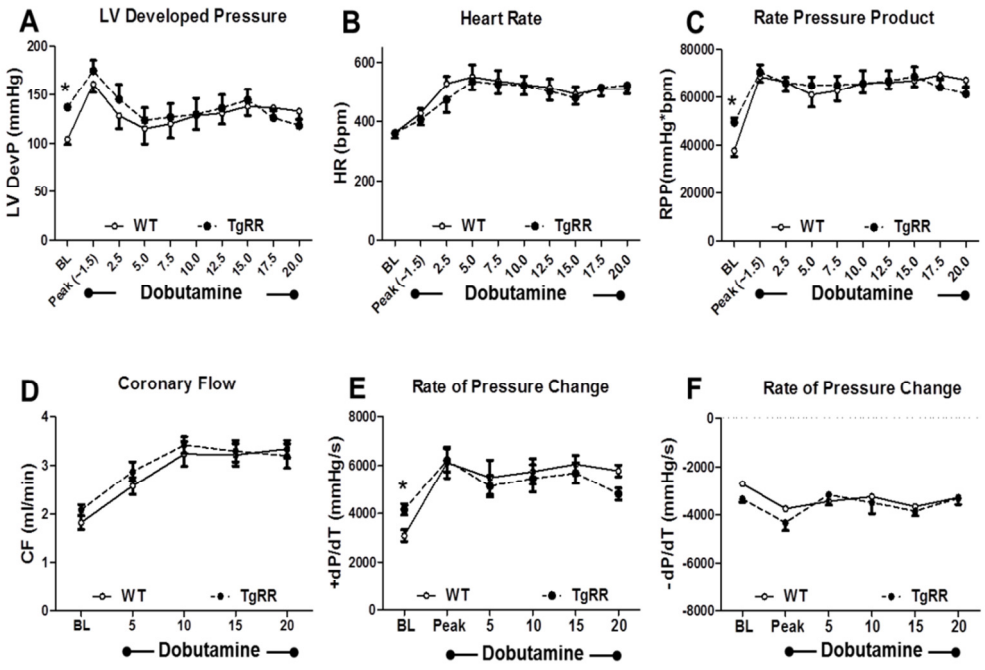

Figure 2.2. Response of LV function during 20 minutes of acute physiological demand. (A-C) Left ventricular developed pressure (LVDevP), heart rate (HR), and rate-pressure product (RPP), the product of LVDevP and HR, measured in isolated hearts perfused at baseline (BL) and dobutamine infusion. n=5 each group. (D) Coronary flow, estimated by collecting the perfusate effluent over a 2-minute period, in Langendorff heart preparations during normal workload and dobutamine infusion.. n= 5 each group. (E,F) Rate of pressure change calculated by the first derivative of the LV pressure wave (dP/dt) in Langendorff heart preparations at baseline and during dobutamine infusion. The positive maximum (+dP/dt) is an index of the rate of LV pressure development. The negative maximum (-dP/dt) is an index of the rate of ventricular relaxation. *p< 0.05 vs. WT at BL, n=5 each group.

This enhanced cardiac performance at baseline resulted in a ~10% decrease in levels of the energy reserve compound, PCr, in TgRR mice ($p < 0.05$ vs. WT, Figure 2.4, Figure 2.5). Even though this is a statistically significant reduction, the energetic reserves are still quite considerable (pathologic conditions are associated with 40-50% decreases in PCr [69–71]). There was no significant difference in ATP content (Figure 2.5 B), but Pi was significantly greater in TgRR hearts ($p < 0.05$ vs. WT; Figure 2.5 C) with no difference in intracellular pH (Figure 2.5 D). Even though elevation of Pi has not been demonstrated to significantly reduce function in the heart as it does in skeletal muscle, the higher [Pi] (2.98 ± 0.37mM vs. 4.29 ± 0.37mM, respectively) could reduce LVDevP via Pi-mediated inhibition of force production [72–74]. If so, the potential for increased LV function by elevated cardiomyocyte dATP levels may be even greater than in Figure 2.2 under *in vivo* conditions where cardiac tissue Pi buffering occurs. Combined, these results suggest that increased cardiac contractility in TgRR hearts causes a mild reduction in high energy phosphate reserves, without compromising cellular ATP concentration under normal workload (basal) conditions.

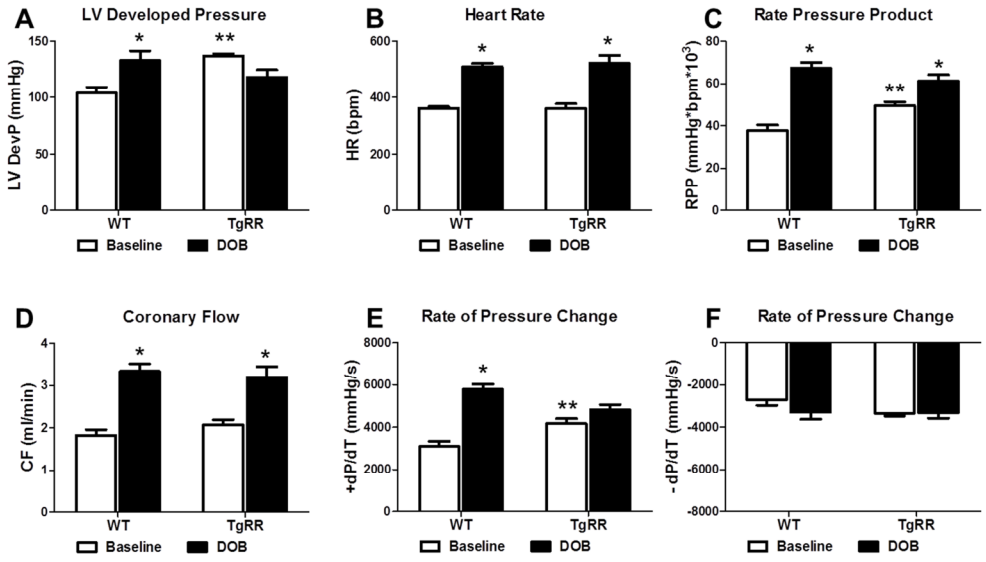

Figure 2.3. Response of LV function during acute physiological demand. (A-C). Left ventricular developed pressure (LVDevP), heart rate (HR), and rate-pressure product (RPP), the product of LVDevP and HR, measured in isolated hearts perfused at baseline (BL) and at the end of dobutamine infusion (DOB). (D). Coronary flow, estimated by collecting the perfusate effluent over a 2 minute period, in Langendorff heart preparations during normal workload and at the end of dobutamine infusion (DOB). (E,F). Rate of pressure change calculated by the first derivative of the LV pressure wave (dP/dt) in Langendorff heart preparations at baseline and at the end of dobutamine infusion (DOB). The positive maximum (+dP/dt) is an index of the rate of LV pressure development. The negative maximum (-dP/dt) is an index of the rate of ventricular relaxation. * $P < 0.05$ vs. respective WT BL. ** $P < 0.05$ vs. WT, n=5 each group.

To test whether overexpression of the RR transgene alters myocardial responsiveness to β-adrenergic stimulation, we infused dobutamine in isolated perfused hearts from TgRR and WT mice. During the initial 90 seconds of dobutamine infusion, LVDevP, +dP/dT, and –dP/dT were significantly increased in both WT and TgRR hearts, demonstrating expected peak β-adrenergic responsiveness (Figure 2.2 A, E, F). However, as the HR approached 500bpm after 5 minutes of dobutamine infusion (Figure 2.2 B), LVDevP, +dP/dT, and –dP/dT declined in both groups (Figure 2.2 A, E, F), consistent with the negative treppe effect (i.e., force-frequency relationship) in mouse myocytes [75]. Over the final 15 minutes of the experimental period HR remained significantly elevated to a comparable degree in both TgRR and WT mice, demonstrating normal adrenergic reserve (Figure 2.2 B, Figure 2.3 B). Interestingly, even though LVDevP at the end of dobutamine infusion in WT hearts was similar to baseline values in TgRR (Figure 2.3 A), dobutamine infusion did statistically increase RPP over the entire infusion time course and remained statistically elevated over baseline levels in both groups at the end of the protocol (Figure 2.2 C, Figure 2.3 C). Thus, the TgRR hearts generate higher baseline force and respond to adrenergic challenge principally with increased rate. The normal rate response suggests that much of β-adrenergic signaling is intact, neither blunted nor sensitized in the TgRR heart. Both TgRR and control hearts experienced similar decreases in PCr (~40%), and ATP (~20%) in response to acute demand (Figure 2.4, Figure 2.5) with associated increases in Pi (Figure 2.5 C). Intracellular pH remained stable in hearts for both groups (Figure 2.5 D). In total, these data indicate that TgRR hearts responded to the acute physiological challenge with a similar work output to controls with comparable changes of high energy phosphate content.

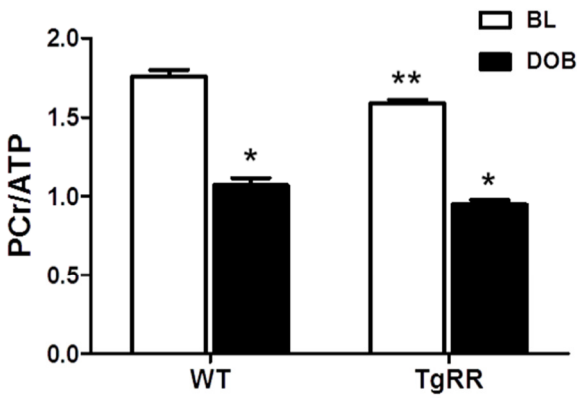

Figure 2.4. Energetic response to dobutamine challenge. Ratio of phosphocreatine (PCr) and ATP as measured by ^{31}P NMR spectroscopy in isolated perfused hearts at baseline (BL) and at the end of 300nM dobutamine infusion (DOB). * P<0.05 vs. WT at baseline, n=5 each group.

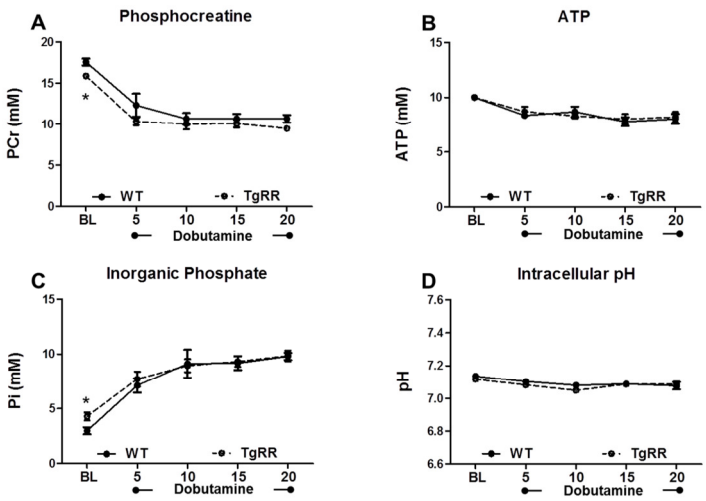

Figure 2.5. Changes of high energy phosphate content during dobutamine challenge. (A-C) Phosphocreatine (PCr), ATP, and inorganic phosphate (Pi) content measured by ^{31}P NMR spectroscopy in isolated perfused hearts at baseline (BL) and during 300nM dobutamine infusion. *p<0.05 vs WT at baseline, n=5 each group. (D) Intracellular pH determined by the relative chemical shift between Pi and PCr at BL and during dobutamine infusion. n=5 each group.

2.3.4 Smooth muscle function

While we [11–14] and others [15–23] have characterized the effect of dATP on striated (skeletal and cardiac) muscle, its effect on smooth muscle is unknown. To determine if vascular smooth muscle responds differently than striated muscle, we measured contraction of non-transgenic mouse aortic muscle strips with complete replacement of ATP for dATP. Figure 1.5 demonstrates that there was no significant difference in the mechanical and biochemical parameters measured for skinned aortic smooth muscle activated with 5mM ATP versus 5mM dATP. When smooth muscle was activated, force rapidly increased to a steady state with both nucleotides. Maximal Ca^{2+} activated force was 25.7 ± 4.8mN/mm^2 (n=8) vs. 25.4 ± 5.5mN/mm^2 (n=7) for ATP vs. dATP, respectively. Since LC_{20} phosphorylation regulates smooth muscle cross-bridge cycling, we quantified the level of phosphorylation in smooth muscle preparations with solutions containing ATP vs. dATP. For ATP, LC_{20} phosphorylation was 2 ± 0.5% at rest (pCa 9) and increased to 33 ± 2% at pCa 4 (n=3), while for dATP, LC_{20} phosphorylation increased from 3 ± 1% to 34 ± 5% (n=3). Since LC_{20} phosphorylation did not differ between preparations with ATP vs. dATP, these data suggest that dATP does not alter the regulation of smooth muscle. Importantly, this indicates that even though increased [dATP] significantly enhances striated muscle contraction, smooth muscle contraction is unchanged by dATP.

2.3.5 Intact cardiomyocyte contractility

Video imaging of sarcomere length (IonOptix) was used to compare the rate and extent of shortening and re-lengthening (relaxation) in single ventricular cells from both TgRR and WT mice. Simultaneous measurements of Ca^{2+} transients were made using Fura2 fluorescence. Representative shortening traces

and Ca^{2+} transients can be seen in Figure 2.6 A and B, respectively. Cardiomyocytes from the TgRR mice had enhanced contractility relative to control (WT) cells, measured by a number of parameters (Table 2.3). The rate and magnitude of shortening were increased by 15.4% and 21.5%, respectively, and rate of relaxation was increased 28.4% (Figure 2.6 A and Table 2.3). These increases in contraction and relaxation properties are similar, but smaller in magnitude, to those we recently reported for adult and neonatal rat cardiomyocytes transduced with an adenoviral vector to elevate cellular RR levels and dATP content (AV-RR) [24]. These cardiomyocyte contractility data support our *in vivo* observations of increased FS and EF, as well as our *in vitro* observations of increased LV rate and magnitude of pressure development. Interestingly, the increased cardiomyocyte contractility occurred with no change in Ca^{2+} transient amplitude (Figure 2.6 B and Table 2.3), thus myofilament responsiveness to Ca^{2+} is increased in TgRR animals (Table 2.3). This also agrees with our previous report of AV-RR transduced adult rat cardiomyocytes [24] and, together, suggests that increasing [dATP] acts primarily to increase myofilament cross-bridge cycling at similar levels of Ca^{2+}.

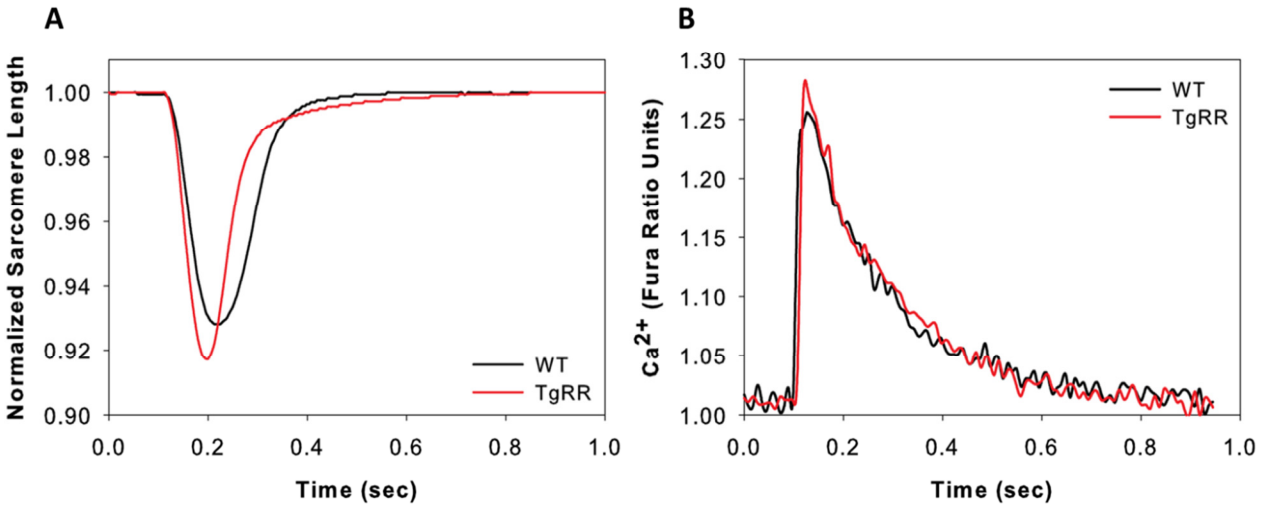

Figure 2.6. Representative sarcomere length (A) and calcium (B) traces from TgRR and WT single isolated ventricular myocytes. (A) Representative sarcomere length traces obtained using video microscopy (IonOptix). WT shortening is shown in grey and TgRR is shown in black. (B) Representative Fura2 fluorescence traces obtained during shortening. No observable difference in calcium handling was noted. WT is shown in grey and TgRR in black. Quantification of these traces (and others) can be found in Table 2.3.

Table 2.3. Sarcomere length and calcium transient values at 1hz stimulation. Measures of sarcomere length and calcium transients obtained in isolated cardiomyocytes from WT and TgRR at 3-5 months of age. Cardiomyocytes were stimulated at 1Hz. Data are presented as mean ± SEM (WT n=73 cells, TgRR n=75 cells). *$p < 0.05$.

	WT	TgRR
Fractional Shortening (%)	7.26 ± 0.36	8.40 ± 0.23 *
Rate of Shortening	-2.93 ± 0.18	-3.56 ± 0.12 *
Time to Peak (ms)	99.95 ± 3.23	92.92 ± 2.61
Rate of Relaxation (μm/sec)	1.76 ± 0.15	2.26 ± 0.11 *
Magnitude of Ca^{2+} Release (%)	38.14 ± 1.89	39.08 ± 1.69
Rate of Ca^{2+} Release (Fura Units/sec)	24.90 ± 1.18	25.71 ± 1.08
Rate of Ca^{2+} Reuptake (Fura Units/sec)	-1.98 ± 0.09	-1.95 ± 0.10

2.4 Discussion

The purpose of this study was to characterize the cardiac function of transgenic animals that overexpress RR, resulting in increased cardiomyocyte [dATP]. The data presented here demonstrate that increased rate and magnitude of cardiomyoycte contraction and increased cardiac performance resulting from elevated cardiomycoyte [dATP] persist into adulthood. We further show that this occurs with minimal effects on cardiac energetic reserves. Additionally, β-adrenergic rate-responsiveness to increase cardiac output is maintained for TgRR mice, though the absolute magnitude of increased cardiac output is somewhat reduced due to significantly increased basal pressure development. Importantly, with β-adrenergic stimulation maximal performance is maintained and myocardial energetics are comparable to WT hearts. Also important is that enhancement in contractile function does not result from, or result in, hypertrophy or altered diastolic dimensions, at least out to 3-5 months of age in mice. To further assess changes in the expression of genes related to myosin isoforms and cardiac hypertrophy, we measured expression levels of myh6 (α-myosin), myh7 (β-myosin), anp (atrial naturetic peptide), and bnp (brain naturetic peptide) via RT-PCR (Figure 2.7). Both myh6 and myh7 were significantly down regulated to a similar degree in TgRR vs. WT (Figure 2.7 A,B). Since upregulation of the fetal isoform myh7 is associated with cardiac pathologies in mice, these data suggest that chronic elevation of dATP did not cause pathological-associated changes in the myosin isoforms. Consistent with this, upregulation of ANP or BNP was not observed in TgRR hearts. This elevation of baseline

cardiac function may persist through life, as we have observed elevation of LV function with no signs of hypertrophy in 8-10 month TgRR mice.

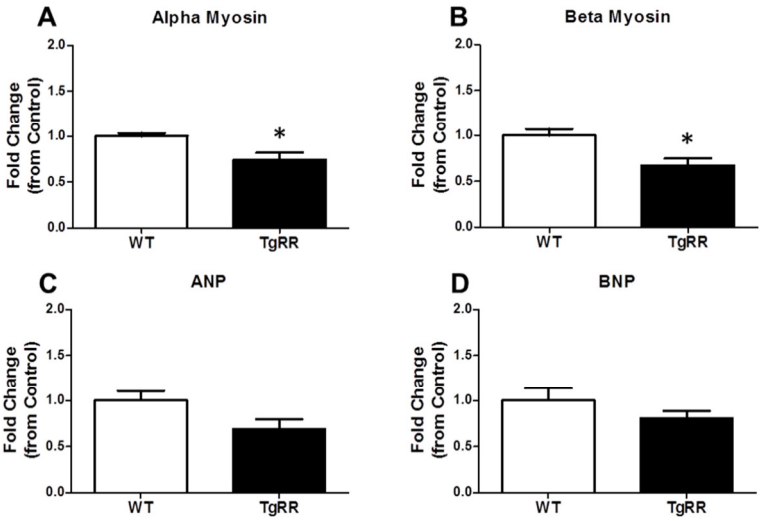

Figure 2.7. Expression of myosin isoforms and hypertorphy genes. (A) Alpha myosin heavy chain (myh6) gene expression. (B) Beta myosin heavy chain (myh7) gene expression. (C) Atrial natriuretic peptide (ANP) gene expression. (D) Brain natriuretic peptide (BNP) gene expression. Specific genes were normalized to 18s ribosomal RNA and reported as fold change over control (WT) ± SEM. * $P < 0.05$ vs. WT. n=5 each group.

The assessment of contractile function presented in this study strongly indicates that the primary effect of dATP is on the myofilament level, as Ca^{2+} transients are not affected. This conclusion is supported by previously published biochemical and mechanical studies suggesting that dATP binds to the myosin head and results in increased chemomechanical cycling. In skeletal muscle, the forward rate of crossbridge attachment and the power stroke (transition 2 in Figure 1.2: A + M.ADP.Pi → AM*ADP±Pi) and the rate of ADP release (transition 3 in Figure 1.2: AM*ADP → AM*) are increased when dATP is used as a substrate for contraction (vs. ATP) [12]. The increase in skeletal muscle contraction is relatively small compared to what we have reported for cardiac muscle containing either α- or β-myosin [11, 13, 14]. Indeed, with only 2% dATP (98% ATP; 5 mM total NTP) there is significant augmentation of force in demembranated cardiac muscle at (sub-maximal) Ca^{2+} concentrations that occur during a cardiac twitch [24]. Since dATP binding affinity is similar to that for ATP [24], we hypothesize that contractile augmentation may occur because the few myosin crossbridges utilizing dATP may bind and cycle more rapidly to actin than myosins utilizing ATP. Indeed, recent evidence suggests that small changes in the minority population of rat ventricular β-myosin content or the minority content of rabbit and human ventricular α-myosin content have a significant effect on the magnitude and rate of cardiac tissue contraction and relaxation [38, 39, 76]. It may be that the initial, rapid binding of a few myosins can augment thin filament activation, which is a highly cooperative process where initial Ca^{2+} binding allows subsequent myosin binding, and this facilitates tropomyosin movement and stabilization [47, 48] and additional Ca^{2+} binding [77, 78]. Both of these promote additional myosin crossbridge binding in a highly cooperative manner for cardiac muscle [47, 48, 79].

Interestingly, dATP appears to be an effective substrate for contraction in all three muscle types (cardiac, skeletal and smooth muscle), but its ability to enhance maximal force is restricted to cardiac muscle, where the augmentation of sub-maximal force is also most prevelant. Our studies have shown it is an effective substrate for myosins from fast and slow twitch skeletal muscle [11–13], α- and β-cardiac muscle [14, 24, 49], vascular smooth muscle (this study), and human fetal skeletal muscle.

Importantly, dATP may also be used by other cellular ATPases. It has been reported that sarcoplasmic reticulum pump (SERCA2a) activity is enhanced by dATP [80]. Here we observed similar Ca^{2+} transient decay kinetics in cardiomyocytes from TgRR vs. WT mice suggesting the level of dATP in the TgRR mice had little or no effect on SERCA2a function. However, we previously reported a small (albeit significant) increase in the rate of Ca^{2+} transient decay for cultured adult rat cardiomyocytes transduced with AV-RR to increase cellular [dATP] [24]. Thus, it is reasonable to hypothesize that other cardiomyocyte ATPases could utilize dATP for function, though it is unknown whether the affinities of these ATPases are similar or dissimilar for dATP. However, given the millimolar levels of competing ATP in the cardiomyocyte and our inability to see the dATP signal by solution NMR (Figure 2.5), it is unlikely that the levels of dATP attained in the TgRR mice (or through viral-mediated transgenesis of RR) would have a dominant effect unless there is a highly cooperative interaction with other proteins, as occurs with cardiac thin filament activation. Future studies will be required to specifically determine the global influence of dATP on cardiomyocyte function.

Previous work has shown that TgRR animals significantly overexpress both Rrm1 and Rrm2 in both cardiac and skeletal muscle compared to their WT littermates, and that this was associated with and ~10-fold increase in cellular [dATP] [25]. This is similar to the level of elevation we recently reported for cultured adult cardiomyocytes transduced with adenoviral vectors to elevate Rrm1 and Rrm2 [24]. Thus, small but significant increases in [dATP] appear to be able to increase contractility at the cell, tissue (*in vitro*), and organ (*in vivo*) levels via enhancement of both the magnitude and kinetics of myofilament contraction and relaxation. Importantly, here we demonstrate that even chronic overexpression of Rrm1 and Rrm2 (and thus chronic increases in [dATP]) do not significantly deplete energetic reserves or eliminate adrenergic responsiveness. Also important for ischemic conditions is that dATP doesn't increase vascular smooth muscle contraction, suggesting it doesn't precipitate vaso-constriction. This is important, because adequate coronary flow is required for long term enhancement of cardiac performance.

2.5 Implications for translational research

While this study was primarily focused on characterizing healthy animals with increased dATP concentration, the results compel us to consider enhancing cardiac dATP concentration as a therapy to increase the basal contractility of the heart in cases where systolic function is reduced. Heart disease is the leading cause of mortality and morbidity in the United States and has been rising dramatically around the world [81]. Many cardiopathologies, as well as ischemia-reperfusion injury and myocardial infarct result in reduced systolic function [40, 57–59]. Whether heart failure results from infarction or other diseases that reduce systolic function, the most common treatment strategies are pharmacological therapies and/or surgery. However, these strategies have significant limitations including multiple off-target drug effects, unintended drug activity within the target myocardium, and complications from surgery and recovery. Additionally, they ultimately only serve as short-term treatments that only slow progression of heart failure. Thus, novel strategies focused on recovery of function are desirable. A potential strategy is to improve basal cardiac function via direct enhancement of myofilament contractile capacity by altering substrate conditions for crossbridEge cycling. Here we have demonstrated in the first animal study considerable *in vitro* and *in vivo* evidence that increasing cardiomyocyte [dATP] increases contractility in muscle via increased (actin-myosin) crossbridge binding and cycling, which elevates basal cardiac function. This elevation persists over time in transgenic mice, whose hearts appear non-pathogenic, respond to a high workload challenge, and maintain normal myocardial energetics. Thus, further studies to test the potential of the elevated cardiac dATP approach for treatment of systolic failure are merited and are in progress by our group. These studies involve cardiac targeted treatment to avoid potential organ-specific or systemic effects of elevated Rrm1 and Rrm2 overexpression and/or dATP.

CHAPTER 3. OPTIMIZATION OF AAV6-RR VIRAL DELIVERY

3.1 Introduction

The work performed using transgenic mice (discussed in Chapter 2) demonstrated that elevated dATP concentrations *in vivo* can improve basal cardiac performance in healthy animals. In order to pursue the use of dATP as a therapy, however, we needed an approach to elevate dATP concentration following a cardiac event and not from birth (as is the case in the transgenic animals). To achieve this goal, we collaborated with Dr. Jeffrey Chamberlain's lab to develop a gene therapy that could be administered to overexpress RR *in vivo.* The design criteria for this gene therapy were: (1) achieve cardiac-specific overexpression of RR, (2) enable sustained overexpression over the long-term, and (3) avoid significant immune response following dosing. These factors were important considerations for both our research and development in small animals and for the further development of this therapy as a treatment for systolic failure in humans.

Lentivirus, adenovirus, and adeno-associated virus are able to infect non-proliferating cells, which makes them attractive for the development of a cardiac-specific gene therapy. While lentivirus elicits long-term transgene expression and does not elicit a T-cell lymphocyte immune response following administration, there are safety concerns associated with its use [82, 83]. Two primary concerns are: (1) insertional mutagenesis leading to oncogenesis resulting from the integration of lentivirus with the host genome and (2) the generation of replication competent lentivirus during production as a result of recombination during manufacturing [82, 83]. Adenoviruses have high transduction efficiencies of various subtypes *in vivo* and *in vitro*, they can be grown at large volumes, and they have a large transgene carrying capacity. Adenoviruses do not integrate with host DNA so there is no risk of insertional mutagenesis [83, 84]. The primary drawback to adenovirus is the activation of immune system associated with neutralizing antibodies against viral proteins, which results in transient transgene expression, prohibits re-administration of the virus, and can lead to death [83–85]. While adeno-associated viruses (AAV) are limited in their transgene carrying capacity, they elicit relatively low immune response, and recombinant AAV systems are replication deficient and do not integrate into the host genome so risk of mutagenesis is also low. AAV transduction also results in long-term transgene expression [26, 28, 83, 85]. For these reasons, recombinant AAV (rAAV) vectors were chosen for the development of a cardiac-specific gene therapy.

As described in section 1.3.3, AAV vectors offer distinct advantages over other viral vectors specifically in the context of cardiac gene therapy. Recent work has demonstrated that AAV serotype 6 offers a unique advantage for cardiac therapies as it favors transduction into the myocardium following systemic delivery, without affecting function or inducing inflammation [27]. While they are slower to reach steady-state expression than adenoviruses (AAV's onset of expression approaches 2-3 weeks), work with AAV2 has shown that despite this lag time, AAV2 vectors expressing a therapeutic gene were able to preserve cardiac function following ischemia-reperfusion in a porcine model [28]. Single systemic administration of AAV8 vectors carrying delta-sarcoglycan in hamsters with a congestive heart failure and muscular dystrophy associated with a delta-sarcoglycan mutation resulted in sustained transgene expression for over twelve months with associated improvements in cardiac performance.

As a proof of principle, this study was designed to test the efficacy of simultaneous administration of two recombinant AAV6 (rAAV6) vectors, each carrying a subunit of rat ribonucleotide reductase (RR) gene, to (1) overexpress RR in healthy rat hearts *in vivo,* and (2) improve cardiac performance. Administration of the virus in this study was performed using direct injection of the virus to the heart. This mode of administration was chosen to enable the use of rats as an animal model with a lower amount of virus (as compared to dose that would be needed for systemic administration in rats). We characterized *in vivo* and *ex vivo* cardiac function using echocardiography and the Neely Working Heart Apparatus, respectively, and the delivery of the virus and protein overexpression using immunohistochemistry (IHC) and Western Blots (WB). We did not observe an increase in cardiac performance by either metric, but did achieve overexpression of RR in the heart. Due to the route of administration the overexpression was limited to punctate regions in the heart. These studies motivated the further development with modifications to the route of administration and animal model. These follow-on studies are described in Chapter 4.

3.2 Materials and Methods

3.2.1 Animal model

Male, Fischer 344 rats were used in this study. All animal experiments were approved by the University of Washington (UW) Animal Care Committee and were carried out in accordance with federal guidelines. Animals were housed in the Department of Comparative Medicine at the UW and were taken care of in accordance with the US NIH Policy on Humane Care and Use of Laboratory Animals.

3.2.2 Experimental Design

Animals underwent echocardiography prior to surgery to establish a baseline assessment of cardiac function. Following surgery and administration of either the treatment or saline, animals were followed for four weeks, during which echocardiography was performed once a week. After four weeks, the animals were sacrificed and tissue was collected for assessment of protein overexpression.

3.2.3 Vector production

Vector production was carried out in collaboration with Dr. Charles Murry's, Dr. Stephen Hauschka's, and Dr. Jeffery Chamberlain's labs. Dr. Stephen's Hauschka's group has developed an optimized cardiac troponin T promoter (cTnT455) by testing activity of promoter and enhancer regions that are conserved between rat, chicken, mouse, and human cTnT. The optimal promoter, and the one used in this work, is the smallest and most active combination of enhancer and promoter regions of the human cTnT (two tandem truncated enhancers ligated to a truncated promoter). The use of a cTnT promoter will enable cardiac-specific expression of our therapeutic gene [86].

The work in this chapter was performed using a two vector system. They were simultaneously delivered at the same dose in an effort to achieve 1:1 expression. The first vector contains Kozak-cTnTpromoter-Rrm1-Stop-SV40 PolyA and the second contains Kozak-cTnTpromoter-Rrm2-Stop-SV40 PolyA. The Rrm1 and Rrm2 sequences used in this chapter are from the rat. This vector system will be referred to as Rat Rrm1 + Rrm2 throughout. Each endogenous sequence was PCR sub-cloned into the pAAV-cTnT455-hPLAP (derived from pARAP4, [87]) vector using SalI and HindIII.

Recombinant AAV6 vector was produced and prepared by Dr. Guy Odom as previously described [87, 88]. Briefly, rAAV6 vectors were produced by $CaPO_4$ co-transfection of HEK 293D cells with each of the plasmids containing either rAAV-cTnT455-Rrm1-Stop-SV40 PolyA or rAAV-cTnT455-Rrm2-Stop-SV40 Poly A vector genomes flanked by AAV2 ITR's and pDGM6 packaging/helper genes [89]. Cells were harvested and processed through a microfluidizer (Microfluidics, Newton, MA), filtered through a 0.22. µm filter, and vector particles being purified by affinity chromatography on a HiTrap heparin column (GE Healthcare, Chalfont St. Giles, UK). Following elution from the column, recombinant AAV6 vectors were further concentrated layering onto a 40% sucrose gradient by ultracentrifugation at 27,000 RPM for 18 hours at 4°C, followed by solubilization in HBSS (Invitrogen, Carlsbad, CA). Vector genome titer was

determined by Southern blot analysis with a DNA standard of known quantity using a ^{32}P-labeled oligonucleotide probe to the poly-adenylation region (5'-TGAATAAAAGATCCTTA-3').

3.2.4 Vector administration

The protocol for direct cardiac injection has been previously described by our collaborators in the Murry Lab [90, 91]. Rats were anesthetized with 5% inhaled isoflurane, intubated and mechanically ventilated with 2-5% isoflurane supplemented with oxygen. The heart was exposed through a thoracotomy and the chest wall was kept open with a retractor. A total of 70 µl of $2x10^{12}$ vector genomes suspended in Hank's Buffered Saline Solution (HBSS) or 70 µl of saline alone was injected at three unique sites using an insulin syringe with a 29-gauge needle.

3.2.5 Echocardiography

The animals were lightly anesthetized using 1% isofluorane. Images were collected with a GE Vivid 7 system using 13MHz linear transducer (General Electric Healthcare). Left ventricular end-diastolic (LVEDD) and left-ventricular end-systolic (LVESD) dimensions were determined using M-mode measurements obtained by short-axis views at the mid-papillary level. All data were averaged from at least three cardiac cycles. Fractional shortening was calculated from these data using the formula: (LVEDD-LVESD)/LVEDD x 100. All echocardiography was carried out by a single reader who was blinded to the genotype of the animals.

3.2.6 Histological Analysis

Animals were lightly anesthetized using 1% isolflurane and 0.1 ml beuthanasia. Hearts were rapidly excised, rinsed in PBS, and sliced into 2 mm thick short-axis sections. A minimum of three sections were taken from each heart, starting at the apex. All sections were fixed in formalin, processed, and paraffin-embedded. 5, 4 µm slices were taken from each 2 mm section.

Immunostaining was performed with primary antibodies against Rrm1 (Goat polyclonal anti-R1 (1:50), Santa Cruz Biotechnology). Samples were then labeled with a biotinylated rabbit anti-Goat (1:500) secondary antibody (Pierce Antibodies) and developed with DAB (Sigma-Aldrich).

3.2.7 Protein preparation and Western Blotting

Excised mouse hearts were rinsed in PBS, and flash frozen in liquid nitrogen for subsequent Western Blot analysis. Total protein was isolated from left ventricular cardiac tissue via homogenization and lysis.

Samples were loaded into a 10% SDS-PAGE gel (BioRad) and run at 200V on ice for 55 minutes. Protein samples were then transferred to nitrocellulose using a standard western blot apparatus (BioRad). The nitrocellulose membranes were then blocked in 5% milk TBS-T and incubated with primary antibody in 1% milk TBS-T (R1 (t-16) Goat polyclonal IgG, 1:500, Santa Cruz Biotechnology; GAPDH Rabbit polyclonal IgG, 1:1000,Rockland). Following wash, secondary antibody was applied to the blots in 1% milk TBS-T (bovine anti-goat IgG-HRP, 1:1,000, Santa Cruz Biotechnology; goat anti-rabbit IgG-HRP, 1:2500, Santa Cruz Biotechnology). Following secondary antibody incubation and wash, membranes were exposed to Pierce ECL Western Blotting Substrate (Thermo Scientific) and subsequently exposed to photography film. The membrane was stripped after each exposure (Restore Western Blot Stripping Buffer, Thermo Scientific). Rrm2 overexpression was not assessed in this study, as a reliable anti-Rrm2 antibody with reactivity for the rat sequence was not available. We expect similar expression of Rrm1 and Rrm2.

3.3 Results

3.3.1 Echocardiography

In vivo cardiac function was assessed via echocardiography for both RR-injected and saline-injected rats. There was no observable difference in cardiac function or in cardiac dimension between the rats that received a direct injection of RR versus those that did not (Table 3.1).These data could suggest that either viral administration did not result in RR overexpression in the heart, that RR overexpression did not result in increased dATP in the heart, that there was not sufficient overexpression of RR in the heart, that echocardiography is not sufficiently sensitive to discern an improvement in cardiac function, or that overexpression of RR and elevated dATP does not improve basal cardiac performance in healthy rats *in vivo.* Based on our previous work, we are confident that if there were sufficient overexpression of RR and elevation of dATP concentration *in vivo*, we would observe an increase in cardiac function. We, therefore, sought to examine the extent of RR overexpression in these animals.

Table 3.1. Echocardiographic measurements of control rats or rats treated with direct myocardial injection of rAAV6-RR. LVID;d: LV internal dimension in diastole, LVID;s: LV internal dimension in systole, FS: fractional shortening, HR: heart rate. Data are presented as mean ± SD (Control n=6, RR n=6).

	Baseline		4 weeks post-treatment	
	Control	RR	Control	RR
LVID;d (mm)	6.0 ± 0.3	6.0 ± 0.3	6.3 ± 0.1	6.4 ± 0.1
LVID;s (mm)	3.1 ± 0.2	3.3 ± 0.2	3.4 ± 0.2	3.4 ± 0.2
FS (%)	48.1 ± 1.4	45.7 ± .1	46.0 ± 2.8	46.5 ± 2.5
HR (bpm)	372 ± 1.9	354.2 ± 0.9	346 ± 1.2	354 ± 5

3.3.2 Histology

Histological assessment of RR-treated and control hearts showed no appreciable difference in myocyte size, organization, or fibrosis between groups. We did detect significant overexpression of R1 around the injection sites. Injection sites could be identified based on the visible immune response that occurred around the area. R1 overexpression was contained to punctate regions immediately around these sites, and did not extend further into the myocardium. Our conclusions from these data are that vector administration resulted in overexpression of RR in the heart. However, given the echocardiographic data, direct myocardial injection may limit distribution of vector genomes and prevent sufficient RR overexpression to improve cardiac performance (Figure 3.1)

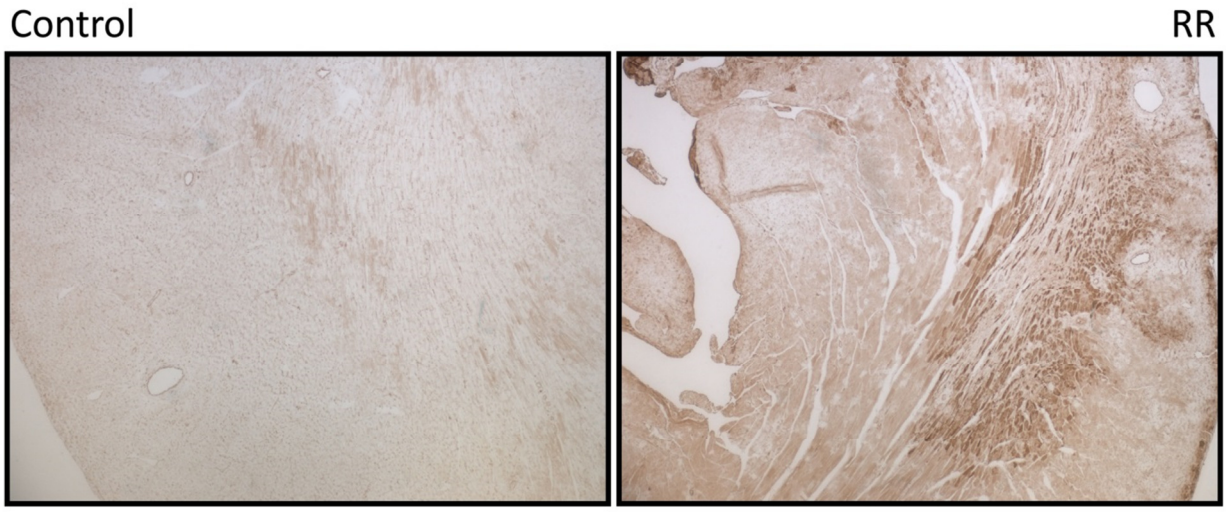

Figure 3.1. Histological assessment of control hearts and hearts treated with direct myocardial injection of rAAV6-RR. Representative cardiac sections from 3-5 month old mice, 4 weeks after treatment were stained with anti-Rrm1. Anti- Rrm1 stained section taken at 4x, control section on the left and RR-treated on the right. Note the punctate region of Rrm1 overexpression.

3.3.3 Western blotting

Western blot analysis of cardiac tissue showed overexpression of RR, which supports the histological assessment above (Figure 3.2).

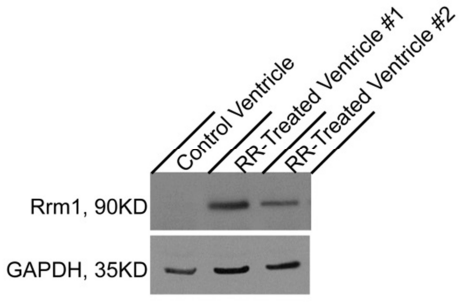

Figure 3.2. Assessment of Rrm1 protein overexpression in hearts from control rats or rats treated with direct myocardial injection of rAAV6-RR. Western blot of the rat Rrm1 + Rrm2-treated animals vs. control. Probing for Rrm1, and a loading control, GAPDH, shows that there is significant overexpression of Rrm1 in these animals. There is no Rrm2 antibody against the rat sequence so we could not assess the levels of Rrm2 in the mice treated with this vector.

3.4 Discussion

Even though we did not achieve the functional results we expected in this study, we demonstrated that direct myocardial injections of rAAV6 resulted in overexpression of RR in the heart. Furthermore, we noted a punctate overexpression of RR that was limited to the injection site. We, therefore, hypothesize based on these data that a systemic injection approach should be used in the future in order to achieve widespread overexpression of RR evenly distributed throughout the heart. Importantly, we did not rule out the following factors as potential reasons for the lack of RR-mediated improvement in cardiac function: (1) echocardiography is not sufficiently sensitive to discern small improvement in cardiac function and (2) improvement in basal cardiac function may not be discernible *in vivo* due to intrinsically high *in vivo* performance and/or hormonal regulation or compensation. For a comprehensive discussion of this topic, please refer to Section 4.4 and Table 4.8.

In order to use a systemic injection model in the future, we will move into mouse models where retro-orbital administration of virus can be used. Furthermore, due to their small size, mice require far less virus (when systemically administered) than rats to achieve the desired dose. The subsequent work reported on the viral system in small animals will be in a mouse model.

CHAPTER 4. AAV6-MEDIATED OVEREXPRESSION OF RR INCREASES MYOCARDIAL DATP AND IMPROVES CARDIAC FUNCTION IN NORMAL AND INFARCTED MICE

4.1 Introduction

Left ventricular dysfunction contributes to the decompensation that leads to heart failure in the majority of cases. It is hypothesized, therefore, that therapies that can improve left ventricular function may be able to prevent or reverse heart failure. Inotropic agents are one such class of therapies. They increase the force of contraction of the ventricle and were, thus, expected to have great success in treating cardiac disease. Their use has surprisingly not proven efficacious in the clinic, which is thought to be at least partially attributable to adverse effects related to their mechanism: increasing intracellular calcium [10]. Use of inotropic therapies has been shown to increase the number of adverse events and, in some cases increase mortality, often as a result of increased myocardial oxygen demand or arrhythmia [8–10]. The work presented here details the characterization of a novel inotrope that is specifically targeted to the myofilament, and results in an increase in force production without an increase in intracellular calcium. We propose that this approach to increase force production has the potential to improve left ventricular function in patients with cardiac disease without excessive off-target effects that limit the currently available therapies.

We have previously demonstrated that 2-deoxy-ATP (dATP) increases contractility in single cells [24], and muscle strips *in vitro* [11, 12, 49], and increases left ventricular developed pressure in transgenic mice [92] by increasing the hydrolytic activity of myosin [13]. In order to adapt this approach to a therapy, we designed an adeno-associated virus with a cardiac Troponin T (TnT) promoter that results in cardiac-specific overexpression of ribonucleotide reductase, the enzyme that catalyzes the production of dATP (introduced in Chapter 3). This work is focused on both characterizing the expression of the systemically administered recombinant adeno-associated viral (rAAV) system in a healthy mouse model, and on investigating the therapeutic potential of the rAAV system to restore cardiac function following myocardial infarction in mice. The data presented here demonstrate that cardiac-specific overexpression of ribonucleotide reductase can be obtained via systemic administration of an rAAV with a cardiac TnT promoter, and that this therapy is sufficient to improve *ex vivo* cardiac performance in healthy mice. In the chronic infarct model the rAAV6-RR therapy improved cardiac performance compared to pre-treatment by 24% when assessed four weeks after treatment and by 16% when

assessed eight weeks after treatment versus the cardiac performance of control mice, which improved by 3% and 7% at the same time points. While this improvement was not statistically significant ($p = 0.15$ at four weeks post-treatment and $p = 0.44$ at eight weeks post-treatment), it does indicate that there may be an effect of treatment. We propose that the lack of statistical significance of the between group comparisons is due to high inter-animal variability as a result of infarct surgery and low power ($n = 7$ control, $n = 6$ RR). Further assessment of the data and interpretation of the results can be found in sections 4.3.3-4.5 below.

4.2 Materials and Methods

4.2.1 Animal Model

Three to five month old C57Bl/6 mice were used in all studies presented in this chapter. All animal experiments were approved by the University of Washington (UW) Animal Care Committee and were carried out in accordance with federal guidelines. Animals were housed in the Department of Comparative Medicine at the UW and were taken care of in accordance with the US NIH Policy on Humane Care and Use of Laboratory Animals.

4.2.2 Infarct model

After inducing anesthesia with injection anesthetic Avertin (0.015 ml/gram body weight), the hair was removed with Nair, and the then prepped with triple application of alternating betadine and sterile saline water. Ophthalmic ointment was applied to prevent corneal drying and abrasion. The animals were orotracheally intubated and supported with a mechanical ventilator using room air supplemented with oxygen. The animals were placed on a 38°C water blanket to maintain body temperature throughout the procedure. The surgical field was draped with sterile gauze, and a left thoracotomy was performed by making a vertical incision through ribs 3-6. The chest was opened with a retractor and the pericardium incised to expose the heart. The left coronary artery was ligated near its origin. Successful ischemia was assessed by observing when the myocardial region distal to the ligation site became pale and blanched. The chest was then closed.

Subcutaneous 0.9% saline (0.5 ml) was given routinely to each animal immediately post-op. Animals were held for observation in a warm environment until they recovered from anesthesia. Buprenorphine (0.05 mg/kg) was administered twice a day as a subcutaneous injection for two days following surgery. Animals were monitored twice daily for the first week after surgery.

Sham surgeries were also performed on some mice. These animals underwent the same pre-surgery routine and a thoracotomy with pericardium incision but did not undergo ligation of the left coronary artery. They received the same post-operative care as the infarcted animals.

4.2.3 Vector production

Vector production was carried out in collaboration with Dr. Charles Murry's, Dr. Stephen Hauschka's, and Dr. Jeffery Chamberlain's labs. Dr. Stephen's Hauschka's group has developed an optimized cardiac troponin T promoter (cTnT455) by testing activity of promoter and enhancer regions that are conserved between rat, chicken, mouse, and human cTnT. The optimal promoter, and the one used in this work, is the smallest and most active combination of enhancer and promoter regions of the human cTnT (two tandem truncated enhancers ligated to a truncated promoter). The use of a cTnT promoter will enable cardiac-specific expression of our therapeutic gene [86]. Dr. Hans Reinecke of the Murry Lab developed codon-optimized sequences for three vectors, each containing a different combination/order of human Rrm1 and human Rrm2. Two of them also contained a picornaviral 2a sequence (P2a) is a small peptide linker (20 amino acids) that enables co-translation of two proteins from a single strand of mRNA. It leverages a ribosomal skipping mechanism, which results in cleavage of the two proteins (in our case, the two RR subunits). The P2a peptide remains attached to the C-terminus of the upstream protein. This system ensures a 1:1 expression of the two subunits, driven by the same promoter [93, 94]. We leveraged the P2a peptide to combine the Rrm1 and Rrm2 genes into one vector. Because the P2a peptide attaches to the upstream protein, we wanted to test vector systems with each subunit first.

The three vectors synthesized were: (1) R1.2, which contains the sequence for Kozak-cTnTpromoter-Rrm1-P2a-Rrm2-Stop-polyAsignal, (2) R2.1, which contains the sequence for Kozak-cTnTpromoter-Rrm2-P2a-Rrm1-Stop-polyAsignal, and (3) Human Rrm1 + Human Rrm2, which is a two-vector system analogous to that in Chapter 3. The first is Kozak-cTnTpromoter-Rrm1-Stop-polyAsignal and the second is Kozak-cTnTpromoter-Rrm2-Stop-polyAsignal. Each of these sets of sequences was synthesized by Genscript (Piscataway, NJ) and then cloned into a pAAV-hrGFP recipient vector (Stratagene, La Jolla, CA) with the GFP released by a NotI/NotI cut.

Recombinant AAV6 vector was produced and prepared by Dr. Guy Odom as previously described [87, 88]. Briefly, rAAV6 vectors were produced by $CaPO_4$ co-transfection of HEK 293D cells with each of the

plasmids containing either rAAV-cTnT455-RR1.2-Stop-polyAsignal, rAAV-cTnT455-RR2.1-Stop-polyAsignal, rAAV-cTnT455-RR1-Stop-polyAsignal, or rAAV-cTnT455-RR2-Stop-polyAsignal vector genomes (as described above) flanked by AAV2 ITR's and pDGM6 packaging/helper genes [89]. Cells were harvested and processed through a microfluidizer (Microfluidics, Newton, MA), filtered through a 0.22. μm filter, and vector particles being purified by affinity chromatography on a HiTrap heparin column (GE Healthcare, Chalfont St. Giles, UK). Following elution from the column, recombinant AAV6 vectors were further concentrated layering onto a 40% sucrose gradient by ultracentrifugation at 27,000 RPM for 18 hours at 4°C, followed by solubilization in HBSS (Invitrogen, Carlsbad, CA). Vector genome titer was determined by Southern blot analysis with a DNA standard of known quantity using a ^{32}P-labeled oligonucleotide probe to the poly-adenylation region (5'-TGAATAAAAGATCCTTA-3').

4.2.4 Vector administration

200 μl of virus ($2x10^{12}$ vector genomes in Hanks Buffered Saline Solution, HBSS) or HBSS alone was administered to mice under isofluorane anesthesia via retro-orbital injection.

There are two study designs discussed in this chapter. In studies using healthy mice, 3-5 month old mice were dosed with virus or saline as described above and followed for 4 weeks after treatment. Infarcted mice were treated 4-5 weeks following infarction and followed for 8 weeks after treatment.

4.2.5 Histological Analysis

Animals were lightly anesthetized using 1% isolflurane and 0.1 ml beuthanasia. Hearts were rapidly excised, rinsed in PBS, and sliced into 3, 2 mm thick short-axis sections. The middle section was immersion fixed in formalin, processed, embedded in paraffin and sectioned (4 um) for histological analysis.

Sections were stained with H&E or immunostained with antigen-retrieval, using primary antibodies against Rrm1 (Goat polyclonal anti-R1 (1:50), Santa Cruz Biotechnology). Samples were then labeled with a biotinylated rabbit anti-Goat (1:500) secondary antibody (Pierce Antibodies) and developed with DAB (Sigma-Aldrich).

4.2.6 Isolated perfused heart preparation

Myocardial energetics and LV function were measured in Langendorff isolated heart preparations as previously described [65–67]. In brief, excised mouse hearts were perfused at a constant pressure of 80mmHg with a modified Krebs Henseleit (KH) buffer consisting of (mmol/L): 118 NaCl, 25 $NaHCO_3$, 5.3 KCl, 2.0 $CaCl_2$, 1.2 MgSO4, 0.5 EDTA, 5.5 glucose, and 0.5 pyruvate, equilibrated with 95% O_2 and 5% CO_2 (pH 7.4). Temperature was maintained at 37.5°C throughout the protocol. After 20 minutes of equilibration, baseline function was monitored for 10 minutes at a fixed end diastolic pressure (EDP) of 8-10mmHg by way of a water-filled balloon inserted into the left ventricle (LV). After baseline, dobutamine (DOB) and calcium were infused at 5% of the coronary flow at a final concentration of 4mM calcium and 50nM DOB for 20 minutes.

4.2.7 Echocardiography

The animals were lightly anesthetized using 1% isofluorane. Images were collected with a GE Vivid 7 system using 13MHz linear transducer (General Electric Healthcare). Left ventricular end-diastolic (LVEDD) and left-ventricular end-systolic (LVESD) dimensions were determined using M-mode measurements obtained by short-axis views at the mid-papillary level. All data were averaged from at least three cardiac cycles. Fractional shortening was calculated from these data using the formula: (LVEDD-LVESD)/LVEDD x 100. All echocardiography was carried out by two readers who were blinded to the animal groups. The data from the two reviewers was averaged to formulate the data set presented below.

Animals were separated into two treatment groups (saline and AAV6-RR) after the 4 week post-infarction echo. Based on the following criteria: (A) > 15% decrease in fractional shortening between baseline (pre-infarction) and 4 weeks post-infarction, (B) infarct region visible on 4 week post-infarct echo, and (C) 4 week post-infarct fractional shortening was below 30%.

4.2.8 Cardiac MRI

Twelve weeks following infarction animals were studied by high-resolution MRI using a 14T NMR spectrometer (Bruker BioSpin MRI GmbH, Germany) in collaboration with Dr. Anna Naumova. Mice were anesthetized with 1.5% isoflurane in oxygen (1 liter/min) delivered through a nose cone, and placed in a 25 mm ^{1}H volume coil. Needle electrodes were attached to animal's extremities for ECG monitoring and to trigger the MRI acquisitions using commercial software ("Small Animal Monitoring

and Gating System" SA Instrument Inc., Stony Brook, NY). High-resolution FLASH CINE short-axis ^{1}H MR images were obtained to quantify left ventricular function. Image acquisition parameters: field of view (FOV) of 25 mm^2; 2D matrix of 256x256; slice thickness 1 mm without gap between slices, 36 cardiac phases for 8–10 short axis slices spanning the left ventricle, repetition time (TR) 6 ms; echo time (TE) 1.8 ms; flip angle (FA) 25 degree, 4 signal averages, in-plane resolution 0.09 mm^2.

For analysis of heart function, epicardial and endocardial borders were manually traced for calculation of left ventricle volumes at end systole and end diastole (ESV, EDV) and left ventricular mass (LVmass) using the software package Medviso Segment Software (Medviso, Lund, Sweeden). Total LV volumes were calculated as the sum of all slice volumes. The left ventricular ejection fraction (EF) was calculated from the relative difference in end-diastolic and end-systolic cavity volumes. Two blinded readers measured all images and their measurements were averaged and reported as mean ± standard deviation.

4.2.9 DNA isolation and qPCR

Total DNA was isolated from snap frozen heart tissue (stored at -80°C) using the DNeasy Mini Kit (Qiagen) according to manufacturer's guidelines. qPCR was performed using iTaq™ Universal Probes Supermix (Bio-Rad) with the following primer sequences:
RR F (cTNT promoter): CCCAGTCCCCGCTGAGA, R (RR1): AGGTTCCAGGCGCTGCT
Pax7: F: CAAGGCCGGGTCAATCAG, R: AGATGACACAGGGCCGGA

PCR was performed on ABI 7900HT-Fast Real-Time PCR System (Applied Biosystems, Foster City, CA). With a total well volume of 15 µl (5 µl sample DNA, 7.5 µl 2x iTaq Universal PCR SuperMix (Applied Biosystems, Foster City, CA), 0.15 µM of each primer, 0.075 µM TaqMan custom probe (Applied Biosystems, Foster City, CA), and 2.215 µl dH_2O). Reaction conditions were 50°C for 2 minutes, 95°C for 10 minutes, and 40 cycles of [95°C for 15 seconds followed by 60°C for 1 minute].

All samples were run in triplicates, and average quantities are reported unless otherwise indicated. A standard curve was run on each plate including six samples run in triplicate. Vector genomes per nuclei were calculated by normalizing to Pax7 genomes in each sample. There are two copies of Pax7 per nuclei, so the total number of vector genomes of RR was divided by the amount of Pax7 divided by two in order to obtain the number of RR vector genomes per nuclei.

4.2.10 Protein preparation and Western Blotting

Excised mouse hearts were rinsed in PBS, and flash frozen in liquid nitrogen for subsequent Western Blot analysis. Total protein was isolated from left ventricular cardiac tissue via homogenization and lysis. Samples were loaded into a 10% SDS-PAGE gel (BioRad) and run at 200V on ice for 55 minutes. Protein samples were then transferred to nitrocellulose using a standard western blot apparatus (BioRad). The nitrocellulose membranes were then blocked in 5% milk TBS-T and incubated with primary antibody in 1% milk TBS-T (R1 (t-16) Goat polyclonal IgG, 1:500, Santa Cruz Biotechnology; R2 (E-16) Goat polyclonal IgG, 1:500, Santa Cruz Biotechnology; GAPDH Rabbit polyclonal IgG, 1:1000,Rockland). Following wash, secondary antibody was applied to the blots in 1% milk TBS-T (bovine anti-goat IgG-HRP, 1:1,000, Santa Cruz Biotechnology; goat anti-rabbit IgG-HRP, 1:2500, Santa Cruz Biotechnology). Following secondary antibody incubation and wash, membranes were exposed to Pierce ECL Western Blotting Substrate (Thermo Scientific) and subsequently exposed to photography film. The membrane was stripped after each exposure (Restore Western Blot Stripping Buffer, Thermo Scientific). Protein band density was quantified using open access software, Image J (NIH). Each band was normalized to the protein standard, GAPDH.

4.3 Results

4.3.1 Vector development

The approach described in Chapter 3 was a two-vector system – one contained the rat Rrm1 gene and the other contained the rat Rrm2 gene. Both were driven by a cTnT promoter (referred to as rat Rrm1 + Rrm2 throughout). When used, both vectors were administered at the same dose and volume with the goal of achieving stoichiometric expression of Rrm1 and Rrm2. In an effort to develop a more translational system, we were interested in building vectors with the human Rrm1 and Rrm2 genes. Furthermore, we were interested in combining the two subunits onto one vector, which was previously not done due to size limitations of the AAV6 system. To that end, in collaboration with Dr. Jeff Chamberlain's lab, we developed three additional vectors. The first is a system identical to that described in Chapter 3 except it contained the human Rrm1 and Rrm2 (cTnT-human Rrm1 + cTnT-human Rrm2; referred to as human Rrm1 + Rrm2 throughout). The second is a single vector that contains a cTnT promoter, followed by the human Rrm1 gene, followed by a picornaviral 2a sequence, followed by the human Rrm2 gene (referred to as human R1.2 throughout). The picornaviral 2a sequence (P2a) is a small peptide linker (20 amino acids) that enables co-translation of two proteins from a single strand of mRNA. It leverages a ribosomal skipping mechanism, which results in cleavage of the two proteins (in

our case, the two RR subunits). The P2a peptide remains attached to the C-terminus of the upstream protein. This system ensures a 1:1 expression of the two subunits, driven by the same promoter [93, 94]. Because the P2a peptide attaches to the upstream protein, we also wanted to test a vector system with the two subunits reversed; this system has the cTnT promoter, followed by the human Rrm2 gene, followed by a picornaviral 2A sequence, followed by the human Rrm1 gene (referred to as human R2.1 throughout).

In order to assess the transduction efficiency and functional effects of these four vectors (rat Rrm1 + Rrm2, human Rrm1 + Rrm2, human R1.2, and human R2.1), we performed two studies in healthy mice. Both studies had the same design; one was performed to assess the rat Rrm1 + Rrm2 (n=4) vs. saline (n=4) and the other to assess the three human vectors (n=4 in each group) vs. saline (n=3). In all cases, 3-5 month old animals were treated with either $2x10^{12}$ vector genomes in Hanks Buffered Saline Solution (HBSS) or equivolume HBSS. Mice were followed for 4 weeks following treatment. Echocardiography was used to assess cardiac function once per week. *Ex vivo* function was assessed using Langendorff isolated heart preparations four weeks following treatment. Tissue was also preserved to assess protein overexpression using Western Blot.

Echocardiography

Echocardiographic analysis of left ventricular dimensions and fractional shortening did not show any difference between any of the groups (% FS values from study with virus with rat sequence: 34.1 ± 2.6 control, 35.1 ± 2.7 Rat Rrm1 + Rrm2, Table 4.1Table 4.1; % FS values from study with virus with human sequence: 30.8 ± 0.8 control, 33.7 ± 1.9 Human Rrm1 + Rrm2, 32.0 ± 2.2 R1.2, 31.2 ± 1.5 R2.1, Table 4.2;). There are a number of reasons that could explain this outcome ranging from issues with our hypothesis, to issues with the virus, to issues with the image analysis. These matters are discussed in detail in the discussion section Table 4.8.

Table 4.1. Echocardiographic measurements obtained in control and rAAV6-RR-treated (rat sequence) healthy mice. All viruses used here contained the human sequences of RR. LVID;d: LV internal dimension in diastole, LVID;s: LV internal dimension in systole, FS: fractional shortening, HR: heart rate. Data are presented as mean ± SD (Control n=3, Rrm1 + Rrm2 n=4, R1.2 n=4, R2.1 n=4).

	Baseline		4 weeks post-treatment	
	Control	RR	Control	RR
LVID;d (mm)	4.0 ± 0.1	3.8 ± 0.1	4.0 ± 0.2	4.0 ± 0.2
LVID;s (mm)	2.6 ± 0.1	2.5 ± 0.2	2.6 ± 0.2	2.6 ± 0.1
FS (%)	35.9 ± 2.6	36.1 ± 3.0	34.1 ± 2.6	35.1 ± 2.7
HR (bpm)	553 ± 35	587 ± 15	572 ± 75	551 ± 36

Table 4.2. Echocardiographic measurements obtained in control and rAAV6-RR-treated (human sequence) healthy mice. All viruses used here contained the human sequences of RR. LVID;d: LV internal dimension in diastole, LVID;s: LV internal dimension in systole, FS: fractional shortening, HR: heart rate. Data are presented as mean ± SD (Control n=3, Rrm1 + Rrm2 n=4, R1.2 n=4, R2.1 n=4).

	Baseline				4 weeks post-treatment			
	Control	Rrm1 + Rrm2	R1.2	R2.1	Control	Rrm1 + Rrm2	R1.2	R2.1
LVID;d (mm)	4.0 ± 0.2	4.2 ± 0.1	4.0 ± 0.1	4.1 ± 0.3	4.3 ± 0.1	3.9 ± 0.1	4.0 ± 0.2	4.1 ± 0.2
LVID;s (mm)	2.9 ± 0.1	2.9 ± 0.0	2.9 ± 0.2	2.9 ± 0.3	2.9 ± 0.0	2.6 ± 0.1	2.7 ± 0.3	2.9 ± 0.2
FS (%)	28.4 ± 1.7	29.7 ± 1.7	28.6 ± 3.9	28.5 ± 1.5	30.8 ± 0.8	33.7 ± 1.9	32.0 ± 2.2	31.2 ± 1.5
HR (bpm)	527 ± 16	508 ± 33	499 ± 38	497 ± 26	496 ± 11	522 ± 16	508 ± 30	497 ± 31

Langendorff isolated heart preparations

Langendorff isolated heart preparations were used to assess *ex vivo* cardiac function in 3-5 month old healthy mice under basal (all groups) and high workload conditions (only in human viruses vs. control study). Although there are similar conclusions from both studies, the section below is divided to discuss the data from the rat virus vs. control and from the human viruses vs. control separately in an effort to ensure clarity.

Rat Rrm1 + Rrm2 vs. Control. Mice dosed with rat Rrm1 + Rrm2 had significantly enhanced basal cardiac function (left ventricular developed pressure, LVDevP) compared to control mice dosed with saline (131.2 ± 6.2 mmHg treated vs. 101.1 ± 9.1 mmHg control, $p < 0.05$) (Figure 4.1. A) The heart rate (HR) of rat Rrm1 + Rrm2 animals was unchanged versus control (349.8 ± 18.9 bpm treated vs. 381.5 ± 35.4 bpm) (Figure 4.1. B). A measure of overall cardiac work, the rate pressure product (HR times LVDevP), was also significantly elevated in rat Rrm1 + Rrm2 mice versus control (45830.8 ± 1973.0 mmHg*bpm RR vs. 38404.1 ± 3097.6 mmHg*bpm, $p < 0.05$) (Figure 4.1. C). The rate of ventricular pressure development, +dP/dt, was also significantly elevated at baseline in animals dosed with rAAV6-RR (rat Rrm1 + Rrm2) (4681.0 ± 444.9 mmHg/s treated vs. 3576.0 ± 269.7 mmHg/s, $p < 0.05$), however the rate of ventricular relaxation (pressure loss) was unchanged (-3961.5 ± 467.3 mmHg/s treated vs. -3374.5 ± 529.4 mmHg/s) (Figure 4.1. E,F). These data are consistent with those obtained from assessing the *ex vivo* cardiac function in TgRR mice described in Section 2.2.7, and demonstrate that treatment with rAAV6-RR (rat Rrm1 + Rrm2) via systemic injection significantly improves basal cardiac function in healthy mice.

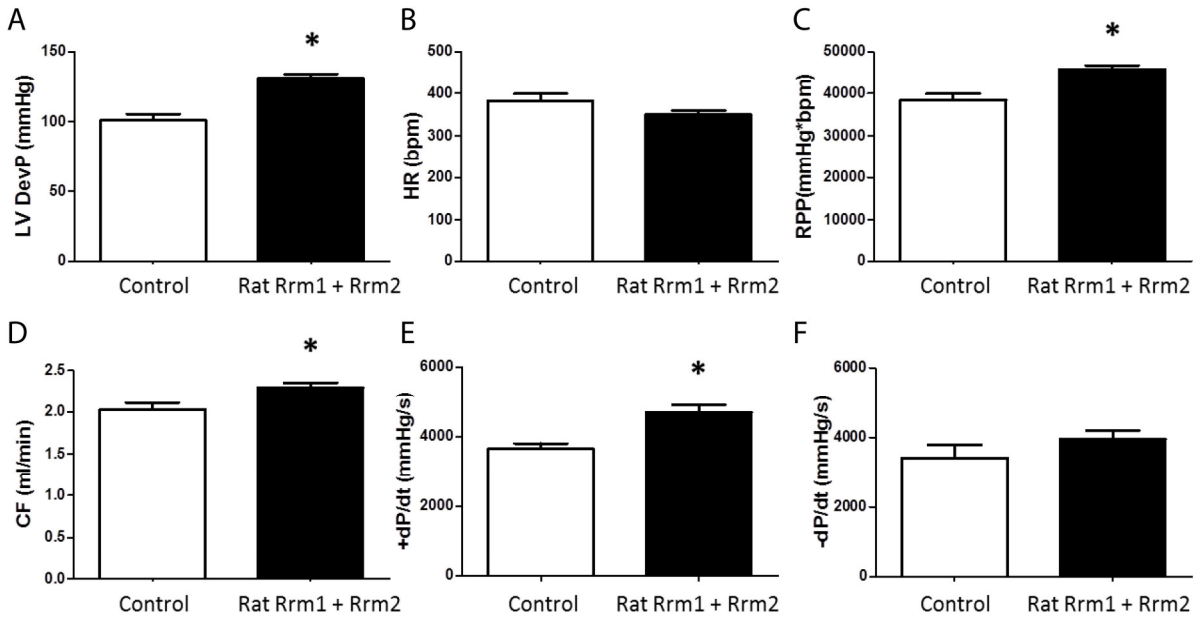

Figure 4.1. Baseline cardiac function of control animals vs. animals treated with rat Rrm1 + Rrm2 as assessed by Langendorff perfused heart apparatus. (A-C) Left ventricular developed pressure (LVDevP), heart rate (HR), and rate-pressure product (RPP), the product of LVDevP and HR, measured in isolated hearts perfused at baseline (BL). (D) Coronary flow, estimated by collecting the perfusate effluent over a 2-minute period, in Langendorff heart preparations during normal workload. (E,F) Rate of pressure change calculated by the first derivative of the LV pressure wave (dP/dt) in Langendorff heart preparations at baseline and during high calcium + DOB infusion. The positive maximum (+dP/dt) is an index of the rate of LV pressure development. The negative maximum (-dP/dt) is an index of the rate of ventricular relaxation. *p< 0.05 vs. control at BL, n=4 RR and n=4 control.

Human rAAV6-RR vectors vs. Control. Mice dosed with any of the human rAAV6-RR viruses had significantly enhanced basal cardiac function (left ventricular developed pressure, LVDevP) compared to control mice dosed with saline (Table 4.3). The heart rate (HR) of all treated animals was unchanged versus control (Table 4.3). The rate pressure product was also significantly elevated in all treated mice versus control (Table 4.3). The rate of contractility, +dP/dt, was also significantly elevated at baseline in animals dosed with human Rrm1 + Rrm2 and human R1.2. Mice treated with human R2.1 had slightly increased +dP/dt vs. control, but the difference was not significant (4722 ± 644.7 mmHg/s R2.1 vs. 3667.3 ± 486.4 mmHg/s, p = 0.057) (Table 4.3). Similar to the TgRR data discussed in Section 2.2.7, and the rat Rrm1 + Rrm2 data discussed above, there was no change in the rate of ventricular relaxation (-dP/dt) for human R1.2 and human R2.1 vs. control. There was, surprisingly, a significant difference in –dP/dt for human Rrm1 + Rrm2 vs. control (-4874.8 ± 503.5 mmHg/s treated vs. -3642.0 ± 570.2 mmHg/s, p=0.04) (Table 4.3). These data are generally consistent with those obtained from assessing the *ex vivo* cardiac function in TgRR mice described in Section 2.3.3 and with the rat Rrm1 + Rrm2

discussed above, and demonstrate that treatment with rAAV6-RR (human Rrm1 + Rrm2. human R1.2, human R2.1) via systemic injection significantly improves basal cardiac function in healthy mice.

Table 4.3. *Ex vivo* cardiac function measurements from Langendorff perfused heart apparatus on animals treated with human rAAV6 vs. control. BL measurements of left ventricular developed pressure (LVDevP), heart rate (HR), rate-pressure product (RPP; the product of LVDevP and HR), coronary output (estimated by collecting the perfusate effluent over a 2-minute period), rate of pressure change (calculated by the first derivative of the LV pressure wave (dP/dt)). The positive maximum (+dP/dt) is an index of the rate of LV pressure development. The negative maximum (-dP/dt) is an index of the rate of ventricular relaxation. *p< 0.05 vs. control at BL, n=4 Rrm1 + Rrm2, n=4 R1.2, n=4 R2.1, and n=4 control. *p < 0.05 versus control hearts.

	Baseline Measurements			
	Control	Human Rrm1 + Rrm2	Human R1.2	Human R2.1
LVDevP	118.1 ± 7.4	153.9 ± 8.1*	141.2 ± 5.8*	141.7 ± 4.0*
HR	376 ± 19	366 ± 18	400 ± 42	376 ± 6
RPP	44389 ± 3282	56296 ± 2211*	56574 ± 7059*	53229 ± 1946*
CO	2.3 ± 0.3	2.6 ± 0.5	2.6 ± 0.2	2.1 ± 0.1
+dP/dt	3667.3 ± 486.4	5304.0 ± 671.2*	4961.3 ± 460.8*	4722.5 ± 644.7
-dP/dt	-3642.0 ± 570.2	-4874.8 ± 503.5*	-4471.5 ± 811.0	-4201.8 ± 644.7

To determine whether administration of any of the human rAAV-RR vectors altered β-adrenergic responsiveness, we assessed cardiac performance under high workload conditions (dobutamine plus high calcium infusion). Similar to the response of the TgRR hearts to dobutamine described in section 2.3.3 LVDevP, HR, RPP, cardiac output, +dP/dT, and –dP/dT (Figure 4.2) were significantly increased in both control and treated hearts by ten minutes following infusion, demonstrating the expected response to β-adrenergic stimulus. However, as the HR approached 500 bpm after 5-10 minutes of high calcium and dobutamine infusion (Figure 4.2 B) LVDevP, +dP/dT, and –dP/dT began to decline in treated and control animals (Figure 4.2 A, E, F), which is consistent with the negative treppe effect (i.e., force-frequency relationship) in mouse myocytes [75]. Despite the decline in these parameters after 5-10 minutes of high workload, they generally remain elevated as compared to the baseline values. In summary, the hearts from animals treated with AAV6-RR respond to β-adrenergic stimulus in the same manner observed with the TgRR hearts, where their hearts generate higher baseline force and respond to adrenergic challenge primarily with increased heart rate. This normal rate responsiveness supports the hypothesis that β-adrenergic signaling is intact, and is not impacted by AAV6-RR treatment.

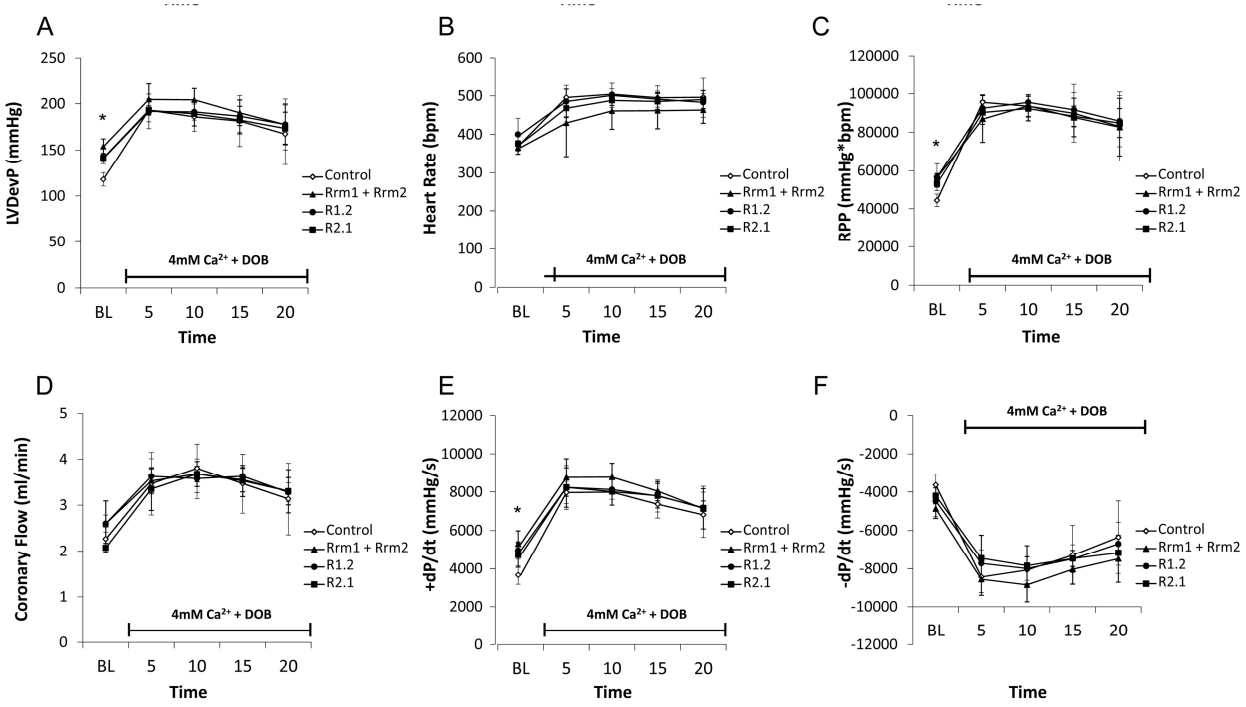

Figure 4.2. Response of LV function of animals treated with human rAAV6-RR vs. control to 20 minutes of acute physiological demand. Plots shown for animals treated with each human virus (n=4 Rrm1 + Rrm2, n=4 R1.2, n=4 R2.1) as well as controls, n=3 control. A-C) Left ventricular developed pressure (LVDevP), heart rate (HR), and rate-pressure product (RPP), the product of LVDevP and HR, measured in isolated hearts perfused at baseline (BL) and high calcium + DOB infusion. (D) Coronary flow, estimated by collecting the perfusate effluent over a 2-minute period, in Langendorff heart preparations during normal workload and high calcium + DOB infusion. (E,F) Rate of pressure change calculated by the first derivative of the LV pressure wave (dP/dt) in Langendorff heart preparations at baseline and during high calcium + DOB infusion. The positive maximum (+dP/dt) is an index of the rate of LV pressure development. The negative maximum (-dP/dt) is an index of the rate of ventricular relaxation. *p< 0.05 of all RR treated groups vs. control at BL.

While all animals treated with human rAAV6-RR virus maintained responsiveness to dobutamine and high calcium, there was no difference in maximal cardiac function under high workload between RR and control animals, which is again consistent with the data collected from the transgenic animals with constitutive overexpression of RR (Section 2.2.7) [92]. In both cases, RR overexpression increased cardiac performance under normal workload conditions and did not blunt β-adrenergic responsiveness.

Western Blot

Western Blotting was used to assess protein overexpression in the ventricle of treated and control animals. As can be seen in Figure 4.3, there is significant overexpression of RR in ventricles of all treated versus control mice (note the rat and human studies are shown on separate panels, A and B respectively). Due to a lack of homology between the rat and human sequences for R2, to our knowledge there is no commercially available antibody for rat Rrm2. Figure 4.3 A, therefore, only shows

Rrm1 overexpression in animals treated with rat Rrm1 + Rrm2. We expect that Rrm2 is overexpressed to a similar extent. This hypothesis is supported by the lane of human Rrm1 + Rrm2 in Figure 4.3 B, where there is a similar amount of overexpression of Rrm1 and Rrm2 in these ventricles. Together, these data confirm that all versions of the rAAV6-RR vector result in significant overexpression of RR versus control.

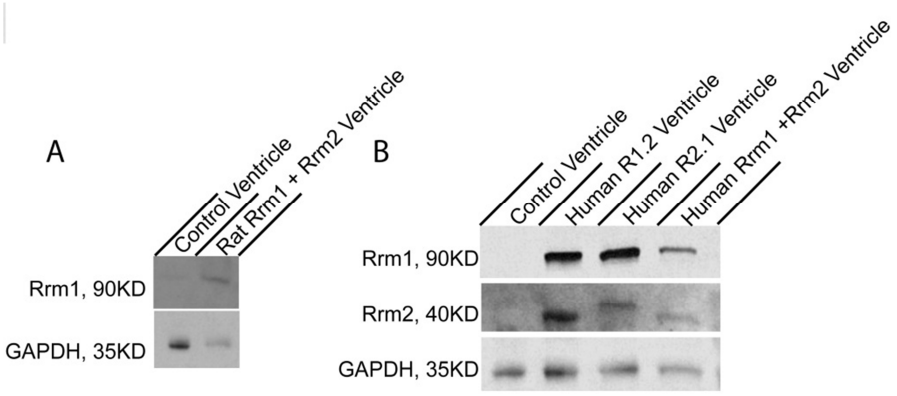

Figure 4.3. Western Blot analysis of control and rAAV6-RR treated animals. Protein was extracted from heart from control and treated mice. (A) Western blot of the rat Rrm1 + Rrm2-treated animals vs. control. Probing for Rrm1, and a loading control, GAPDH, shows that there is significant overexpression of Rrm1 in these animals. There is no Rrm2 antibody against the rat sequence so we could not assess the levels of Rrm2 in the mice treated with this vector. (B) Western blot analysis for human Rrm1 + Rrm2-, R1.2-, and R2.1-treated animals vs. control. Probing for Rrm1, Rrm2, and a loading control, GAPDH, shows that there is significant overexpression of both Rrm1 and Rrm2 in treated mice with no notable expression of RR in control heart.

Conclusions from vector development

These two studies enabled us to characterize four vector systems, both in their efficacy in inducing RR overexpression and in their effect on cardiac function in healthy mice following systemic administration. The data from these studies demonstrates that all vectors (both rat and human as well as both one-vector and two-vector systems) result in similar levels of overexpression of RR in the ventricles of treated animals vs. controls. Furthermore, the functional effects of treatment were nearly identical for all vectors tested. All vectors improved function over control by ~20-30% at baseline, and for those tested, had similar responses to dobutamine and high calcium. Furthermore, these data are also extremely similar to the data we collected from the TgRR mice discussed in Section 2.2.7.

In order to proceed toward a translational gene therapy, we sought to move forward with further characterization using a vector that contained the human Rrm1 and Rrm2 sequences, and with a one vector system. The human and R1.2 and human R2.1 both fit these criteria and both performed well. We

decided to move forward with the human R1.2 vector. For the remaining portion of this chapter, we will refer to this vector as R1.2 and refer to treated animals as RR animals.

The following sections describe additional characterization of the healthy R1.2-treated animals vs. control from the study described above as well. Subsequent sections also cover an additional study performed on infarcted animals that were either treated with R1.2 or given saline four weeks following infarction.

4.3.2 Healthy mice treated with AAV6-RR (human R1.2)

Heart size and histology in healthy mice treated with saline or human R1.2

Heart weight (HW), body weight (BW), and HW to BW ratio (HW/BW) did not differ between healthy 3-5 month old mice that were dosed with saline versus those that were dosed with R1.2 (Table 4.4). Histological assessment of cardiac tissue showed no observable pathology in mice dosed with AAV6-RR (Figure 4.4). Consistent with our previous observations of the effects of RR overexpression [92], these data demonstrate that the administration of AAV6-RR does not result in changes in cell size, cell orientation, or in hypertrophy.

Table 4.4. Heart weight and body wegiht measurements for control and RR animals. Body weight (BW), heart weight (HW), and HW/BW ratio from control and RR animals between 3-5 months of age. Data are presented as mean ± SD (Control n=7, RR n=6). No values are significantly different between groups, $p > 0.05$.

	Control	RR
BW (g)	29.8 ± 2.1	28.1 ± 2.1
HW (mg)	115.3 ± 11.2	121.0 ± 15.2
HW/BW (mg/g)	3.9 ± 0.4	4.3 ± 0.4

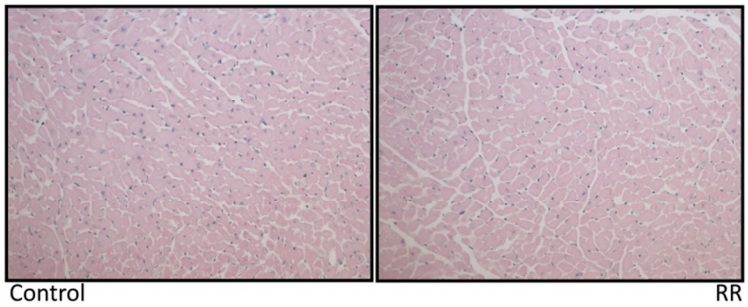

Figure 4.4. Histological assessment of control and RR heart sections. Cardiac muscle morphology in control and RR-treated mice. Tissues collected from 3-5 month old mice 4 weeks after treatment were stained with H&E. Images taken at 20x.

Vector distribution and protein expression

In order to assess the distribution of viral genomes following administration of AAV6-RR (R1.2), we performed quantitative polymerase chain reaction (qPCR) on the liver, gastrocnemius, and ventricle of healthy control and RR mice. qPCR analysis demonstrated significant viral genome (vg) uptake in the liver and ventricle of treated mice, with negligible uptake in the gastrocnemius (liver 45.0 ± 14.8

vg/nuclei; ventricle 11.2 ± 5.1 vg/nuclei; gastrocnemius 1.3 ± 1.3 vg/nuclei) (Figure 4.5). As expected, there was less than one viral genome per nuclei detected tissue from saline-injected animals. These results are consistent with previous studies using the same AAV6 and promoter combination with a different gene sequence (Dr. Erik Feest, unpublished data).

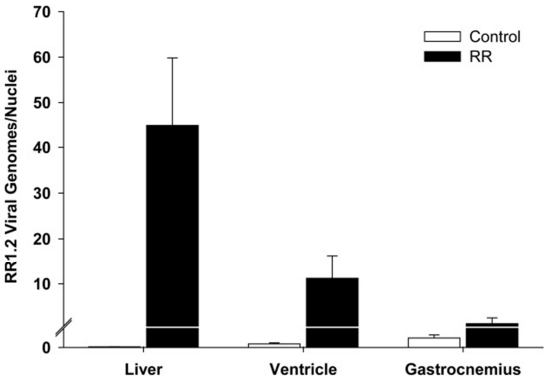

Figure 4.5. PCR Results quantifying the RR1.2 quantifying the RR1.2 viral genomes per nuclei of liver, ventricle, and gastrocnemius tissues. Bars represent the mean ± standard deviation of four RR1.2 treated samples of each tissue type and three saline-injected samples of each tissue type. Each sample was run in triplicate.

Western Blotting was used to assess protein overexpression in ventricle and liver tissue (the tissue that contained high levels viral genomes in treated animals). As can be seen in Figure 4.6, there is significant overexpression of Rrm1 and Rrm2 in ventricles of treated versus control mice (ventricle samples are the same as that shown in Figure 4.3, above). No ribonucleotide reductase protein was detectible in the liver of control or of treated animals, demonstrating the efficacy of the cardiac troponin t promoter (Figure 4.6).

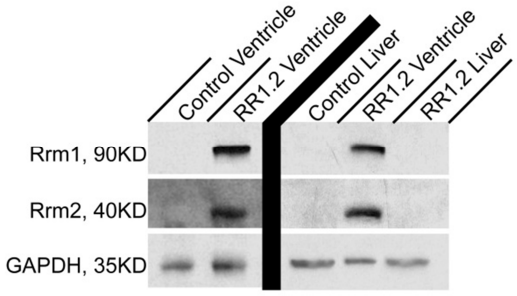

Figure 4.6. Western blot analysis of control and RR mouse heart and liver tissue. Protein was extracted from heart and liver from control and treated mice. Western blot analysis for Rrm1, Rrm2, and a loading control, GAPDH, shows that there is significant overexpression of both Rrm1 and Rrm2 in treated mice with no notable expression of RR in control heart or liver.

Histological assessment of the tissues stained for Rrm1 shows significant overexpression of Rrm1 in mice treated with rAAV6-RR (R1.2) vs. control, which can be seen from the representative images of stained sections (Figure 4.7). These data also demonstrate the extent and distribution of protein overexpression in the hearts of treated animals. The Rrm1 protein is evenly distributed throughout the entire section in each of the sections observed

.

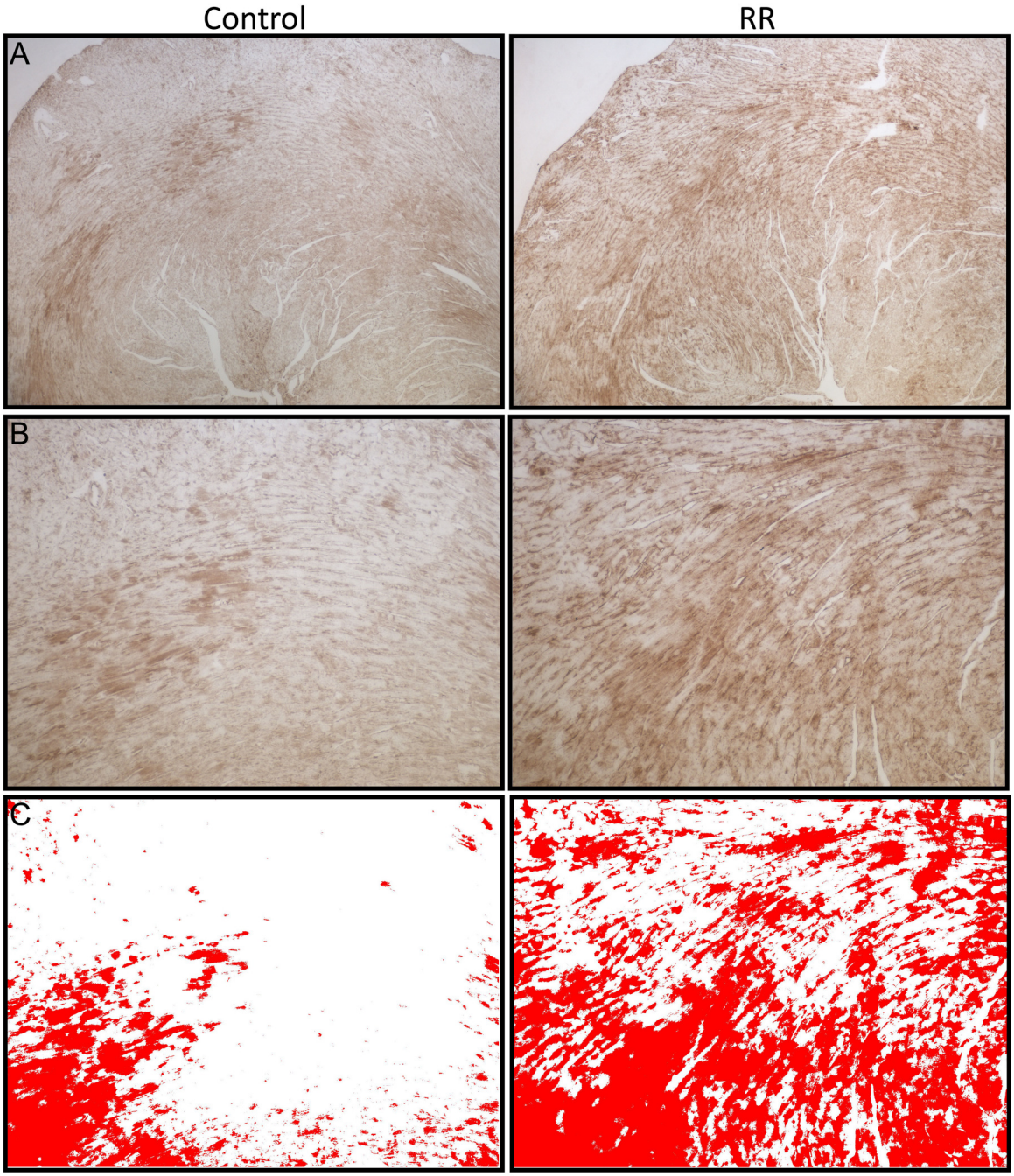

Figure 4.7. Histological assessment of control and RR animals to assess extent and distribution of RR overexpression. Representative cardiac sections from 3-5 month old mice, 4 weeks after treatment were stained with anti-Rrm1. (A) Anti- Rrm1 stained section taken at 4x, control section on the left and RR-treated on the right. (B) Anti- Rrm1 stained section taken at 10x, control section on the left and RR-treated on the right. (C) 10x Image thresholded to show positive Rrm1 staining, control section on the left and RR-treated on the right.

Together, these data demonstrate that systemic administration of rAAV6-RR results in cardiac-specific overexpression of RR. Importantly, even though there are viral genomes found in the liver at high levels, there was no detectable RR protein expression in the livers of treated animals (Figure 4.6). Furthermore, liver weight did not differ between treated animals and controls (RR, 1.1g vs. Saline, 1.1g) and there was no outward sign of disease as a result of viral genome presence. These results validate the vector system and demonstrate that systemic administration of rAAV6-RR can be used as a tool to achieve RR overexpression in the heart.

Langendorff isolated heart preparations

Langendorff isolated heart preparations were used to assess *ex vivo* cardiac function in 3-5 month old healthy mice under basal and high workload conditions. These data are discussed in detail in section 4.3.1 and values for each parameter described can be found in Table 4.3, however an additional figure showing only R1.2-treated versus control is included below (Figure 4.8) to clearly show the difference between control and AAV6-RR (R1.2)-treated mice. Briefly, mice dosed with rAAV6-RR (R1.2) had significantly enhanced basal cardiac function (LVDevP) compared to control mice dosed with saline with unchanged heart rate. The rate pressure product, and rate of contractility, +dP/dt were also significantly elevated in RR mice versus control. The rate of ventricular relaxation was unchanged.

Figure 4.8 highlights that LVDevP, HR, RPP, cardiac output, +dP/dT, and –dP/dT were significantly increased in both control and RR hearts following dobutamine and high calcium infusion, demonstrating the expected response to β-adrenergic stimulus. As noted above, both groups experienced a decline in LVDevP, +dP/dT, and –dP/dT after ~5 minutes with HR ~500 bpm (Figure 4.8 A, E, F), which is consistent with the negative treppe effect previously observed in mouse myocytes [75]. Despite the decline in these parameters after 5 minutes of high workload, they generally remain elevated as compared to the baseline values. This normal rate responsiveness supports the hypothesis that β-adrenergic signaling is intact, and is not impacted by AAV6-RR treatment. R1.2 mice do not have elevated maximal function relative to control mice (215.6 ± 18.9 mmHg RR vs. 243.3 ± 20.2 mmHg), which is consistent with previous observations. The improved cardiac performance observed in healthy animals dosed with AAV-RR motivated us to investigate whether treatment with AAV-RR could improve contractility in mice suffering from chronic heart failure.

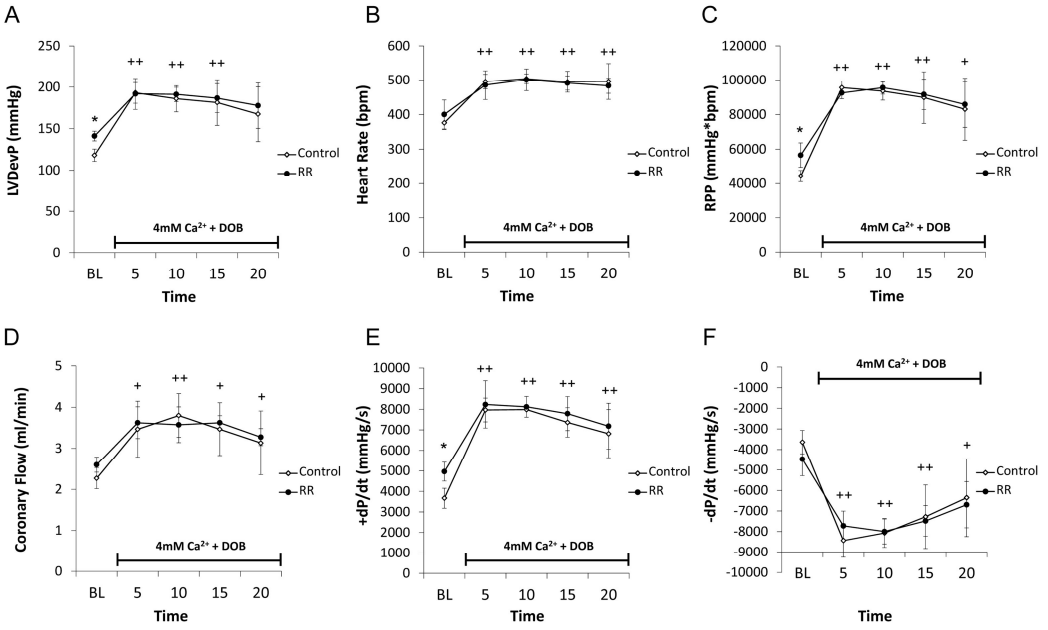

Figure 4.8. Response of LV function to 20 minutes of acute physiological demand. (A-C) Left ventricular developed pressure (LVDevP), heart rate (HR), and rate-pressure product (RPP), the product of LVDevP and HR, measured in isolated hearts perfused at baseline (BL) and high calcium + DOB infusion. n=4 RR and n=3 control. (D) Coronary flow, estimated by collecting the perfusate effluent over a 2-minute period, in Langendorff heart preparations during normal workload and high calcium + DOB infusion. n=4 RR and n=3 control. (E,F) Rate of pressure change calculated by the first derivative of the LV pressure wave (dP/dt) in Langendorff heart preparations at baseline and during high calcium + DOB infusion. The positive maximum (+dP/dt) is an index of the rate of LV pressure development. The negative maximum (-dP/dt) is an index of the rate of ventricular relaxation. *$p< 0.05$ vs. control at BL, $^{+}p<0.05$ vs. its group baseline value (++ indicates both groups are elevated versus baseline, + indicates only RR group is elevated), n=4 RR and n=3 control.

4.3.3 Infarcted mice treated with AAV6-RR (human R1.2)

Echocardiography of infarcted mice

Mice undergoing infarctions were echoed at baseline (pre-infarct), 4 weeks post-infarction, 8 weeks post-infarction, and 12 weeks post-infarction to assess *in vivo* cardiac function. Treatment was administered after the 4 week post-infarction echo. Inclusion criteria are outlined in the methods section above (Section 4.2.7). At baseline, there was no significant difference in any parameter between the control and RR animals. At the 4 week post-infarction (pre-treatment) time point, there was still no difference between the RR and control groups, but both groups had significantly depressed fractional shortening versus baseline. All other parameters were, on average, unchanged from baseline (Table 4.5.)

Outlier analysis was performed using Tukey's hinges as the first and third quartile (Q1 and Q3, respectively). Outliers were identified as any value that was less than Q1 – 1.5x(Q3-Q1) or any value that was more than Q3 + 1.5x(Q3-Q1). This analysis returned one animal from the RR group that was an outlier in the post-treatment Fractional Shortening measurement. As such, this animal was removed from all calculations. This exclusion combined with the echo inclusion criteria for large infarcts left us with group sizes of n=7 (saline) and n=5 (RR).

Table 4.5. Echocardiography measurements. Echocardiographic measures obtained in saline-injected and AAV6-treated mice. LVID;d: LV internal dimension in diastole, LVID;s: LV internal dimension in systole, FS: fractional shortening, HR: heart rate. Data are presented as mean ± SD (Saline n=7, AAV6-RR n=5). *p < 0.05 vs. baseline measurement from the same group.

	PRE-TREATMENT				POST-TREATMENT			
	Baseline		4 weeks post-infarct		8 weeks post-infarct		12 weeks post-infarct	
	Control	RR	Control	RR	Control	RR	Control	RR
LVID;d (mm)	4.1 ± 0.2	3.8 ± 0.4	4.1 ± 0.6	4.2 ± 0.5	4.3 ± 0.7	4.5 ± 0.5	4.3 ± 0.6	4.5 ± 0.5
LVID;s (mm)	2.7 ± 0.2	2.7 ± 0.1	3.1 ± 0.4	3.2 ± 0.5	3.2 ± 0.8	3.3 ± 0.6	3.2 ± 0.7	3.3 ± 0.5
FS (%)	33.5 ± 2.0	31.2 ± 2.8	26.0 ± 3.2*	23.4 ± 2.9*	26.8 ± 6.8	27.5 ± 4.8	27.2 ± 5.3	26.7 ± 3.8
HR (bpm)	470 ± 47	435 ± 26	462 ± 28	467 ± 41	449 ± 17	455 ± 30	451 ± 35	453 ± 16

At every time point following treatment, the two groups did not differ on any parameter when compared to each other (student's t-test comparing mean from RR vs. mean from control). If, however, a repeated measures, paired t-test was used to compare whether an animal improved following treatment (comparing the change fractional shortening from pre-treatment (4 weeks post-infarct) to post-treatment (8 weeks or 12 weeks post-infarct)), the animals treated with AAV6-RR significantly improved at 8 weeks (4 weeks after treatment) while the control animals did not change (RR p=0.04 vs. control p=0.4, Table 4.6). At 12 weeks post-infarct (8 weeks after treatment), the fractional shortening in the RR group fell slightly. Thus, the paired t-test comparing pre-treatment to 8 weeks post-treatment is not significant for either treated or control animals (RR p=0.09 vs. control p=0.6).

Table 4.6. Repeated measures t-test analysis of fractional shortening data obtained from echocardiography analysis. Paired t-test results on fractional shortening values obtained from echocardiographic analysis. FS: fractional shortening. Data are presented as mean difference of the 4 week post-infarct echo data (pre-treatment) vs. the 8 or 12 week post-infarct echo data (post-treatment) ± SD (Saline n=7, AAV6-RR n=6). *p = 0.05 for treated animals comparing the mean difference between pre-treatment and post-treatment.

	4 weeks post-infarct vs. 8 weeks post-infarct		4 weeks post-infarct vs. 12 weeks post-infarct	
	Control	AAV6-RR	Control	AAV6-RR
Mean Difference in % FS (value)	0.8 ± 6.3	5.3 ± 3.8	1.6 ± 5.6	3.5 ± 3.5
p-value (two-tailed, paired t-test)	0.74	0.04*	0.48	0.09

This analysis demonstrates that there is large inter-animal variability, and thus comparing the means of each group directly to each other does not reveal any between group differences. When each animal is used as its own control in the repeated measures t-test, however, the difference from treatment becomes clear. To further assess the effect of treatment, we evaluated the mean percent change in fractional shortening function at 8 weeks and 12 weeks post-treatment for each group. While these data are not significant, they demonstrate that there was greater improvement observed in the treatment group than the controls (4 week post-infarct (pre-treatment) vs. 8 week post-infarct (post-treatment): Saline = 3%, RR = 24%; 4 week post-infarct vs. 12 week post-infarct: Saline = 7%, RR = 16%)(Figure 4.9).

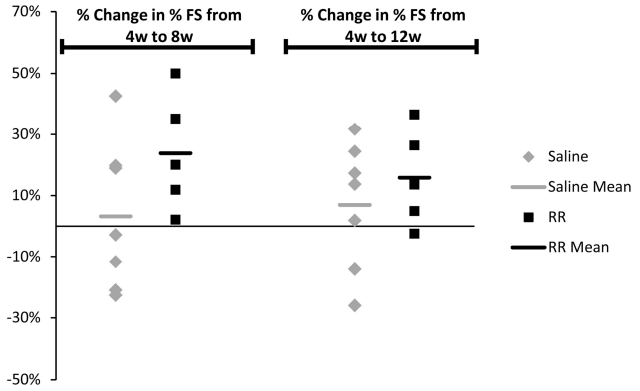

Figure 4.9. Percent change in fractional shortening from pre-treatment (4 weeks post-infarct) to post-treatment (8 weeks and 12 weeks post-infarct). Each marker represents one animal (Saline n=7, RR n=5). Horizontal lines represent group means, which are reported in the text above. The mean difference is not significant between groups, which is a reflection of the high variability within each group.

This representation of the data highlights that only one of the RR treated animals regressed below the pre-treatment value over the following eight weeks, while ~60% control animals did not improve at four weeks post-treatment and ~30% remain worse than pre-treatment levels at eight weeks post-treatment. The large spread of these data also highlights the variability within each group. Some variability is likely due to inherent differences between animals. Some, however, is probably due to variation in the size of the infarction each animal received (discussed in more detail below).

Together, these data demonstrate that, when using each animal as its own internal control, rAAV6-RR treatment results in significantly improved function following infarction. However, the large variability within each group dramatically affects the statistical analysis when the group numbers are as low as they are (n=7 control, n=5 RR), and thus there were no significant functional differences when comparing means between groups.

Cardiac magnetic resonance imaging (MRI) of infarcted mice

Cardiac MRI was performed at the 12 week post-infarct time point. We sought to obtain high-resolution, volumetric measurement of cardiac function that is not possible with echocardiography. MRI was also used to quantify regional wall thickening differences – both as a measure of infarct size (% dysfunction) and the effect of treatment (improvements in systolic thickening in remote regions of the heart). Assessment of infarct size is important to get a sense of the extent of heterogeneity of our data set. Infarct size was defined as the % of left ventricular mass (LV Mass) that had fractional wall thickening below zero. Fractional wall thickening was determined for 12 segments on each short axis slice (1 mm thick) throughout the heart and was calculated using the following formula: $(ES_{WT} – ED_{WT})/ED_{WT}$ where ES_{WT} is equal to the wall thickness at end systole and ED_{WT} is defined as the wall thickness at end diastole.

Similar to the echocardiography data presented in Section 4.3.3, there were no significant differences in any parameter between groups (ejection fraction, EF; stroke volume, SV; Left Ventricular Mass, LV Mass; and % dysfunction, % of LV Mass that has fractional wall thickening < 0%). Because the MRI was only acquired at one time point we cannot perform repeated measures analysis on these data. Thus, despite the high resolution of this imaging technique, the inter-animal variability prevents any conclusions from being drawn from comparing between groups.

Table 4.7. Cardiac MRI measurements obtained in control and rAAV6-RR-treated mice. EF: ejection fraction, SV: stroke volume, LVM: left ventricular mass, % dysfunction calculated as percentage of left ventricle with < 0% fractional wall thickening. All data were analyzed by two readers. Data are presented as mean ± SD (Control n=7, RR n=5).

	12 weeks post-MI	
	Control	RR
EF (%)	52.8 ± 23.6	50.5 ± 11.1
SV (μl)	29.1 ± 3.4	28.1 ± 3.8
LVM (mg)	120.9 ± 34.5	117.5 ± 17.3
% dysfunction	16.7 ± 14.0	16.0 ± 2.8

Infarct size measurements ranged from 1% to 41.9% in the control group and from 10.2% to 25.1% in the RR group, indicating the wide range of infarct sizes that could underlie the large

variability in functional measurements. The infarct size measurements are relatively well correlated with the fractional shortening data (echo) and ejection fraction measurements (MRI) for the control group (the RR group is more clustered around medium sized infarcts, and there is no correlation between function and % dysfunction). The r-squared value for the infarct size vs. fractional shortening measurements from the 12 week post-MI (8 weeks post-treatment) are 0.73 (control) and 0.005 (RR). R-squared values for infarct size vs. ejection fraction measurements from the same time point are 0.93 (control) and 0.11 (RR). A further analysis of variability as a result of the infract surgery (especially in the control group), quantification of the range of % FS within each group at multiple time points, shows that in the control group the range of function increases over time. At baseline, the range of % FS values is 3.6 for control and 6.8 in RR group. Four weeks after the infarct surgery, before treatment the range increased in the control group to 8.8 and stayed approximately the same in treated animals, at 6.9. At the final time point, 12 weeks post-infarct surgery, 8 weeks post-treatment, the range of function in the control group increased further to 13.7 and again the range in the RR group stayed about the same, 6.1. Together, these analyses indicate that if infarct size were more consistent within the control group, it is likely we would obtain imaging data with less variability in cardiac function, which would enable a more robust analysis of the effect of treatment. Adding more animals to this study would also improve the statistical analysis. With the numbers currently used one animal can have a profound effect on the group statistics.

4.4 Discussion

There were two primary goals of this study. First, we sought to characterize a recombinant adeno-associated vector carrying a cTnT promoter and the human sequence of RR by evaluating both its distribution and resulting protein overexpression in healthy mice as well as its effects on cardiac function in healthy mice. Second, we aimed to determine whether treatment with AAV6-RR in a chronic mouse infarction model would result in significant improvements in cardiac function versus controls. The data presented here demonstrate that treatment with AAV6-RR results in significant levels of viral genomes in the liver and hearts of treated animals, however overexpression of RR is limited to the heart, which is expected with a cTnT promoter. The overexpression of RR in the heart resulted in significant improvements in cardiac function *ex vivo* as determined by the Langendorff perfused heart experiments. Importantly, this improvement in cardiac function occurred without any impact on heart rate, and did not interfere with β-adrenergic rate-responsiveness. Even though there was significant improvement in *ex vivo* function in these animals, echo analysis of cardiac *in vivo* did not reveal any

between-group differences. There are many reasons that could explain this discrepancy (increase in *ex vivo* function with no change in *in vivo* function) ranging from flaws in our hypothesis to problems with the image analysis we performed. Below, Table 4.8 breaks down these potential issues. The right column of the table contains a discussion of why particular issues are more likely to be the root cause of the discrepancy. There was also significant improvement in cardiac function observed in animals treated with rAAV6-RR following a myocardial infarction versus control if a repeated measures (within-animal) statistical test was used. However, we observed a large amount of inter-animal variability in function and infarct size within the groups, which precluded us from making conclusions about the treatment by comparing the treated group directly to the control group of animals. Some of the issues discussed in Table 4.8 could also be contributing to the variability and low signal/noise that we observed in our assessment of *in vivo* cardiac function.

It is also important to note that TgRR animals had significantly improved cardiac function *in vivo* vs. control animals, which was not seen in this study. There are a number of reasons that could explain this difference. First, the TgRR and WT mice used in that study were on an FVB background. The mice used in this study were on a C57Bl/6 background. There are known differences between strains that impact cardiac function, regulation of HR and autonomic nervous system activity, response to stress, and response to genetic manipulation [95–98]. These strain differences are important to keep in mind as they may affect (1) how the animals respond to anesthesia and the acquisition of echocardiography data directly, and/or (2) how the animals respond to RR overexpression. Additionally, because overexpression of RR in the transgenic mice was achieved via the chicken β-actin promoter and cytomegalovirus enhancer and was present since birth, the RR overexpression in the C57Bl/6 adult mice was achieved via AAV6-meditated transduction driven by the cTnT promoter and enhancer, we may observe different levels of RR overexpression and thus different effects on cardiac function. Lastly, it is possible that the discrepancy is due to echocardiography acquisition and analysis itself. Different experimenters collected and analyzed the echocardiography data from the TgRR study and from the C57bl/6 study, which could also explain the differences observed. An experiment to test these hypothesis could be performed by treating healthy, control FVB mice with the AAV6-RR virus and measuring cardiac performance *in vivo.* This would elucidate whether the issue was due to strain differences or if the discrepancy was related to the method of RR overexpression. If this experiment was performed with the same operator who collected and analyzed the C57Bl/6 study, it could also rule out inter-operator differences.

The results from this study confirm that systemic delivery of AAV6-RR is a feasible approach to achieve cardiac-specific overexpression of RR. Furthermore, the results here indicate that overexpression of RR may have therapeutic potential to improve cardiac function in patients who suffer from systolic dysfunction. These data support the previous work studying RR overexpression or increased dATP concentration in various models.

Table 4.8. Disscussion of potential issues with echocardiography in mice that could explain discrepancy between *in vivo* and *ex vivo* functional measurements. Table below discusses potential issues with echo imaging in mice as well as tests that have been done and information that we have that inform us on the likelihood of these issues underlying the effect that we see. Works cited in this table are [144, 157].

Potential Explanation for discrepancy	Discussion of tests that have been performed to address potential issues
dATP does not affect heart function *in vivo*	While this has not been directly addressed, previous work performed in our lab (Lundy, 2014; unpublished work) have shown that RR overexpression improves cardiac function *in vivo*. As such, I expect that the hypothesis that elevation in dATP increases cardiac function is still valid. It is important to note, however, that strain differences (discussed in Section 4.4) and species differences may play a role in whether this effect is detectable *in vivo.*
rAAV system doesn not result in sufficient elevation in [dATP] to improve function	We have not yet quantified whole cell [dATP] in rAVV6-RR -treated vs. untreated animals. We have, however, quantified dATP in cells following AV-RR transduction *in vivo* and Ylikallio et al. quantified [dATP] in skeletal muscle of TgRR animals. In both of these cases, dATP was increased 10x in RR animals vs. controls, which, in both cases, increased cardiac function by ~20%. [dATP] should be quantified in rAAV6-RR-treated animals to confirm similar elevation to previous studies. If [dATP] is too low in these animals, we could consider increasing the viral dose for subsequent studies in an attempt to increase the dATP concentration further.
Function is already maximal in healthy mice *in vivo*, so there is no room for function to be further improved	We tested this hypothesis by evaluating mice under deeper anesthesia, with dobutamine, and following infarction. Under deeper anesthesia (lower heart rate), we still did not see any differences between groups. Furthermore, treatment with dobutamine increased heart rate and fractional shortening, indicating that the hearts were not maximally activated at rest. The data from our infarction study (below) show promising preliminary results, however there is large inter-animal variability which obscures the effect. Future studies could be performed on other models of systolic dysfunction that have a more homogenous phenotype compared to infarcted animals (dystrophic or DCM transgenic mice for example), which would enable us to test this effect without sacrificing homogeneity.
There is hormonal regulation/compensation *in vivo* obscuring any effect	This could potentially explain the discrepancy between *ex vivo* and *in vivo* measurements of cardiac function. *Ex vivo* measurements enable the assessment of contractility independent of autonomic nervous system regulation, which cannot be tightly controlled *in vivo.* It is possible that neuronormal regulation (1) accounts for some of the variability observed *in vivo* (within a given strain after infarction as well as between strains) and/or (2) blunts the effect of elevated [dATP] *in vivo* in C57bl/6 mice. More rigourous testing of the effects of parasympathetic and sympathetic blockers and agonists would need to be conducted to confirm this hypothesis.
The effect of elevated [dATP] on cardiac function is not large enough to resolve with echo	We have performed a couple of tests to assess the variability and underlying noise in echocardiography of mouse hearts. As the literature suggests, we observed relatively high day-to-day variation in mice. Some ways to control this are: closely monitor anesthesia, perform any shaving of the mice 24 hours before echo, perform echo in the same room under the same conditions. Clinically, it has been reported that there is inter- and intra-observer variability in % EF calculation of over 10% (Galderisi, 2011). This may have implications regarding whether the effect of increased [dATP] can be detected by this imaging modality. This does not take into effect the error involved in extrapolating whole heart function from m-mode measurements, which would be increased in animals with irregular heart shapes and contracile performance as is the case following MI. This error may also be compounded with a heterogenous
Echo in itself has a lot of error (especially with mice)	
Group sizes are too small and this study is underpowered for a technique with such variability	Given the inherent error in echo imaging, and the heterogeneity within our groups, it is likely that to see an effect, we need much larger group sizes than what we currently have used. At this point, single animals have large effects on group means and deviation, which strongly impacts the statistical analysis. Future studies will be carried out with similar experimental design to supplement the animals numbers included in these studies presented here.

4.5 Future directions

Even though this study demonstrated that there was an effect of treatment with rAAV6-RR on infarcted animals, the inter-animal variability was high, and ultimately the study was underpowered. To increase power future studies should be carried out with the same experimental design to increase the number of animals that can be compared between treatment and control. To reduce inter-animal variability within this system, emphasis should be placed on achieving more consistent infarction size during surgery and on acquiring consistent echo data. Echo imaging on small animals has been demonstrated to be riddled with low signal to noise and low reproducibility [REF]. It is possible to overcome this hurdle by increasing the sample size, however more work could be done on the operator side by ensuring that echo analysis and acquisition are consistent day-to-day. For example, a small study could be run on healthy mice where they were echoed three days for 2 weeks to determine how much variability there is with each day of acquisition and analysis.

An alternative approach would be to consider investigating a different model of systolic dysfunction. One such example could be animal models of dilated cardiomyopathy, such as the tropomyosin (Tm) D230N transgenic mouse developed by the Tardiff group at the University of Arizona [99]. The Tm D230N mutation is clinically observed [100]. The D230N transgenic mice have reduced calcium sensitivity compared to WT mice, which results in systolic dysfunction [99–101]. We have previously shown that dATP increases the calcium sensitivity of myofilaments *in vitro*, so this model of systolic dysfunction may not only provide a more consistent phenotype (as compared to an infarct model), but may offer interesting insights into the range of applicability of treatment with AAV-RR. Although transitioning to different model of systolic dysfunction may pivot this research away from the primary translational end point (human heart failure), this is a potential alternative investigative approach that would demonstrate efficacy of the therapy in small animals.

CHAPTER 5. MOLECULAR MECHANISMS UNDERLYING DEOXY ADP ACTIVATION OF MYOSIN

5.1 Introduction

Myosin is a motor protein that normally uses the energy of ATP hydrolysis to produce force and motion. However, myosin is a promiscuous enzyme that can use a variety of nucleotides as substrates, although most are not as effective as ATP [20, 22]. 2 deoxy-ATP (dATP), a nucleotide identical to ATP with the exception of an oxygen missing from the 2-position on the ribose ring, is normally produced in cells for DNA synthesis and repair. We demonstrated previously that dATP increases hydrolytic activity of both cardiac (MYH6, MYH7) [49] and skeletal (MYH2) myosin [13]. dATP also increases the magnitude and rate of contraction of both cardiac [24, 49] and skeletal muscle cells [11, 12], as well as left ventricular pressure development in mice [92]. Chemo-mechanical analysis of acto-myosin suggests that, following myosin (M) hydrolysis of the γ-phosphate of dATP, M.dADP.Pi binding to actin is enhanced, and product (Pi, dADP) release may be faster than for M.ADP.Pi [12]. While these biochemical and mechanical data are convincing that post-hydrolytic myosin activity is enhanced by dATP, the structural basis for this improved performance is not known. Because myosin translates the chemical energy of ATP or dATP to mechanical force through conformational changes associated with alterations to the binding pocket and actin binding surface, it might be expected that the dATP-induced enhancement of myosin performance is the direct result of changes to protein structure and dynamics.

Myosin is composed of functional subdomains that undergo conformational changes in a nucleotide-dependent manner, including the N-terminal, upper 50k, lower 50k, and the converter subdomains (Figure 1.9). The cleft that separates the upper and lower 50k domains is bordered by the strut and loop 2 that connect the upper and lower 50k domains near the actin binding surface and three nucleotide binding regions (p-loop, switch 1, and switch 2) at the apex of the cleft. [55, 102]. To better understand how dATP alters myosin performance, we are particularly interested in the conformation, contacts, and dynamics of the regions of myosin that are involved in translating alterations from the nucleotide binding pocket to the actin binding surface. Because the chemo-mechanical assessment of how dATP altered cross-bridge cycling suggested that post-hydrolytic myosin binding to actin is enhanced with dATP, in this study we have focused our assessment on the pre-powerstroke conformation of myosin where myosin is bound to the nucleotide hydrolysis products, (d)ADP and Pi. We hypothesized that dADP.Pi-induced alterations to the binding pocket ultimately result in the stabilization of a myosin

structure that has a higher propensity for binding actin than that bound to ADP.Pi. Thus, here we provide a detailed exploration of the P-loop and switch regions, the cleft conformation, and the actin binding surface structure and charge.

This work is focused on determining the structural detail underlying the biochemical observation of dADP-induced increased cross-bridge attachment. We used an *in silico* approach to assess atom-level differences in pre-powerstroke (weak-binding) myosin structure and dynamics as a result of dADP.Pi (vs. ADP.Pi) binding. Multiple, all-atom molecular dynamics (MD) simulations were performed of the Dictyostelium discoideum myosin S1 head, which was crystallized in the pre-powerstroke state (PDB ID:1VOM; [103]) with Mg^{2+},P_i and either ADP or dADP in the binding pocket for 50 ns (referred to as ADP simulations and dADP simulations, respectively, throughout). These simulations provide a better understanding of the structure-function relationship of myosin in the pre-powerstroke state and how changes in its conformation could directly alter cross-bridge attachment. Furthermore, the atom-level assessment of myosin structure, simulated over time, provides unique detail into the dynamics of allosteric regulation that propagates a conformational change from the nucleotide binding pocket to the actin binding surface of myosin. The allosteric mechanism was previously studied primarily through assessment of crystal structures alone. We demonstrate how, with all else equal, dADP binding to myosin in the pre-powerstroke conformation induces conformational changes within the myosin S1 head that result in an overall shift in the population distribution of energetically favored myosin structures to a conformation that favors actin binding. These changes are precipitated by a change in the contacts made by Phe129, which spends the majority of its time in contact with the O2' at the 2 position of the ribose ring of ADP; Phe129 reorients and makes altered contacts, however, when the O2' is absent. The significant conformational alterations in the nucleotide binding pocket result in an altered contact network and stabilize a myosin conformation that is more conducive to actin binding. The MD simulations predict that myosin bound to dADP should enhance electrostatic interactions between myosin and actin, and actin binding studies in an *in vitro* motility assay support the MD predictions. These data not only suggest a mechanism for dADP-induced changes to the myosin structure and dynamics that favor myosin binding to actin, but also provide unique insight into the dynamics of pre-powerstroke myosin bound to ADP.

5.2 Materials and Methods

The sequence and residue numbering for Dictyostelium discoideum myosin II are used throughout this chapter.

5.2.1 Model Selection

The crystal structure for pre-powerstroke myosin (PDB ID:1VOM), which was resolved at 1.90 Å was used as a starting structure for all simulations [103]. VO_4 was replaced in all structures by PO_4 (Pi). PO4, ADP, and dADP were parameterized in the Levitt et al. force field [104] using previously established bond length, bond angles, and torsion angles. Partial charges (Figure 5.1) were calculated by running a geometry optimization of each structure in GAMESS [105]. Loops missing from the 1VOM structure were replaced using homology modeling in MODELLER [106–109]. Dictyostelium discoideum myosin was chosen for these studies because it is the myosin II that has been crystalized in multiple conformations at the highest resolution. We sought a myosin that was available in multiple conformations so that we can further study the effects of dATP and its hydrolysis products on other parts of the cross-bridge cycle. We sought myosin that had been crystalized at high resolution because those are most suitable for the all-atom MD simulations performed.

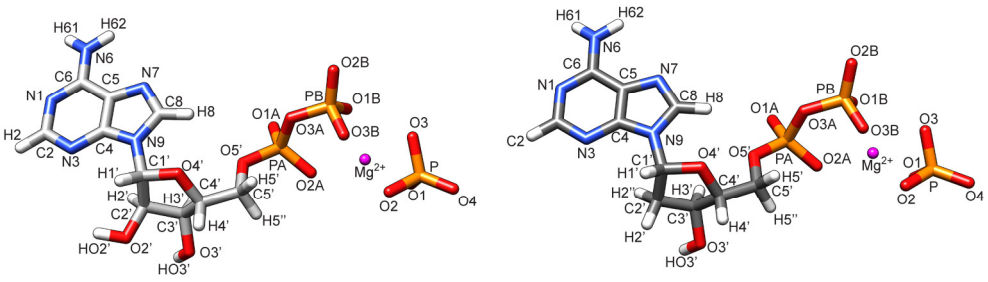

		ADP	dADP
ATOM NAME	ATOM TYPE	CHARGE	CHARGE
N6	M2	-0.34288	-0.344454
H61	HN	0.236548	0.236169
H62	HN	0.237021	0.236169
C6	A6	0.253825	0.251973
N1	L6	-0.34191	-0.344999
C2	A6	0.126475	0.123278
H2	H	0.10685	0.104116
N3	L6	-0.31015	-0.309591
C4	A7	0.160039	0.157614
C5	A7	-0.13184	-0.133299
N7	L5	-0.21576	-0.210639
C8	A5	0.1112	0.108944
H8	H	0.141841	0.235761
N9	N	-0.2661	-0.273488
C1'	C1	0.214412	0.244526
H1'	H	0.103047	0.140089
C2'	C1	0.043638	-0.219276
H2'	H	0.115655	0.118085
H2''	H	N/A	0.09803
O2'	OH	-0.402531	N/A
HO2'	HO	0.267589	N/A
C3'	C1	0.053628	0.07953
H3'	H	0.110467	0.106861
O3'	OH	-0.40618	-0.403803
HO3;	HO	0.256051	0.257763
C4'	C1	0.053637	0.058522
H4'	H	0.083319	0.082485
O4'	OR	-0.35409	-0.355572
C5'	C2	0.039441	0.038081
H5'	H	0.095021	0.09257
H5''	H	0.080746	0.078681
O5'	O2	-0.400608	-0.399573
P1	P	0.515711	0.5156
O1A	OP	-0.586497	-0.587111
O2A	OP	-0.58211	-0.584365
O3A	O2	-0.45844	-0.459947
PB	P	0.402435	0.403197
O1B	OP	-0.667782	-0.670703
O2B	OP	-0.668301	-0.667509
O3B	OP	-0.672896	-0.672845
P	P	0.313193	0.313193
O1	OP	-0.825042	-0.825042
O2	OP	-0.826143	-0.826143
O3	OP	-0.830034	-0.830034
O4'	OP	-0.831975	-0.831975

Figure 5.1. Partial charges used as parameters for ligands in MD simulations. Cartoons of ADP, dADP, Pi, and Mg^{2+} are shown with labels that correlate to the rows in the table below. All other parameters (bond length, bond angle, and torsion angle) were used from Levitt et al., 1995 expect for the angle of PA-O3-PB bond [104]. Based on visual inspection of the static molecule, a value of 130^{o} was used for this bond angle.

5.2.2 MD Simulations

Both systems were prepared according to our standard protocols [110]. All-atom, explicit solvent MD simulations were performed at 37°C and neutral pH using *in lucem* molecular mechanics (*il*mm) (Beck et al., 2000-2014). The NVE microcanonical ensemble (constant number of particles, volume, and energy) was used with periodic boundary conditions, and the Levitt et al. force field [104]. Before running the simulations, the starting structures (Myosin + (d)ADP + P_i + Mg^{2+}) were minimized for 1,000 steps, and flexible three-center (F3C) water molecules [112] were added to a rectangular box The solvent density of the box was adjusted to 0.99336 g/ml, the experimentally determined density for that temperature [113]. A time step of 2 femtoseconds (fs) was used, and after each picosecond (ps), a structure was saved for analysis. An 8 Å force-shifted cutoff was employed for non-bonded interactions [114]. Three simulations of Myosin + ADP + P_i + Mg^{2+} and three simulations of Myosin + dADP + P_i + Mg^{2+} were performed for 50 ns each.

5.2.3 MD Analysis

All analyses of MD trajectories were performed using *il*mm unless otherwise indicated (Beck et al., 2000-2014). Contacts between non-sequential atoms were classified as in contact if two carbon atoms were separated by less than 5.4 Å, or if two non-carbon atoms were separated by less than 4.6 Å. They were further classified as hydrophobic if they were between two carbon atoms less than 5.4 Å apart and each carbon was bound to at least one hydrogen atom. Contacts were considered hydrogen bonded if there was a donor (D-H) and acceptor (A) atom that were within 2.6 Å of each other and where the D-H-A angle was between 45° and 135°. Lastly, contacts were defined as 'other' if there were two heavy atoms within 4.6 Å of each other and did not fit in either of the other two classifications. Distances were measured between specific atom pairs. Solvent accessible surface area (SASA) was calculated using the Lee and Richards algorithm [115]. Protein images were generated using the UCSF Chimera package from the Computer Graphics Laboratory, University of California, San Francisco (supported by NIH P41 RR-01081) [116] unless otherwise indicated.

5.2.4 In vitro motility

In vitro motility assays were performed as previously described [117, 118]. Briefly, skeletal muscle myosin used in this assay was prepared from back muscle of male New Zealand White rabbits according to Margossian and Lowey [119]. It was stored at –20 °C in 50% glycerol for no longer than 4 months. Heavy meromyosin (HMM) was prepared as described by Kron et al. [120] and used within one week of

preparation. F-actin was prepared from rabbit back and leg muscle ether powder, labeled with Rhodamine-phalloidin (RhPh; Molecular Probes, Eugene, OR), and stored on ice for no longer than six weeks [120–123].

Flow cells were constructed as described previously [124, 125]. Two glass cover slips were used and separated by 2mm foam adhesive strips. Total chamber volume was typically 50–70 µl. The lower slide surface was coated with 0.1% nitrocellulose in amylacetate (Sigma-Aldritch, St. Louis, MO). The experimental procedure followed was similar to Gordon et al. [118, 125]. Briefly, HMM (0.17- 0.4 mg/ml) was added to the flow cell for 3 min, and nonspecific protein binding to the surface was blocked with bovine serum albumin (BSA). Non-labeled sheared F-actin was then added to the chamber for 1 min followed by wash, after which RhPh F-actin was then added for 1 min followed by infusion of the motility buffer. The motility buffer consisted of (in mM/L): 25 imidazole, 1 EGTA, 0.85 free Mg2+, 0.1 MgATP /MgdATP, and ionic strength was adjusted to 50-150 mM with KCl. Antioxidants (18 µg/ml catalase, 0.1 mg/ml glucose oxidase, 3 mg/ml d-glucose, and 40 mm DTT) were added to minimize photobleaching [120]. All motility assays were performed at 23.5 ± 0.5 °C. At least six areas of each assay chamber were recorded for 10 seconds each at 10 Hz with IVM Image Acquisition. Recordings were analyzed digitally, using custom software developed in house.

5.3 Results and Discussion

Three simulations with ADP, Pi, and Mg^{2+} bound to myosin and three simulations with dADP, Pi, and Mg^{2+} bound to myosin were performed. These simulations are referred to as ADP and dADP simulations throughout this manuscript. Furthermore, while we discuss dADP binding or dADP-induced changes to the binding pocket, all of the simulations also included Pi and Mg^{2+}. Each simulation was 50 ns long, and was performed at 37°C and neutral pH. Unless otherwise indicated, values provided below are averages of all three simulations of a given condition over the last 30 ns of simulation time. Error values given are the standard deviations between simulations.

5.3.1 Effects of dADP binding on the nucleotide binding pocket of myosin

To investigate the local effects of dADP in the nucleotide binding pocket of myosin, we specifically assessed the atomic contacts that were altered as a result of removing the O2' from the starting structure. In the ADP simulations Phe129 Cα, Cδ1, and Cε1 spent over 65% of the simulation time in

contact with O2’ (Figure 5.2). In the dADP simulations, however, there were contact changes in the binding pocket due to the absence of the O2’, altering the Cα, Cδ1, and Cε1 contacts. Instead, these atoms primarily contacted the C5 and C6 on the adenine portion of dADP and established new intramolecular contacts with Gln662 and Leu663. Phe129 also lost contact with Arg131 in the dADP simulations. These immediate changes in the nucleotide-binding site initiated a cascade of changes in intramolecular interactions that resulted in global changes to myosin’s conformation.

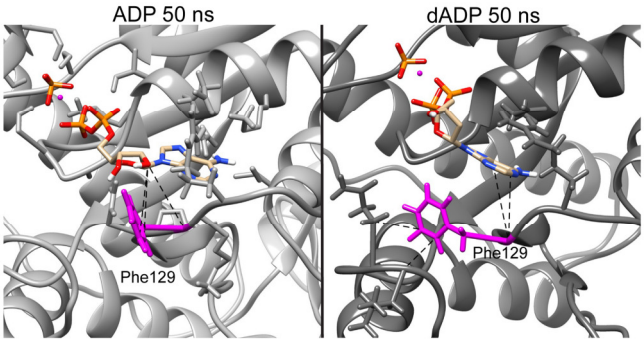

Figure 5.2. Loss of O2' disrupts contacts in the nucleotide binding pocket. Representative figures showing the conformation of the nucleotide binding pocket at 50 ns from ADP and dADP simulations. Phe129 is highlighted in magenta, and the primary contacts it makes are shown with a dotted black line.

To further assess the local dADP-induced conformational changes to the binding pocket, we performed root-mean-squared-deviation (RMSD) analysis of the Cα atoms of the myosin binding pocket residues (considered to be any residue that made contact with the nucleotide throughout the simulation). The binding pocket residues were also used in the alignment for the RMSD calculation, and as such this measurement reflects local changes to the binding pocket conformation. These binding pocket residues are involved in coordinating the nucleotide and experienced larger conformational changes with bound dADP as compared to ADP (2.5 ± 0.2 Å vs. 1.9 ± 0.6 Å). While this local shift appears to be fairly minor, it was associated with a dramatic loss of contacts between myosin and dADP, Pi, and Mg^{2+}, which are critical for maintaining a closed nucleotide binding pocket (Figure 5.3 and Figure 5.4). Myosin maintained ~240 atomic contacts with ADP, Pi, and Mg^{2+} over the course of simulations. However, ~5 ns into the dADP simulations, myosin lost ~20% of its contacts with the nucleotide, Pi, and Mg^{2+}, a change that persisted for the rest of the simulation. The loss of these intermolecular contacts was associated with a change in the position of both the binding pocket and the position of the nucleotide within the pocket (Figure 5.3 B).

The N6 nitrogen on the adenine ring of dADP moved away from its myosin binding partners (Asn188 and Lys191) during all three simulations. In simulations #2 and #3, the distance between dADP N6 and Asn188 Cα increased from ~5 Å to ~ 10 Å from 0-5 ns. In simulation #1 this distance remained stable at ~5 Å until 28 ns into the simulation when it increased to ~8 Å. The average distance between dADP N6 and Asn188 Cα over the last 20 ns of simulation time was 10.2 ± 1.6 Å across all three simulations. In contrast, in all three ADP simulations, it maintained the ~ 5 Å distance between dADP N6 and Asn188 Cα throughout. The average distance between ADP N6 and Asn188 Cα over the last 20 ns of simulation time was 5.1 ± 0.8 Å across all three simulations. The distance between Lys191 and nucleotide N6 mirrored what was observed between Asn188 and N6 in terms of the

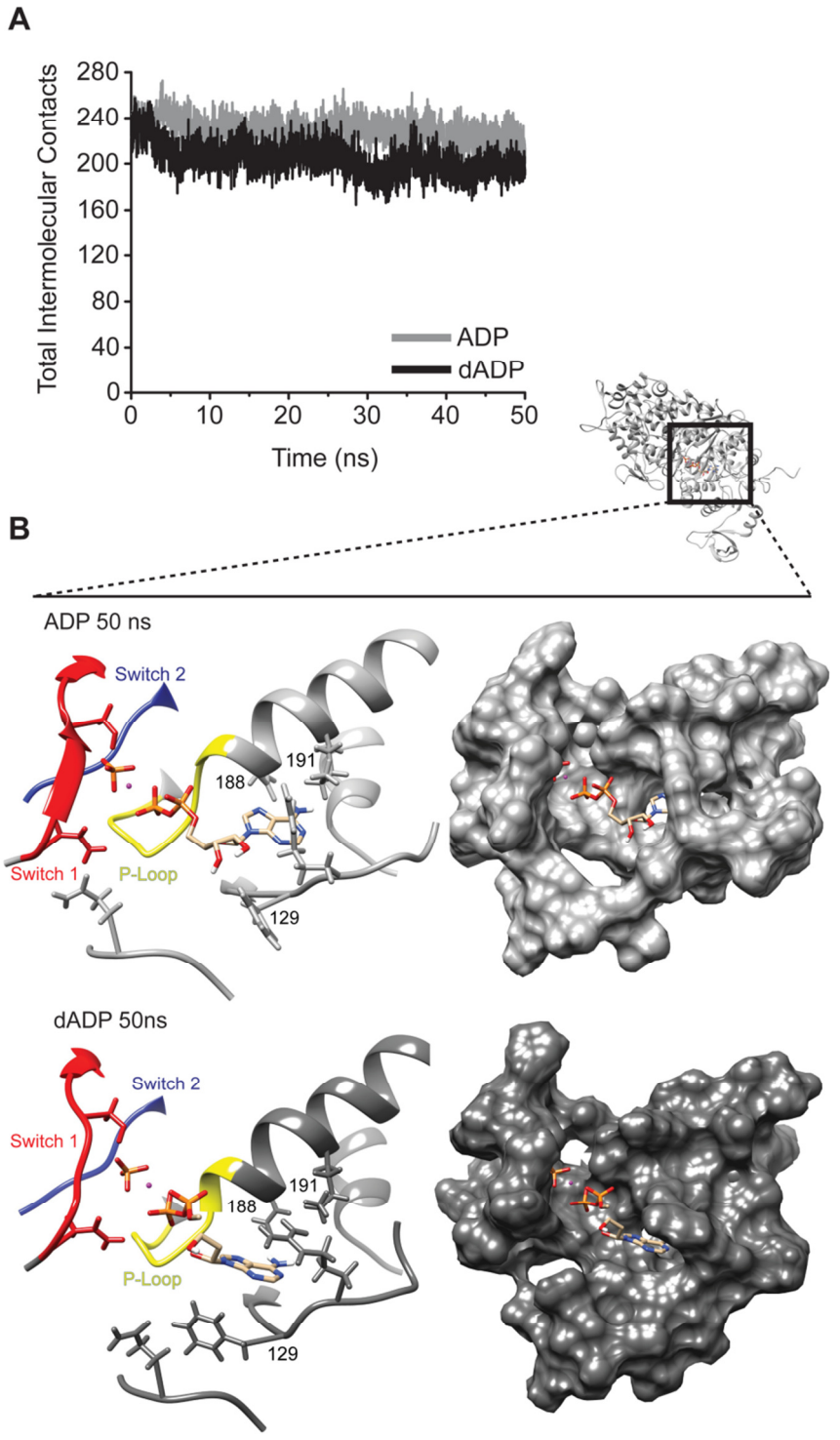

Figure 5.3. The nucleotide binding pocket conformation is altered in dADP simulations. (A) Total number of contacts made between myosin and the nucleotide, Pi, and Mg^{2+} averaged over the three simulations for each condition. (B) Ribbon diagram and surface renderings of representative binding pocket structures highlighting the conformational differences between the binding pocket in the dADP (dark grey) and ADP (light grey) simulations. Small myosin structure shows region of focus.

timing of events and magnitude of change. In simulations #2 and #3, the distance between dADP N6 and Lys191 Cα increased from ~8 Å to ~ 12 Å from 0-5 ns. In simulation #1, this distance remained stable at ~8 Å until 28 ns into the simulation when it increased to ~11 Å. The average distance between dADP N6 and Lys191 Cα over the last 20 ns of simulation time was 11.8 ± 1.2 Å across all three simulations. In contrast, in all three ADP simulations, it maintained an ~ 8 Å distance between dADP N6 and Lys191 Cα throughout. The average distance between ADP N6 and Lys191 Cα over the last 20 ns of simulation time was 7.6 ± 1.1 Å across all three simulations.

The increased distance between the dADP N6 and Asn188 and Lys191 reflects the loss of interactions between dADP and the binding pocket compared with ADP. Asn188 was in contact with ADP for 100%, 86%, and 45% of the time in simulations #1, #2, and #3, respectively. Lys191 was in contact with ADP for 100%, 72%, and 100% of the simulation time. In contrast, for the dADP simulations the Asn188-dADP contact was only intact for 13%, 4%, and 0.3% of the time, and the Lys191-dADP contact was present for 54%, 6%, and 5% of the time. These data highlight a significant number of alterations to the binding pocket when myosin hosts dADP vs. ADP. As can be seen in Figure 5.3 B and evidenced by the distance measurements described above, not only was the conformation of the binding pocket altered in the dADP simulations, but so was the position of the nucleotide.

The p-loop, Switch 1 (SW1), and Switch 2 (SW2) (Figure 5.4 A) coordinate the nucleotide and undergo conformational changes throughout the cross-bridge cycle to mediate nucleotide binding and release. While the p-loop conformation was similar across all simulations, the conformation and dynamics of the switch regions differed between dADP and ADP simulations. The switch regions and nucleotide, phosphate, and Mg^{2+} moved away from each other in dADP simulations, disrupting key contacts required for a “closed” binding pocket conformation. A histogram showing the number of times SW1 was a given distance from the PB atom on ADP or dADP group (phosphorous that is furthest away from adenine) (Figure 5.4 B) illustrates how the position of SW1 was more stable in dADP simulations, favoring two distances as evidenced by the bimodal distribution of structures with highly populated regions from 7.4-7.6 Å and from 8.8-9.0 Å. In contrast, the ADP distribution was wide and diffuse, forming a large populated region with distances ranging from 7.4–8.2 Å. The distance between the SW1 region and PB was greater than 8.4 Å for only ~15% of the ADP simulations vs. ~45% of the dADP simulations. Similarly, a histogram counting the number of times SW2 was a given distance from PB (Figure 5.4 B) demonstrates that the position of SW2 was more stable in the dADP simulations than in

the ADP simulations. The distribution of ADP structures was broad, however, with the most populated region between 8.2-8.8 Å. The dADP structures formed a prominent single peak with the most populated region ranging between 10.4-11.0 Å. The distance between the SW2 region and PB was greater than 10.4 Å for only ~25% of the ADP simulations vs. ~65% of the dADP simulations.

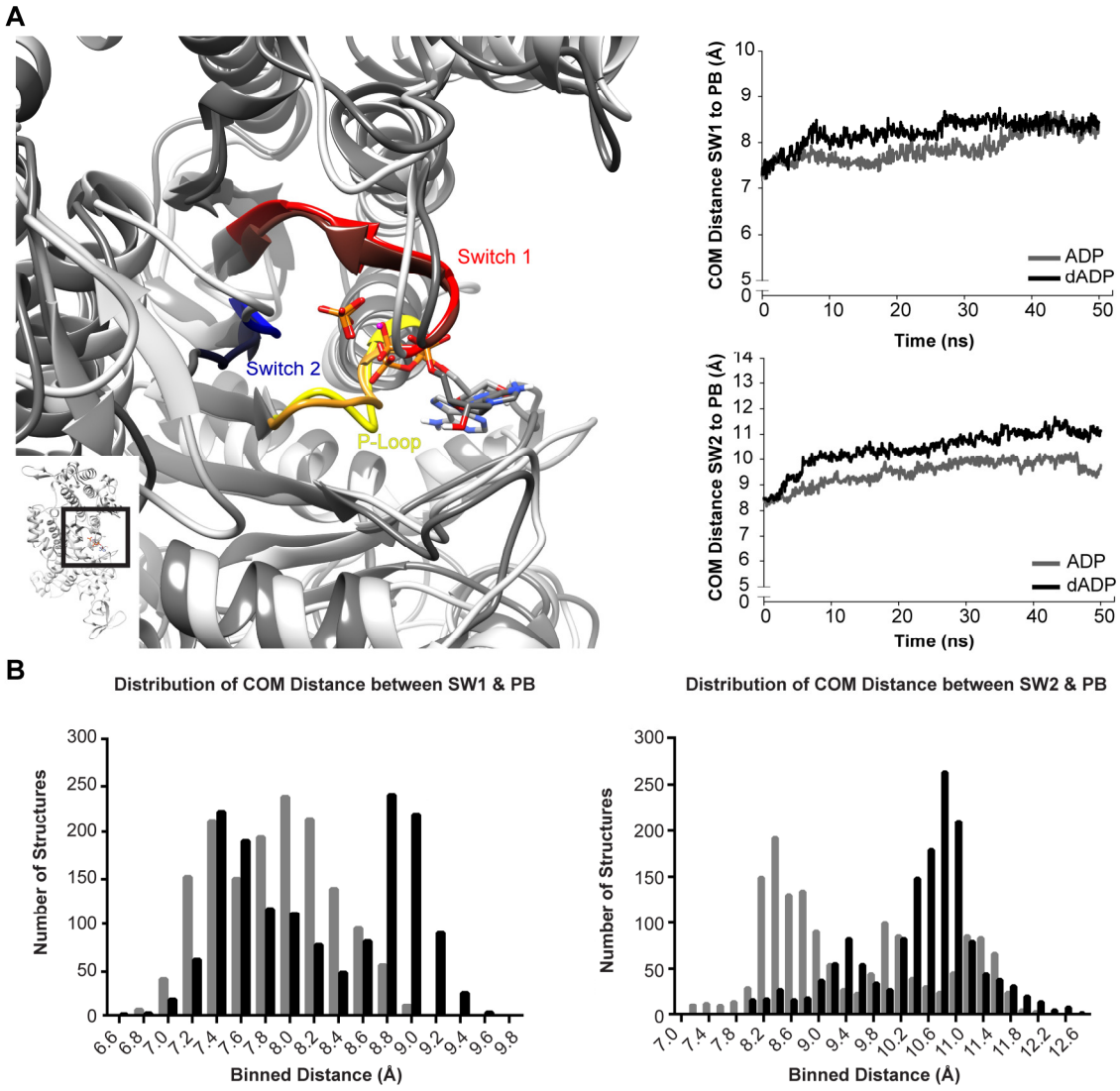

Figure 5.4. Alterations to the conformation of the switch regions, nucleotide, Pi, and Mg^{2+} observed in dADP simulations. (A) Representative 50 ns structures of the binding pocket demonstrate minimal differences in the p-loop (yellow) between ADP (light grey) and dADP (dark grey) simulations in contrast to dramatic alterations to the position of the switch regions (switch 1, red; switch 2, blue). The entire myosin head is shown on the left corner with the boxed region highlighting the region of interest shown larger to the left. Plots quantify the distance between the center of mass (COM) of switch I (SW1) and switch II (SW2) and PB over time. (B) Histograms highlight that there are more instances of structures with increased distance between the switch regions and Pi when dADP is bound vs. ADP.

These data are represented as average distance vs. time in Figure 5.4 A (right panel), which highlights the motion of these regions over the course of the simulations. The difference in the switch conformation in the dADP simulations prevented the maintenance of contacts that typically secure the nucleotide in a "closed" binding pocket [55, 126–130]. The p-loop, SW1, and SW2 regions are addressed in turn, in more detail below.

p-loop

Unlike the role of the switch regions in allosteric regulation, the role of the p-loop in communicating between the nucleotide binding pocket and the actin binding surface has not been studied extensively. It is known, however, that contacts between the p-loop and the nucleotide are critical in coordinating the nucleotide in the binding pocket [55, 126, 131]. Our simulations suggest that there are minimal differences between how dADP and ADP interact with the p-loop. Contacts that persisted for over 90% of the ADP simulations between p-loop residues and both the nucleotide and Pi also persisted for > 90% of the time in all of the dADP simulations with one exception. This exception was in dADP simulation #2 where Ser181 was only in contact with dADP for 5% of the simulation, as compared to 96% and 95% in the other two simulations (and over 90% in all three ADP simulations). The distance between the center of mass of the p-loop and the nucleotide was also unchanged in ADP vs. dADP simulations. It was stable and maintained its shape throughout the course of all six simulations. We did not observe a significant change in the twisting in the central beta sheet between ADP and dADP simulations, which supports the conclusion that there is minimal dADP-induced movement in the p-loop.

Switch 1

Switch 1 (SW1) is thought to communicate between the nucleotide binding pocket and the actin binding surface, sensing changes from NTP to NDP, and undergoing conformational shifts that alter affinity for the nucleotide and/or actin. The conformation of SW1 is largely dictated by its interaction with the nucleotide and influences myosin's interaction with actin, where the "open" conformation of SW1 binds actin more tightly than the "closed" conformation of SW1 [55, 129, 130]. SW1 is defined as "open" when Ser237 does not interact with the Mg^{2+} ion [126]. In all three of the ADP simulations, Ser237 was in contact with the Mg^{2+} ion for over 99% of the simulation time. In the dADP simulations, Ser237 contact with the Mg^{2+} ion was more variable, with interaction times for individual simulations being 65%, 99%, and 11% (contact breaks at 26.4 ns, and 5.7 ns for simulation #1, and #3, respectively). In addition to the loss of contact with Mg^{2+}, the SW1 residue Asn233 lost contact with Pi and the nucleotide in the dADP

simulations. The contact between Asn233 and Pi was present for 17%, 31%, and 68% of the three ADP simulations, but only 13%, 7%, and 9% of the dADP simulations. The contacts between Asn233 and the nucleotide were present for 19%, 100%, and 85% of the ADP simulations, but only 47%, 12%, and 29% of the dADP simulations (Figure 5.5). The loss of key intermolecular contacts between SW1 and nucleotide, Pi, or Mg^{2+} demonstrate dADP-induced increase in the propensity of SW1 to adopt an "open" conformation.

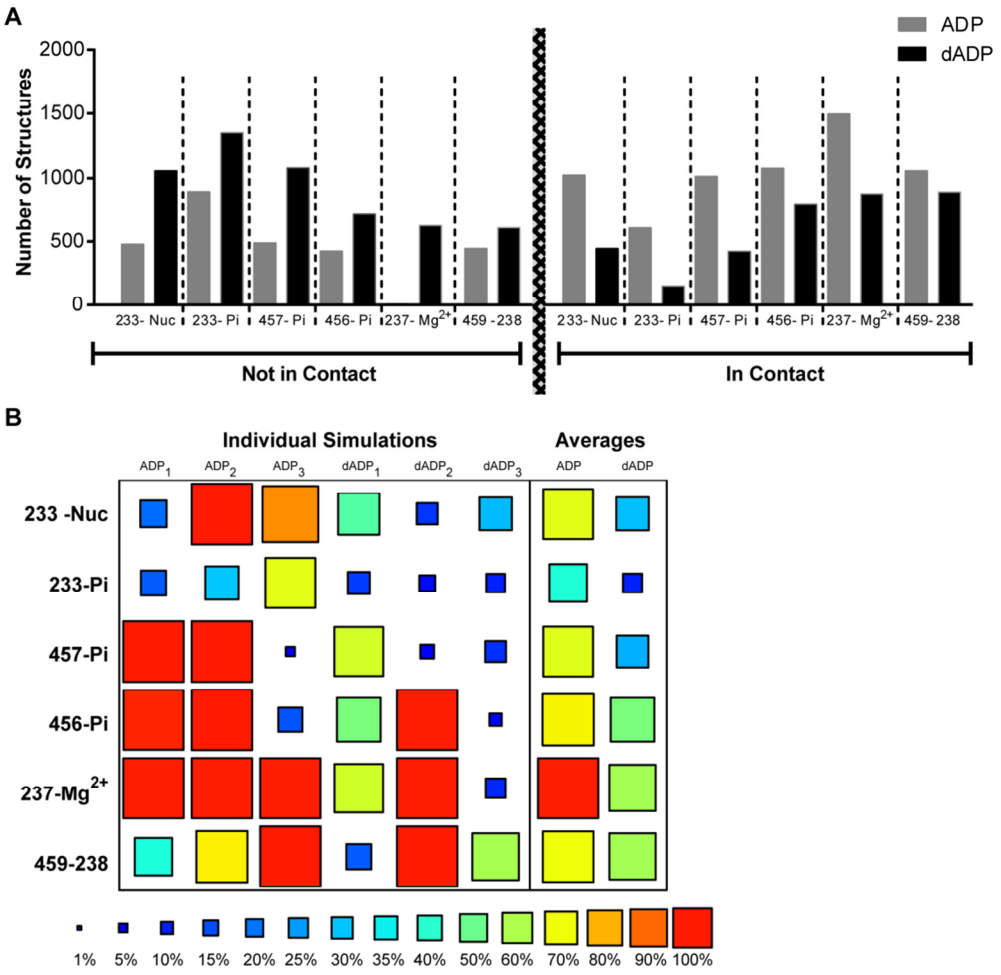

Figure 5.5. Analysis of key switch region contacts that are broken in dADP simulations. (A) An assessment of the number of structures that contain key contacts vs. those that don't. 100 ps sampling of each 50 ns data set was used, and shows whether the following contacts are intact: Asn233 and the nucleotide, Asn233 and Pi, Gly457 and Pi, Ser456 and Pi, Ser237 and Mg^{2+}, and GLU 459 to Arg238. The y-axes measure the number of instances that a contact is either broken or intact. The bars on the left side of the graft measure instances when the contact is broken, and those on the right measure when it is intact. These data highlight that there are more dADP structures with key contacts broken than ADP structures (which predominately populate the contact intact state), indicating that there is an increased number of dADP simulations that populate the "open" conformation of both switch I and switch II. (B) A summary of the percent time each contact is intact. These data demonstrate that while there is no uniform switch from contacts intact to broken with dADP, these key contacts are, on average, present for less time in the dADP simulations than the ADP simulations.

Switch 2

The Gly457 (SW2 residue) interaction with Pi is necessary for ATPase activity, and it is lost in the strong actin binding state when SW2 is in the "open" position [55, 126–128, 132, 133]. The loss of contact between Gly457 and Pi was also observed in Targeted Molecular Dynamics (TMD) simulations of myosin binding to actin [128]. The conformational change of SW2 and the loss of the essential hydrogen bond with Gly457 are proposed to initiate phosphate release and the powerstroke [128], and they are also thought to be hallmarks of a myosin conformation preferred by actin [127]. We observed a reduction in the contacts between Gly457 (SW2 residues) and Pi, and neighboring residue Ser456 and Pi in the dADP simulations (457-Pi: 100%, 100%, 2% in ADP simulations vs. 65%, 5%, 12% in dADP simulations; 456-Pi: 99%, 100%, 16% in ADP simulations vs. 52%, 100%, and 4% in dADP simulations) (Figure 5.5).

Analysis of the conformation of the p-loop and switch regions as well as their interactions with the nucleotide, Pi, or Mg^{2+} demonstrates that dADP-induced structural and dynamic changes result in overlapping, but distinct, distributions of conformational states. There were more instances where a critical contact was broken between myosin and the nucleotide, Pi, or Mg^{2+} with dADP compared with ADP simulations (Figure 5.5). This loss of critical intermolecular contacts in dADP simulations indicates that dADP enables a more "open" conformation of both SW1 and SW2, a conformational state that is associated with weak nucleotide binding and strong actin binding. Importantly, even though there was an increase in the time that switch regions adopted a more "open" conformation in the dADP simulations (as evidenced by position and loss of contact with the nucleotide, Pi, and Mg^{2+}), there were no contacts between Pi and regions of myosin outside of the "binding regions" (p-loop, switch 1, and switch 2). Cecchini et al. determined that contacts between Pi and residues outside of the binding regions are indicative of Pi progressing through the exit tube before release, and that when Pi is stable in the binding pocket, there are only interactions between the p-loop, switch 1, and switch 2 regions [126]. Our data, therefore, suggest that even though the switch regions may be more open with dADP, Pi was stable in the binding pocket and did not proceed through the exit tube, which would indicate release. The stability of Pi in pre-powerstroke myosin is important as it can prevent myosin from going through the powerstroke before binding to actin [126].

The altered position and contacts of the switch regions, combined with the loss of contacts between other myosin residues that coordinate the nucleotide, resulted in a more mobile nucleotide that was also more exposed to solvent. dADP had both a higher RMSD than ADP (5.1 ± 0.4 Å vs. 3.3 ± 1.2 Å, respectively) and a higher solvent accessible surface area (SASA) vs. ADP (153.6 ± 6.03 $Å^2$ vs. 88.1 ± 22.6 $Å^2$, respectively) (Figure 5.6). An analysis of the binding pocket conformation demonstrates that dADP initiates a cascade of contact changes beginning with Phe129 that result in an altered binding pocket conformation. Ultimately, dADP was further away from the switch regions (and more exposed to the solvent) than ADP, which prevented contacts between dADP, Pi, and Mg^{2+}, and residues critical for a "closed" nucleotide binding pocket. Thus, the most populated states in the dADP simulations resembled a more "open" conformation, as is typically seen in the strong actin binding states [55, 126–128, 132, 133]. The observed alterations to the binding pocket provide insight into the mechanism by which dADP.Pi activates myosin to increase cross-bridge attachment, as they highlight dADP–induced stabilization of a conformation of myosin that is typically observed in strong actin-binding states.

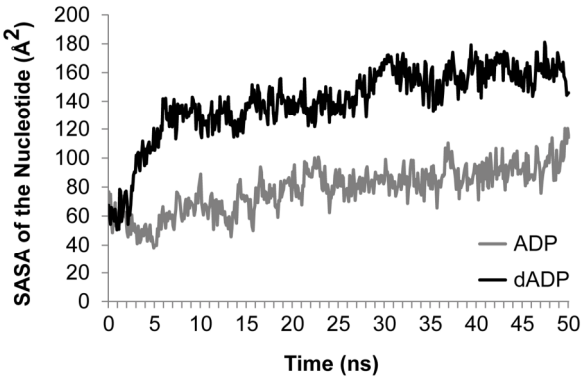

Figure 5.6. Solvent accessibility of ADP and dADP over time highlights that dADP is more exposed than ADP. SASA was calculated and averaged for ADP and dADP. These data highlight that the movement of the switch regions and altered conformation of the binding pocket in dADP simulations that result in an open binding pocket and a higher SASA of dADP than ADP.

5.3.2 Effects of dADP on the cleft orientation

The extent to which the actin binding cleft is open vs. closed is thought to predict whether myosin binding to actin is energetically favorable. Open-cleft conformations of myosin bind to actin endothermically in contrast to closed-cleft conformations of myosin, which can bind exothermically [134]. We assessed the openness of the actin binding cleft by measuring the angle between the helices bordering the cleft on the lower 50k domain (w-helix, residues 630-646) and the upper 50k domain (HO helix, residues 411-442). The helices and vectors used to measure this angle are shown from two different views in Figure 5.7 A. The cleft angle measurements suggest that dADP stabilized a closed cleft conformation of myosin and specifically highlight the closure of the outer cleft (the portion closest to the actin binding site). Interestingly, in the ADP simulations, the cleft slowly opened throughout the

course of the simulation; at 9 ns into the simulation the cleft angle was ~28° and by 25 ns the cleft angle reached approximately 33° where it remained for the rest of the simulation (Figure 5.7 B). In addition to measuring the angle of the cleft, we also calculated the distances between residues on the inner (inner cleft, residues 277-465; far inner cleft, residues 232-461) and outer (outer cleft, residues 416-589; far outer, residues 365-536) portions of the cleft that have been previously used to assess cleft closure across different species of myosin and in different states of the cross-bridge cycle [135]. These pairs are highlighted by space-filled residue rendering in (Figure 5.8). Even though some of these atoms reside in flexible loop regions, this analysis demonstrates that dADP stabilized the closed cleft conformation. Figure 5.8 B shows a histogram of structures from dADP and ADP simulations for each of the residue pairs listed above. The narrowness of the dADP distribution relative to the ADP distribution highlights the stability of the myosin cleft structure with ADP. The ADP-bound myosin sampled a wider range of distances, reflecting fluctuations in the cleft with a propensity for increased distances (in particular in the outer cleft measurements).

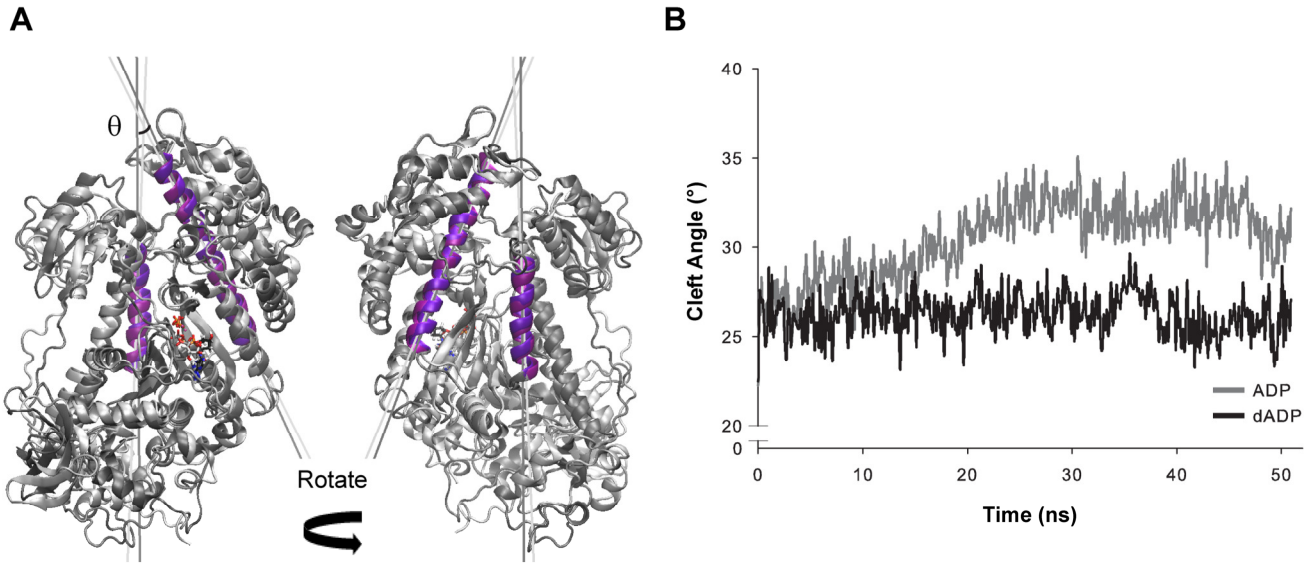

Figure 5.7. Cleft analysis using helix-helix measurement highlights dADP stabilization of the closed cleft conformation. (A) Representative structures are shown to highlight the w-helix and HO Helix that are used to measure cleft angle. ADP structure shown in light grey, and dADP structure shown in dark grey. Purple helices are those that were fit by vectors used to calculate the cleft angle. Light purple is used on the ADP structure and dark purple on the dADP structure. Vectors used to calculate cleft angle are represented by light gray (ADP) and dark grey (dADP) lines. (B) Cleft angle was calculated at the point of intersection of these vectors. Vector angle quantification is shown over time and indicates that dADP stabilizes a closed cleft conformation as compared to ADP. Figure 6A generated using VMD (http://www.ks.uiuc.edu/Research/vmd/) [158, 159].

This analysis also indicates that the outer portion of the cleft was more closed in the dADP simulations. However, by this measure, the inner cleft was slightly more open in the dADP vs. ADP simulations, though it was also more stable than the ADP simulations. The openness of the inner cleft was due to movement of the residues on the lower 50k domain (Phe461 and Ser465).

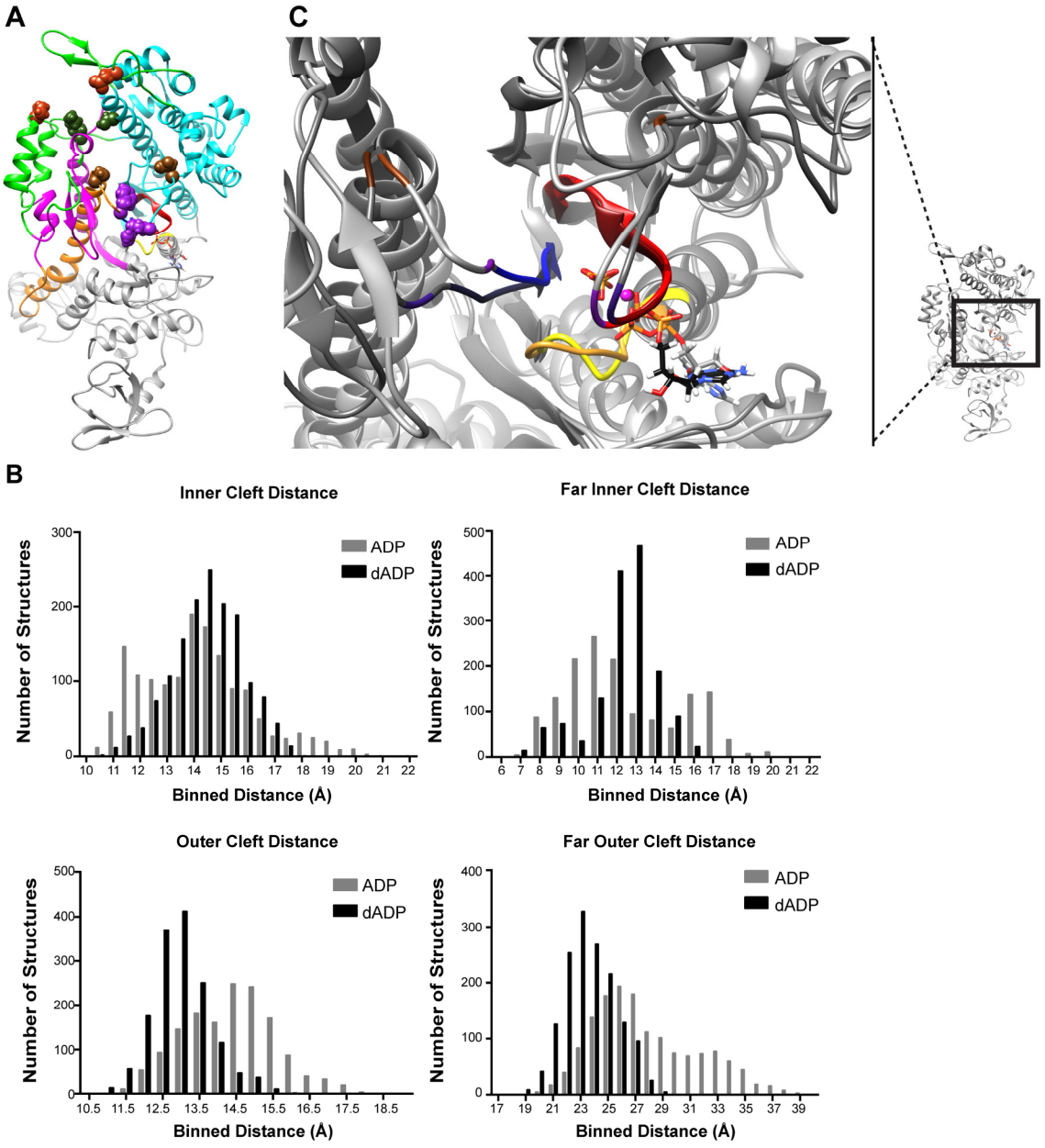

Figure 5.8. Cleft analysis using residue-residue distance highlights dADP-induced closed outer cleft. Representative structure highlights the residues used in this analysis (shown as spheres) (A). Histogram of structures taken at 100 ps resolution highlight the structures from dADP simulations populate a more closed-cleft (residues closer together) state (B). Representative 50ns structures highlight the movement of residues on the lower 50k region, 461 (purple) and 465 (brown), away from their partner on the upper 50k region, 232 (purple) and 277 (brown), in dADP simulations vs. ADP simulations. Reference structure is shown with detail region shown in boxed region (C).

While residues on the upper 50k domain (Arg232 and Asn277) were in a relatively similar position throughout both ADP and dADP simulations, Phe461 and Ser465 moved away from their upper 50k counterparts in the dADP simulations as a result of the opening of SW2 (residues 454-459) (Figure 5.8 C), as described above. In fact, the mean, median, and mode of the far inner cleft measurement (which contains the residue closest to SW2) of the dADP simulations are nearly identical to the reported distance in the myosin post-rigor crystal structure, 1MMD [136], where it is expected that SW2 is open [55, 135]. Despite the opening of the inner cleft in these simulations, the outer cleft was maintained in a more closed position. This dADP-induced stabilization of the cleft conformation with a closed outer region may underlie the increased cross-bridge attachment and rate of force development observed with dATP *in vitro* [12].

5.3.3 Effects of dADP on the actin binding surface

The initial binding interaction between actin and myosin in the pre-powerstroke state is primarily electrostatic in nature [102, 137–139], and the rate of attachment and ATPase activity can be dramatically affected by the positive charges presented on myosin's actin binding surface [139–141]. Consequently, we assessed the solvent accessible surface area (SASA) of the positively charged residues on the actin binding surface of myosin, with particular focus on Loop 2, where the charge density has been shown to mediate ATPase activity [139–141]. In the dADP simulations, there was a moderate increase in the SASA of all positive side chains of residues on the actin binding surface compared with the ADP simulations (616.6 $Å^2$ ± 38.6 $Å^2$ vs. 594.0 $Å^2$ ± 32.6 $Å^2$ respectively)(Figure 5.9). Further analysis of Loop 2 indicates more of a shift toward increased polar residue exposure in the dADP simulations. Not only was there an overall increase in the mean of Loop 2 polar SASA with dADP (270.8 ± 26.2 $Å^2$ (ADP) vs. 315.3 ± 21.3 $Å^2$ (dADP)), but there was also a narrower distribution of dADP structures with more instances of higher Loop 2 polar SASA (Figure 5.9 B). This distribution indicates that dADP stabilized a conformation of myosin with increased polar SASA of Loop 2 residues. Figure 8C further highlights this shift in the distribution of structures favoring increased polar SASA in dADP vs. ADP simulations. For example, ~50% of the dADP structures had polar SASA of 300 $Å^2$ or greater vs. ~25% of ADP structures. These results indicate that there was an increase in the occurrence of higher SASA of polar loop 2 residues and positively charged actin binding residues in dADP simulations and that the distribution was positively skewed as opposed to the negative skew in the ADP data (Figure 5.9 B).

It is difficult to correlate the increase in Loop 2 polar SASA to the increase in charge of Loop 2 previously studied [139, 141]. This is particularly true in the case where increased charge was achieved in combination with increasing the number of residues in Loop 2, which can change the flexibility and packing of that region [139].

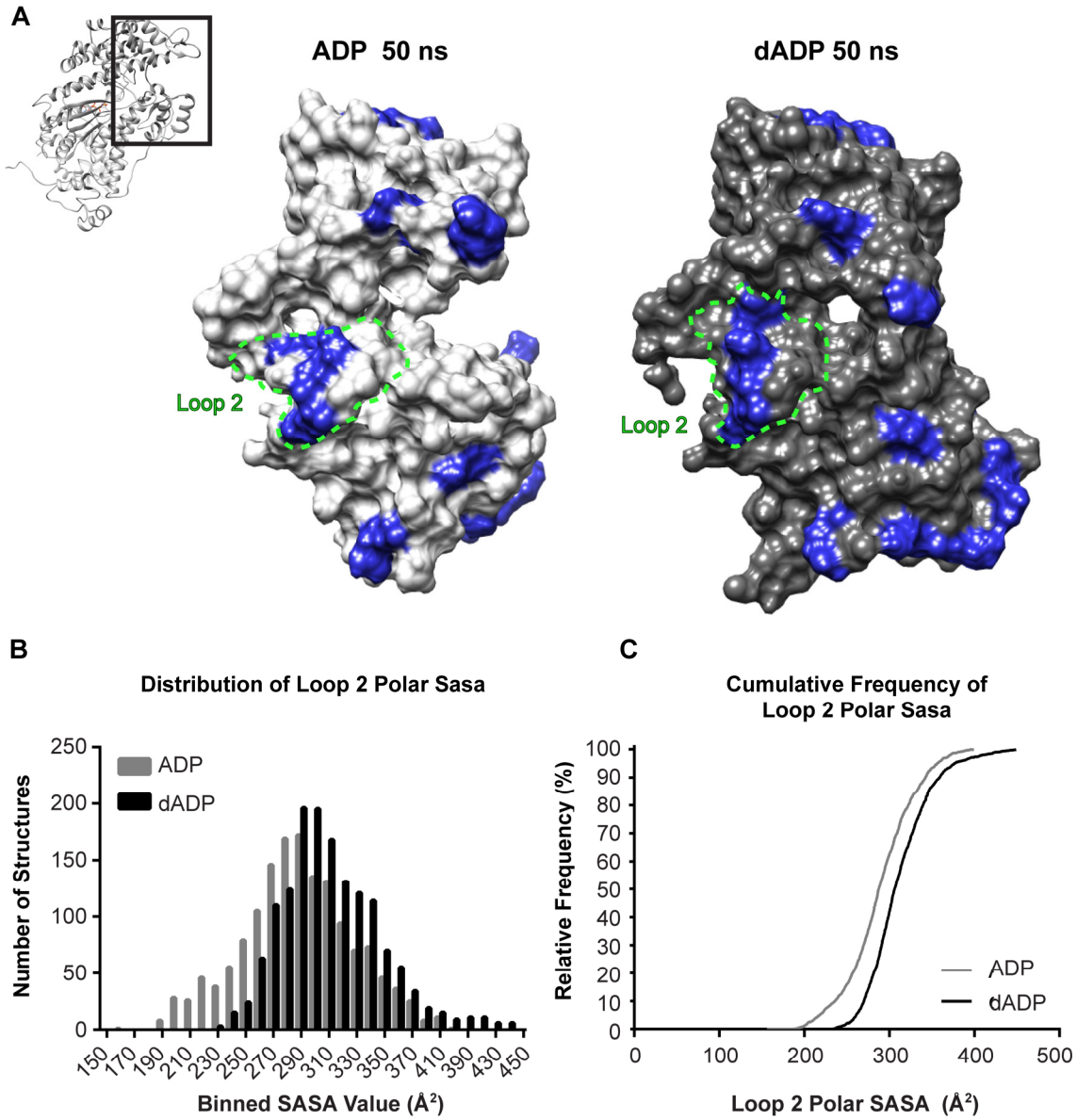

Figure 5.9. Assessment of dADP-induced alterations to the actin binding surface. (A) Representative actin binding surface structures at 50 ns from ADP and dADP simulations. For reference, the entire S1 is shown where the boxed region indicates the region that is shown with a surface rendering. Blue highlight indicates positively charged residues. These residues are more exposed to the solvent in the dADP simulations. (B) 100 ps granularity data used to populate histogram, which highlights the right shift of the distribution of Loop 2 polar SASA values in dADP simulations. (C) This effect is further evidenced by the cumulative frequency plot that demonstrates at any SASA value observed, there is a higher fraction of dADP structures that have higher SASA values than ADP structures.

If, however, we assume that altering the sequence of Loop 2 by adding lysines does not alter the region's propensity for solvent exposure, we can use the ADP and dADP simulations to consider the possible effect of adding three lysines (as was done in Joel et al., 2003) to the polar SASA of Loop 2. In the dADP and ADP simulations, the average polar SASA of the lysines ranged from 35-65% of the total potential polar SASA when fully exposed to solvent (99.1 $Å^2$ [142]).

The three lysines that were added by Joel et al. replaced two serines and a methionine (max potential polar SASA of 87.9 $Å^2$ and 51.0 $Å^2$, respectively). Thus, the net increase in potential polar SASA achieved from the substitution of three lysines for two serines and a methionine is 70.4 $Å^2$). Using the percentage of total potential polar SASA observed for lysines in Loop 2 in the dADP and ADP simulations (35-65%), the lysine substitutions used by Joel et al. could increase Loop 2 polar SASA by ~25-46 $Å^2$. The average difference between Loop 2 polar SASA in dADP simulations and Loop 2 polar SASA in ADP simulations was 23.2 $Å^2$, and the max difference (average over a 10 ns interval) was 50.7 $Å^2$. These data suggest that the effect of dADP on Loop 2 polar SASA is of similar magnitude to the effect of substituting 3 lysines for 2 serines and a methionine. Joel et al. demonstrated that the substitution of three lysines reduced the K_m of HMM for actin by 15 fold. The increase in polar SASA on Loop 2 observed in dADP simulations, therefore, suggests that dADP increases the affinity of myosin for actin.

Together, these analyses suggest that having dADP in the nucleotide binding pocket results in allosteric modification to the actin binding surface. Correlation analysis demonstrates that the SASA of polar residues on loop 2 is inversely related to the cleft angle measurement in ADP simulations, with the strongest relationship appearing in ADP simulation #2. The cleft is the most open in ADP simulation #2, and has the lowest polar residue SASA of Loop 2 (Figure 5.10). There is very little correlation between cleft angle and Loop 2 SASA, which reflects the stability of these parameters in the dADP simulations. dADP stabilizes a closed cleft conformation, which in turn, stabilizes the exposure of polar residues on Loop 2. The resulting cluster of stable conformations with high polar residue exposure on Loop 2 and closed cleft can be seen in Figure 5.10. Further evidence of this relationship can be observed by examining the average Loop 2 polar SASA at different time intervals. Whereas the average Loop 2 polar SASA remains relatively constant over the entire 50 ns simulation [mean ± SD SASA equal to 303.7 ± 9.8 $Å^2$ from 0-10 ns, 309.3 ± 21.0 $Å^2$ from 10-20 ns, 316.0 ± 30.9 $Å^2$ from 20-30 ns, 319.3 ± 27.6 $Å^2$ from 30-40 ns, 310.7 ± 9.6 $Å^2$ from 40-50 ns], the average Loop 2 polar SASA starts to decrease shortly after the cleft opens in the ADP simulations [mean ± SD SASA equal to 320.9 ± 11.9 $Å^2$ from 0-10 ns, 309.8 ± 21.9

$Å^2$ from 10-20 ns, 283.2 ± 15.0 $Å^2$ from 20-30 ns, 270.0 ± 36.0 $Å^2$ from 30-40 ns, 259.1 ± 29.1 $Å^2$ from 40-50 ns]. Others have demonstrated that increasing the charge of the actin binding surface on myosin can increase acto-myosin interaction and ATPase [139, 141], and we hypothesize that the increase in charged surface area increases the affinity of myosin for actin in the presence of dADP, thereby increasing the probability of cross-bridge attachment.

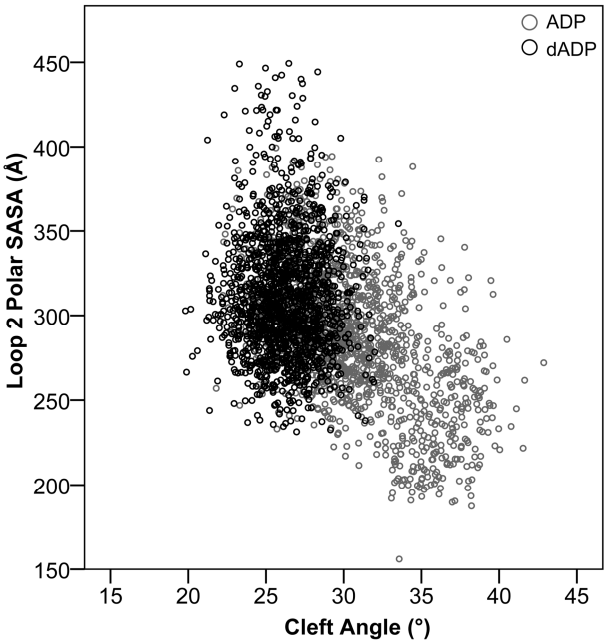

Figure 5.10. Correlation assessment of Loop 2 polar SASA and cleft angle highlights dADP stabilization of a closed cleft conformation and increased polar residue exposure on the actin binding surface. 100 ps resolution data points were used to calculate the Pearson product-moment correlation coefficient (*r)* for Loop 2 polar SASA and cleft angle for both ADP and dADP correlations. The scatter plot of these data points is shown. In ADP simulations, these values have a negative correlation with an *r* value of -0.507. In dADP simulations, the data cluster around one area of the curve and are not well correlated, *r* = -0.028. These results demonstrate that dADP stabilizes a closed cleft conformation that also stabilizes polar residue exposure on Loop 2. In ADP simulations, when the cleft opens, this reduces the exposure of polar residues on Loop 2.

5.3.4 *In vitro* motility analysis

In vitro motility (IVM) assays are commonly used to study the actin-myosin interaction under different conditions (e.g. temperature, pH, and ionic strength). The ionic strength of motility solutions typically ranges from 40–100 mM, because lower ionic strengths (compared to physiological) are required for actin to stay on myosin-coated surfaces. Solutions with ionic strength over 100mM tend to disrupt the electrostatic interactions between actin and myosin in the weak-binding state, resulting in dissociation of actin and loss of movement [139, 143]. Decreasing the nucleotide concentration in motility solutions combats this loss of actin filaments on the surface as ionic strength is increased, though motility is slowed. We hypothesized, based on the increased exposure of polar groups observed in the pre-powerstroke state *in silico*, that more actin filaments should stay on myosin-coated surfaces as the ionic strength is varied when 0.1 mM dATP is the substrate (vs. 0.1 mM ATP). This concentration is near the Km for actin motility in the assay for both ATP and dATP [13], and was selected to ensure that enough

filaments would land and be motile on the surface for rigorous comparisons. The substrates are hydrolyzed by myosin to dADP and Pi (vs. ADP and Pi) prior to addition of actin, and enable us to experimentally examine the propensity of pre-powerstroke myosin bound to dADP to bind to actin. This effect is particularly noticeable at 150 mM where more than three times as many actin filaments were moving with dATP than with ATP Figure 5.11. The increase in bound, moving filaments at high ionic strength suggests that dATP (dADP and Pi when hydrolyzed) enhances long-range electrostatic interactions between actin and myosin and supports the idea that enhanced binding (electrostatic) between myosin and actin could occur in myofibrils at physiological ionic strength (~200 mM). This may underlie the observed increases in myosin binding and force production in the presence of dATP [12, 14, 49]. The surface analysis of the dADP simulations suggests a structural correlate that may explain this observation, i.e. dADP may allosterically alter the actin binding surface of myosin, resulting in increased exposure of polar side chains that increases myosin binding to actin. Together, these data demonstrate a potential mechanism for dATP-induced increases in cross-bridge attachment and ultimately in increased force production.

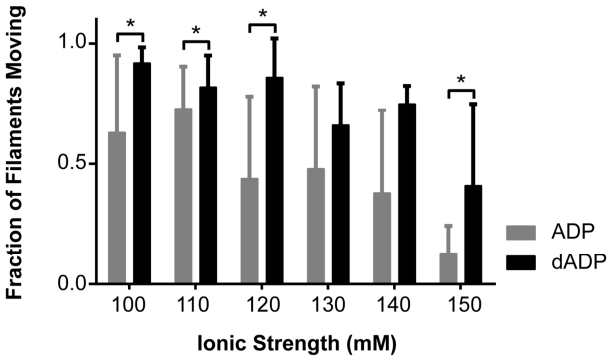

Figure 5.11. The fraction of moving filaments in *in vitro* motility assay with ATP and dATP at increasing ionic strengths. The fraction of moving filaments at ionic strengths 100 mM to 150 mM are shown for conditions with ATP and with dATP. There were between 20 and 1600 filaments measured for each group (number of filaments decreased with increasing ionic strength) on 4-15 slides. Bars represent mean + SD of the fraction of moving filaments. *$p < 0.05$.

5.4 Conclusions

Previous experimental work assessing the functional effects of dATP on myosin and muscle contraction demonstrated that dATP significantly increases the rate of cross-bridge cycling, the magnitude and rate of force development and the rate of relaxation [12, 14, 49]. These results encouraged the development of increased cardiac muscle dATP as a potential therapy for systolic dysfunction [24, 92, 144]. However, little work has been done to understand the structural changes in myosin that elicit these dramatic functional effects. Here, we have employed MD simulations to elucidate the structural effect of dADP binding to pre-powerstroke myosin. The data presented here leverage the atomic resolution of MD simulations and provide insight into the conformational changes that result from dADP binding to

myosin. These simulations indicate that the Phe129 contact with O2' at the 2 position of the ribose ring is a critical contact between myosin and ADP. Upon the removal of a single oxygen atom, significant conformational alterations occur in the binding pocket, which in turn are transmitted across the protein, stabilizing a closed cleft conformation and increasing the SASA of polar groups in Loop 2 on the actin binding surface. These analyses highlight the significance of a single atom and provide insight into how myosin translates conformational changes between the nucleotide binding site and the actin binding surface throughout the cross-bridge cycle (Figure 5.12). Furthermore, these simulations provide novel insight into both how allosteric modifications occur in myosin at the atomic level and provide insight into structural mechanisms that underlie alterations to the cross-bridge cycle. These data could potentially be used in concert with larger-scale models of the acto-myosin network to enable better understanding of how molecular-level changes may affect the macro-level performance [145, 146].

Data from our in vitro motility assays (Figure 5.11) and our previous work [12, 13] strongly suggest that dATP binding to myosin increases the probability of cross-bridge attachment. Thus, based on both the experimental and MD studies, we propose that dADP-induced alterations to the conformation and dynamics of myosin stabilize a myosin conformation that enables more energetically favored actomyosin interactions, which provides a molecular framework for the large body of biochemical data available for this system.

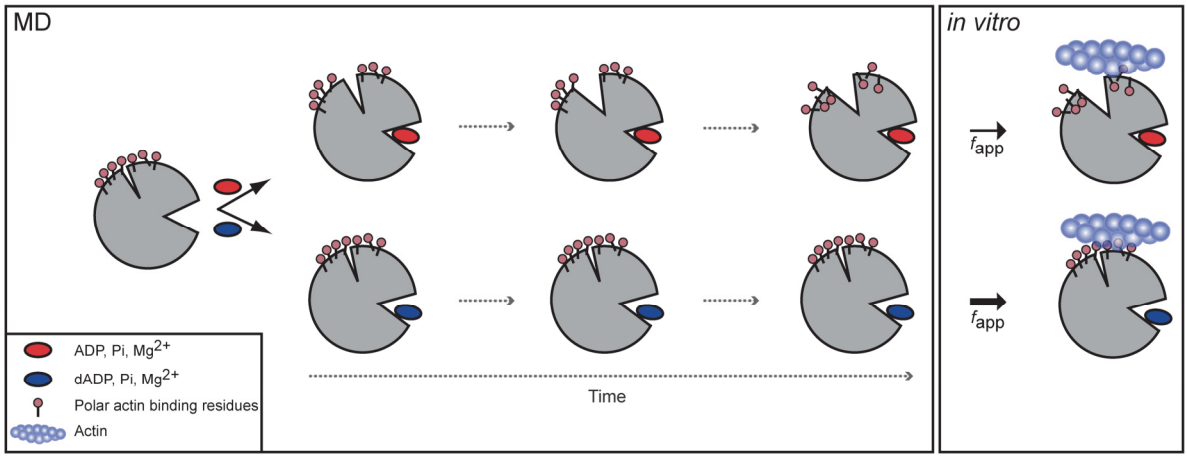

Figure 5.12. Schematic of dADP-induced changes to myosin structure. Simplified overview of allosteric pathway of alterations over time to myosin structure with ADP (top) vs. dADP (bottom). ADP was stable in the binding pocket and maintained contacts with the switch regions, which stabilized a "closed" conformation of the binding pocket. This resulted in an opening of the actin binding cleft over time, which in turn reduced the exposure of polar residues on the actin binding surface. dADP, on the other hand, destabilized the binding pocket. Contacts were broken between the switch regions and the nucleotide, Pi and Mg^{2+}, which stabilized an "open" conformation of the nucleotide binding pocket resulting in increased SASA of the nucleotide. This binding pocket conformation stabilized a closed cleft conformation, which in turn favored increased (relative to ADP simulations) exposure of charged residues on the actin binding surface of myosin bound to dADP. The model predicted that the increased charge on the actin binding surface would result in increased electrostatic interactions between myosin and actin, which was supported by the IVM data (Figure 9) and previous *in vitro* studies [12], and suggests a mechanism by which dATP (and its hydrolysis products, dADP and Pi) increase actomyosin interaction and force production.

CHAPTER 6. MOLECULAR DYNAMICS SIMULATIONS OF MYOSIN MUTATION IMPLICATED IN HYPERTROPHIC CARDIOMYOPATHY

6.1 Introduction

Hypertrophic Cardiomyopathy (HCM) is characterized by a thickening of the ventricular wall and myfibrilar disarray. Not only does this disease affect 1 in 500 people, but it is the leading cause of sudden cardiac death in juveniles [147]. A striking 60-70% of cases of HCM can be attributed to a genetic mutation, and there have been 16 genes implicated in HCM pathology. There are currently over 230 mutations in β-cardiac Myosin Heavy Chain (MYH7) gene that have been reported to result in HCM in humans, and over 145 in the myosin head region alone [147–150]. Even though most of the mutations recorded occur in functional regions (actin binding sight, light chain binding site, ligand binding site, etc.; for reference see section 5.1 and Figure 1.9), there is no clear understanding of how mutations are linked to phenotype [151].

These mutations have been reported following clinical evaluation in humans, but the underlying mechanisms that drive the development of disease have not been well-studied. Clinical reports and *in vitro* studies of kinetics and contraction have allowed the researchers to hypothesize how the location, change in charge, and change in hydrophobicity as a result of mutations in functional domains can lead to severe disruptions in function. For example, a disruption in the hydrophobicity of the actin-binding surface could disrupt the cross-bridge binding process. Due to the large size of the myosin S1 head, few groups have investigated how these mutations affect protein dynamics on a molecular level. To the best of my knowledge, only one group has modeled the acto-myosin interface for longer than 1 ns, and they only carried their studies out to 5 ns.

R403Q (human β-myosin numbering) was the first HCM-causing mutant discovered and results in a severe HCM phenotype [148, 150, 152]. Many have characterized the effects of R403Q on cardiac function. These experiments have ranged from *in vitro* motility and ATPase assays (unloaded myosin + actin) using different myosin isoforms (*Dictyostellium discoideum* (Dicty), rat α-cardiac, mouse α-cardiac, Tg-mouse β-cardiac, human β-cardiac) to measurements of kinetics and isometric force from fibers from affected patients. Even though R403Q has been heavily investigated, there is no consensus in the literature about the effects of R403Q on cross-bridge cycling and the mechanism of R403Q-induced hypertrophy. Some research reports that R403Q enhances ATPase, and increases the rate of contraction

and relaxation (with lower force) [29, 148, 150], while others report that R403Q slows hydrolytic activity and reduces cardiac performance [150, 153–155]. Most work has focused on studying nucleotide release and/or myosin detachment from actin. There has been limited research on R403Q-mediated alterations to pre-powerstroke myosin and actomyosin binding. The work that has been done to assess the attachment processes, however, has demonstrated that R403Q increases the rate of force development [29].

The work presented here is focused on understanding whether R403Q alters the structure or dynamics of pre-powerstroke myosin. Furthermore, because we have also experimented on and simulated myosin bound to dADP.Pi in this state (Chapter 5), and we, therefore understand the functional effects of the structural changes associated with dADP, we can compare the R403Q-induced perturbations to myosin to dADP-induced perturbations to better understand how the mutation alters cardiac phenotype. Multiple, all-atom MD simulations were performed of *Dictyostelium discoideum* myosin S1 head which was crystallized in the pre-powerstroke state (PDB ID:1VOM; [103]) with Mg^{2+},P_i and ADP in the binding pocket. Wild type (WT) simulations are the same as the ADP simulations described in Chapter 5. Mutant simulations were run following alteration to the myosin of Arginine to Glutamine at residue 397, which is the homologous residue to 403 in human β-cardiac myosin. The objective of this work is to investigate any structural or dynamic changes to myosin that result from the R397Q mutation and to compare these data to both the dADP simulations and experiments and to the experiments on this mutated myosin that have been done *in vitro.*

6.2 Materials and Methods

The sequence and residue numbering for Dictyostelium discoideum myosin II are used for the remainder of this chapter.

6.2.1 Model Selection

The crystal structure for pre-powerstroke myosin (PDB ID:1VOM), which was resolved at 1.90 Å was used as a starting structure for all simulations [103]. VO_4 was replaced in all structures by PO_4 (Pi). PO_4 and ADP were parameterized in the Levitt et al. force field [104] using previously established bond length, bond angles, and torsion angles. Partial charges (Figure 5.1) were calculated by running a geometry optimization of each structure in GAMESS [105]. Loops missing from the 1VOM structure were replaced using homology modeling in MODELLER [106–109]. The mutation at position 397 of Arginine

for Glutamine was performed using Chimera [116]. Dictyostelium discoideum myosin was chosen for these studies because it is the myosin II that has been crystalized in multiple conformations at the highest resolution. We sought a myosin that was available in multiple conformations so that we can further study the effects of mutation and on other parts of the cross-bridge cycle. We sought myosin that had been crystalized at high resolution because those are most suitable for the all-atom MD simulations performed.

6.2.2 MD Simulations

Both systems were prepared according to our standard protocols [110]. All-atom, explicit solvent MD simulations were performed at 37°C and neutral pH using *in lucem* molecular mechanics (*il*mm) (Beck et al., 2000-2014). The NVE microcanonical ensemble (constant number of particles, volume, and energy) was used with periodic boundary conditions, and the Levitt et al. force field [104]. Before running the simulations, the starting structures (Myosin + ADP + P_i + Mg^{2+}) were minimized for 1,000 steps, and flexible three-center (F3C) water molecules [112] were added to a rectangular box. The solvent density of the box was adjusted to 0.99336 g/ml, the experimentally determined density for that temperature [113]. A time step of 2 femtoseconds (fs) was used, and after each picosecond (ps), a structure was saved for analysis. An 8 Å force-shifted cutoff was employed for non-bonded interactions [114]. Three simulations of WT Myosin + ADP + P_i + Mg^{2+} and three simulations of R397Q Myosin + ADP + P_i + Mg^{2+} were performed for 50 ns each.

6.2.3 MD Analysis

All analyses of MD trajectories were performed using *il*mm unless otherwise indicated [111]. Contacts between non-sequential atoms were classified as in contact if two carbon atoms were separated by less than 5.4 Å, or if two non-carbon atoms were separated by less than 4.6 Å. They were further classified as hydrophobic if they were between two carbon atoms less than 5.4 Å apart and each carbon was bound to at least one hydrogen atom. Contacts were considered hydrogen bonded if there was a donor (D-H) and acceptor (A) atom that were within 2.6 Å of each other and where the D-H-A angle was between 45° and 135°. Lastly, contacts were defined as 'other' if there were two heavy atoms within 4.6 Å of each other and did not fit in either of the other two classifications. Distances were measured between specific atom pairs. Solvent accessible surface area (SASA) was calculated using the Lee and Richards algorithm [115]. Protein images were generated using the UCSF Chimera package from the

Computer Graphics Laboratory, University of California, San Francisco (supported by NIH P41 RR-01081) [116] unless otherwise indicated.

6.3 Results

Three simulations with ADP, Pi, and Mg^{2+} bound to WT myosin and three simulations with ADP, Pi, and Mg^{2+} bound to R397Q myosin were performed. These simulations are referred to as WT and R397Q or mutant simulations throughout this chapter. Each simulation was 50 ns long, and was performed at 37°C and neutral pH. Unless otherwise indicated, values provided below are averages of all three simulations of a given condition over the last 30 ns of simulation time. Error values given are the standard deviations between simulations.

6.3.1 Contact analysis of residue 397

In order to assess if the R397Q mutation disrupted intramolecular contacts around residue 397, we specifically examined contacts that involved both 397 and neighboring residues in mutant and WT simulations using ContactWalker [156]. In mutant simulations, Gln397 gains contact time with Lys391 (86 ± 5% mutant vs. 12 ± 15% WT Arg397- Lys391) and loses contact with Asp595 (12 ± 9% mutant vs. 100 ± 0% WT Arg397 – Asp595). Neighboring residue Pro396 also undergoes significant contact changes as well. In mutant simulations it loses contact with reside Gln593 (11 ± 9% mutant vs. 88 ± 8% WT) and gains contact with residue His408 (76 ± 3% mutant vs. 23 ± 2% WT) (Figure 6.1). Note all of these percentages include the entire 50 ns simulation time.

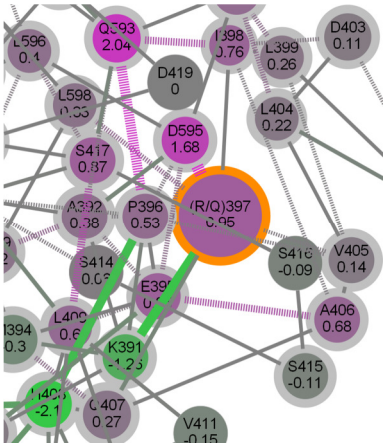

Figure 6.1. Contact walker assessments of R397Q mutant simulations vs. WT. Mutant site shown in Magenta with orange border. Magenta dashes show contacts lost in mutant vs. WT and green lines show contacts gained. Numbers show the minimum contact difference between all mutant and all WT simulations. Residue 397 and 396

6.3.2 Effects of R397Q on the actin binding surface of myosin

The contact changes described above reflect mutation-induced alterations the contact network in parts of the actin binding surface. To further assess the effects of the mutation on these residues, we performed root-mean-squared deviation (RMSD) analysis of the Cα atoms of the actin binding surface. The actin binding residues were also used in the alignment for the RMSD calculation, and as such this measurement reflects local conformation of the actin binding sites. Interestingly, despite the alterations

to the contact network on the actin binding surface described above, the local conformation did not differ between the WT and R397Q simulations (4.4 ± 0.7 Å vs. 4.5 ± 0.1 Å).

The contacts between residues 396-593 and especially 397-595 stabilize the position of the M Loop (residues 396-410) (Figure 6.2 A, Top). In all of the mutant simulations, this loop (which contains the mutation) loses contact between these two critical pairs, and pulls away. In two out of three mutant simulations, the native β-sheet secondary structure that this actin binding loop adopts is lost and instead the M loop adopts a non-native α-sheet secondary structure (Figure 6.2). In mutant simulation 2, the native β-sheet is lost around ~19 ns and transitions to α-sheet by ~38 ns. In mutant simulation 3, the transition happens more quickly; the β-sheet is lost around ~12 ns and α-sheet is formed ~25 ns (Figure 6.2 B). The beta strands in mutant simulation 1 tend to fray on the ends slightly more than those in the WT simulations, but it never transitions out of the native β-sheet structure. Figure 6.2 shows an example structure from mutant simulation 3 M Loop before and after conversion to α-sheet vs. WT myosin simulation 3, which has stable native β-sheet throughout (A, bottom) and plots of M Loop secondary structure for all size simulations (B).

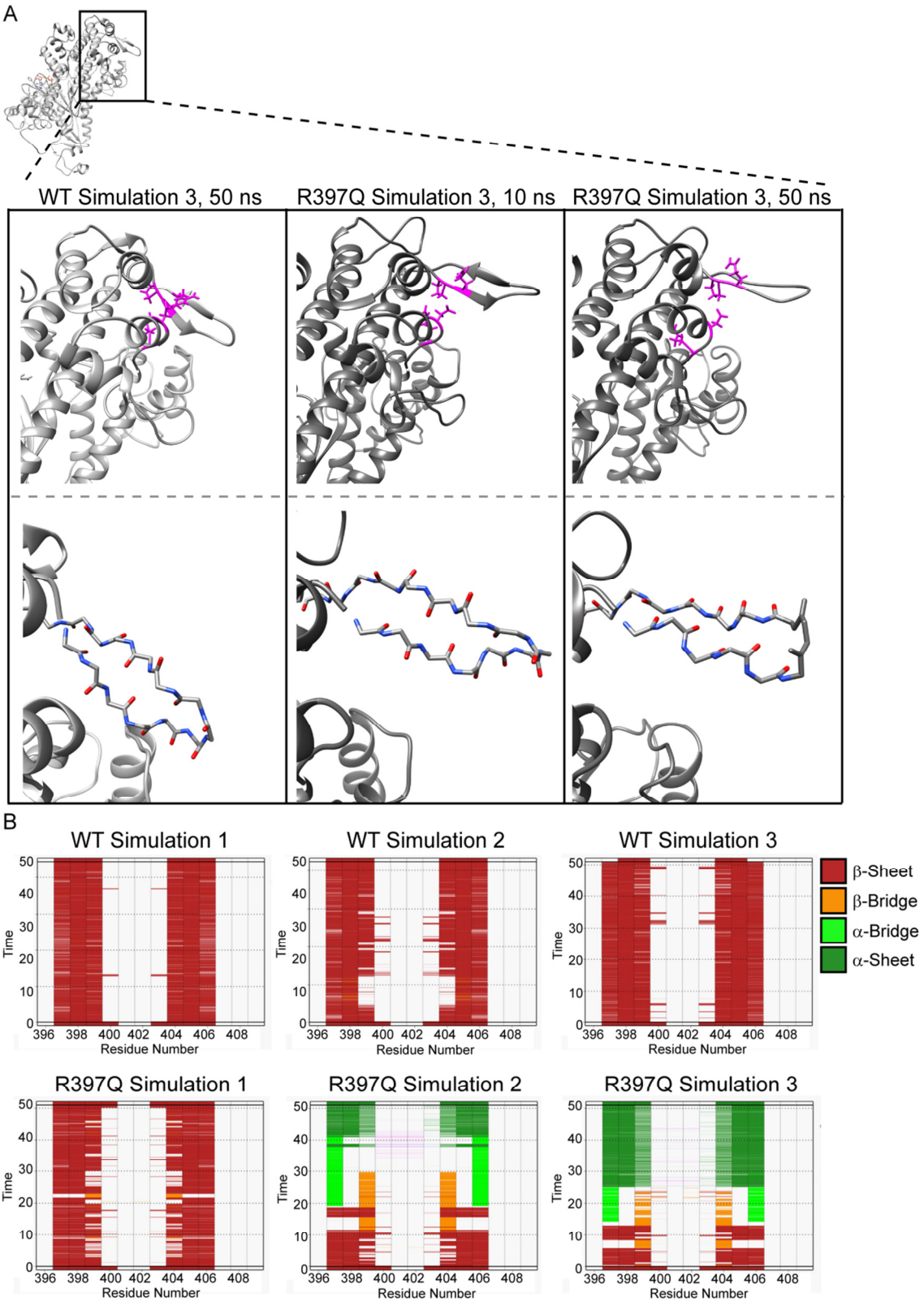

Figure 6.2. Assessment of M Loop contacts and secondary structure. (A) Contacts that are broken in mutant simulations are shown in magenta. Breakage of these contacts is associated with movement of the M Loop away from the rest of myosin. (B) Converson of M Loop to α-sheet. (C) DSSP assessment of secondary structure for each simulation over time. R397Q simulations 2 and 3 convert to α-sheet.

A further assessment of the actin binding surface was carried out to determine if, in addition to these contact changes and secondary structure alterations, R397Q altered the charge exposure on the actin binding surface. The initial interaction between actin and myosin in the pre-powerstroke state is primarily electrostatic in nature [102, 137–139], and the rate of attachment and ATPase activity can be dramatically affected by the positive charges presented on myosin's actin binding surface [139–141]. Loop 2, in particular, is known to be critical in the early electrostatic interaction between actin and myosin. The charge density on Loop 2 has been shown to mediate ATPase activity [139–141]. We were, therefore, interested in whether the mutation on the actin binding surface altered the exposure of polar residues on the actin binding (and loop 2 in particular) surface that could affect the early-stage acto-myosin interaction.

In dADP simulations (Section 5.3.3), Loop 2 polar SASA was increased relative to WT ADP simulations (315.3 ± 21.3 $Å^2$ dADP vs. 270.8 ± 26.2 $Å^2$ ADP). We predicted that this increase in polar residue exposure would result in increased acto-myosin interaction vs. WT ADP. *In vitro* motility experiments at high ionic strength validated this prediction. High ionic strength solutions are typically not used for *in vitro* motility experiments because the charged solution interrupts the acto-myosin electrostatic interaction resulting in dissociation of actin and loss of movement [139, 143]. In the experiments we performed at a variety of ionic strengths, we observed an increased number of moving filaments with dADP vs. ADP, at all ionic strengths, but this effect is particularly noticeable at 150 mM where more than three times as many actin filaments were moving with dATP than with ATP (Figure 5.11).

Similar to the effect that dADP had on the actin binding surface (Section 5.3.3), R397Q resulted in an increase in the exposure of Loop 2 polar residues vs. WT (288 ± 2.6 $Å^2$ vs. 270.8 ± 26.2 $Å^2$ for mutant vs. WT) (Figure 6.3 A). The effect of dADP was greater than that of R397Q (315.3 ± 21.3 vs. 288 ± 2.6 for dADP vs. R397Q) suggesting that dADP may have a more profound effect on actin binding than R397Q vs. WT (ADP). Nonetheless, the intermediary value of increased polar SASA of Loop 2 suggests that R397Q may increase electrostatic interactions between actin and myosin. Inspection of the distribution of structures adopting conformations with higher Loop 2 polar SASA demonstrates that R397Q stabilized the actin binding site relative to WT (and dADP). A histogram of Loop 2 polar residue SASA shows that the R397Q simulations have a more narrow distribution that is right shifted versus WT; there are few instances of this SASA value going below 250 $Å^2$ (4% of R397Q vs. 16% of WT), and many more instances of values over 270 $Å^2$ (82% of R397Q vs. 70% of WT) (Figure 6.3 B). Figure 6.3 C further highlights this

shift in the distribution of structures favoring increased polar SASA in dADP vs. ADP simulations, however this effect is not as dramatic as what was observed with dADP in Figure 5.9.. .Both the increased frequency in states with higher Loop 2 polar SASA values and the narrower distribution highlight that R397Q stabilizes a conformation with increased Loop 2 polar SASA, which is a conformation that has a higher actin-binding propensity than WT myosin (demonstrated with dADP simulations and experiments).

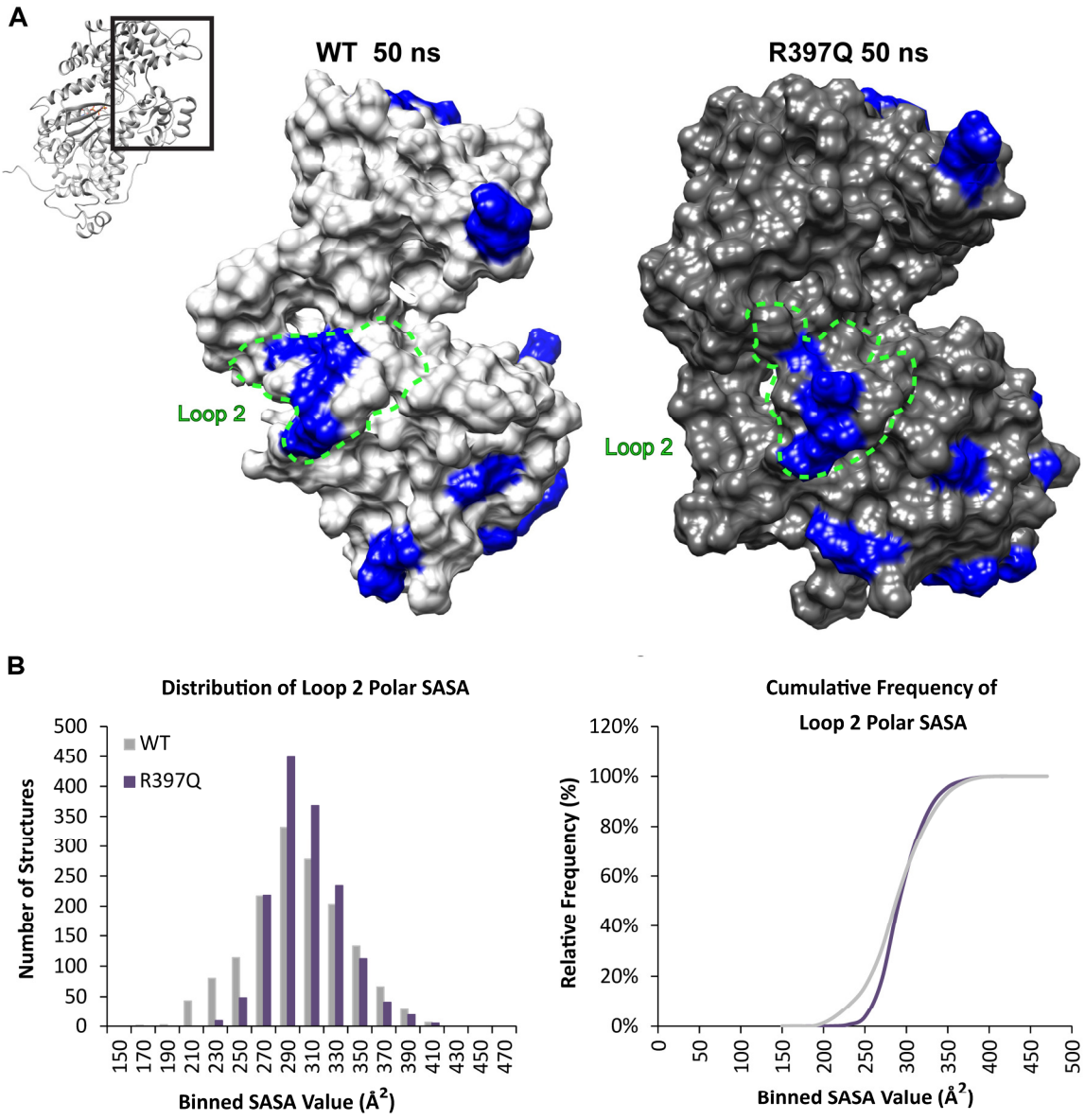

Figure 6.3. Assessment of R397Q-induced alterations to the actin binding surface. (A) Representative actin binding surface structures at 50 ns from WT and R397Q simulations. For reference, the entire S1 is shown where the boxed region indicates the region that is shown with a surface rendering. Blue highlight indicates positively charged residues. These residues are more exposed to the solvent in the R397Q simulations. (B) 100 ps granularity data used to populate histogram, which highlights the right shift of the distribution of Loop 2 polar SASA values in R397Q simulations. (C) This effect is further evidenced by the cumulative frequency plot that demonstrates at any SASA value observed, there is a higher fraction of R397Q structures that have higher SASA values than WT structures. The effect of R397Q on Loop 2 polar SASA is less dramatic than that of dADP.

6.3.3 Effects of R397Q on the cleft conformation

The extent to which the actin binding cleft is open vs. closed is thought to predict whether myosin binding to actin is energetically favorable. Open-cleft conformations of myosin bind to actin endothermically in contrast to closed-cleft conformations of myosin, which can bind exothermically [134]. Using the same methods that we used to assess cleft openness in dADP vs. WT ADP simulations, we measured the angle between the helices bordering the cleft on the lower 50k domain (w-helix, residues 630-646) and the upper 50k domain (HO helix, residues 411-442). The helices and vectors used to measure this angle are shown from two different views in Figure 5.7 A and shown again here in Figure 6.4 A. The cleft angle measurements demonstrate that R397Q stabilized a closed cleft conformation of myosin and specifically highlights the closure of the outer cleft (the portion closest to the actin binding site) (Figure 6.4 B). This R397Q-induced stabilization of the cleft relative to WT is very similar to the dADP-induced alterations discussed in section 5.3.2.

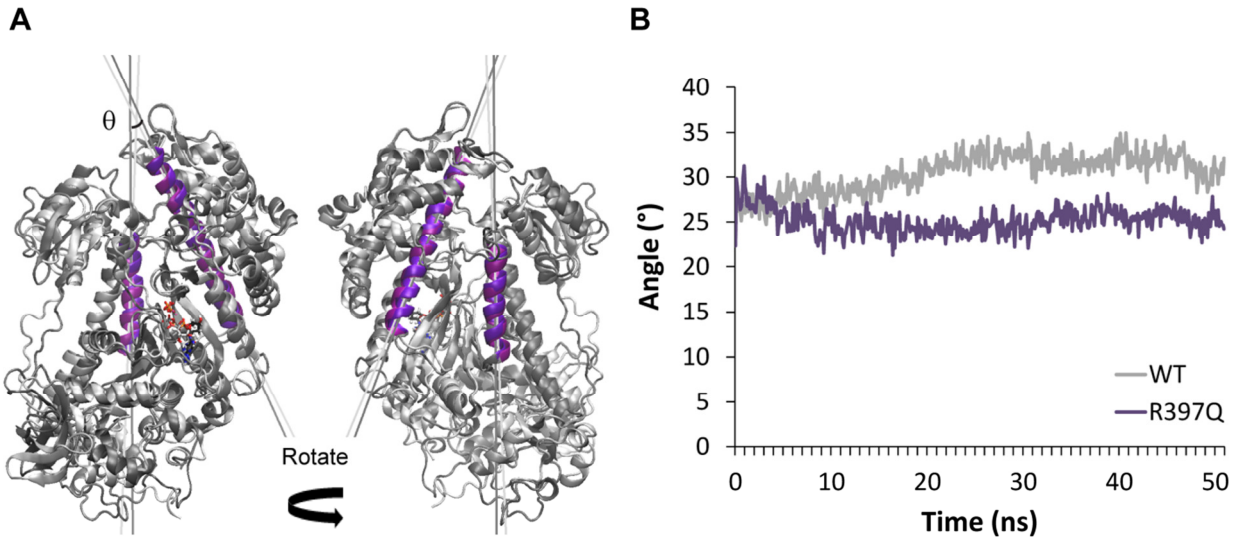

Figure 6.4. Cleft angle quantification using helix-helix method. Assessment of the cleft angle by calculating the angle between the two vectors shown in fit through the helices colored purple (A). (B) Quantitative data shown in plot for 50ns of simulation time. The two sets of simulations diverge almost immediately and highlight that R397Q stabilizes a closed cleft conformation.

As was discussed in Chapter 5, the cleft angle is inversely related to Loop 2 polar SASA. This is observed again in this data set, where the stably closed cleft angle in the mutant simulations is concomitant with a narrow, stable distribution of high Loop 2 polar SASA values, discussed above.

We also assessed the cleft conformation in R397Q simulations by calculating the distances between residues on the inner (inner cleft, residues 277-465; far inner cleft, residues 232-461) and outer (outer cleft, residues 416-589; far outer, residues 365-536) portions of the cleft that have been previously used to assess cleft closure across different species of myosin and in different states of the cross-bridge cycle (Figure 5.8 A and Figure 6.5 A) [135]. This analysis supports the data observed using the cleft angle analysis, and is again similar to what was observed in dADP simulations. The R397Q mutation stabilized a closed outer cleft (416-589 and 365-536 were closer together in mutant vs. WT simulations) however, the inner cleft was more open in mutant vs. WT simulations (Figure 6.5 B). These alterations were less dramatic than what was observed in dADP simulations, but similar to the conclusions discussed in section 5.3.2, these measurements suggest that R397Q stabilizes a conformation of myosin with a closed cleft and increased exposure of polar residues in Loop 2 relative to WT myosin. In Figure 6.5 C, R397Q myosin is shown aligned to WT (ADP) myosin and WT (dADP) myosin to enable comparisons of the binding pocket, switch regions, and inner cleft residue distances. As evidenced by Figure 6.5 B,C the opening of the inner cleft relative to WT myosin suggests that the nucleotide binding pocket may be more open in R397Q simulations than in WT simulations.

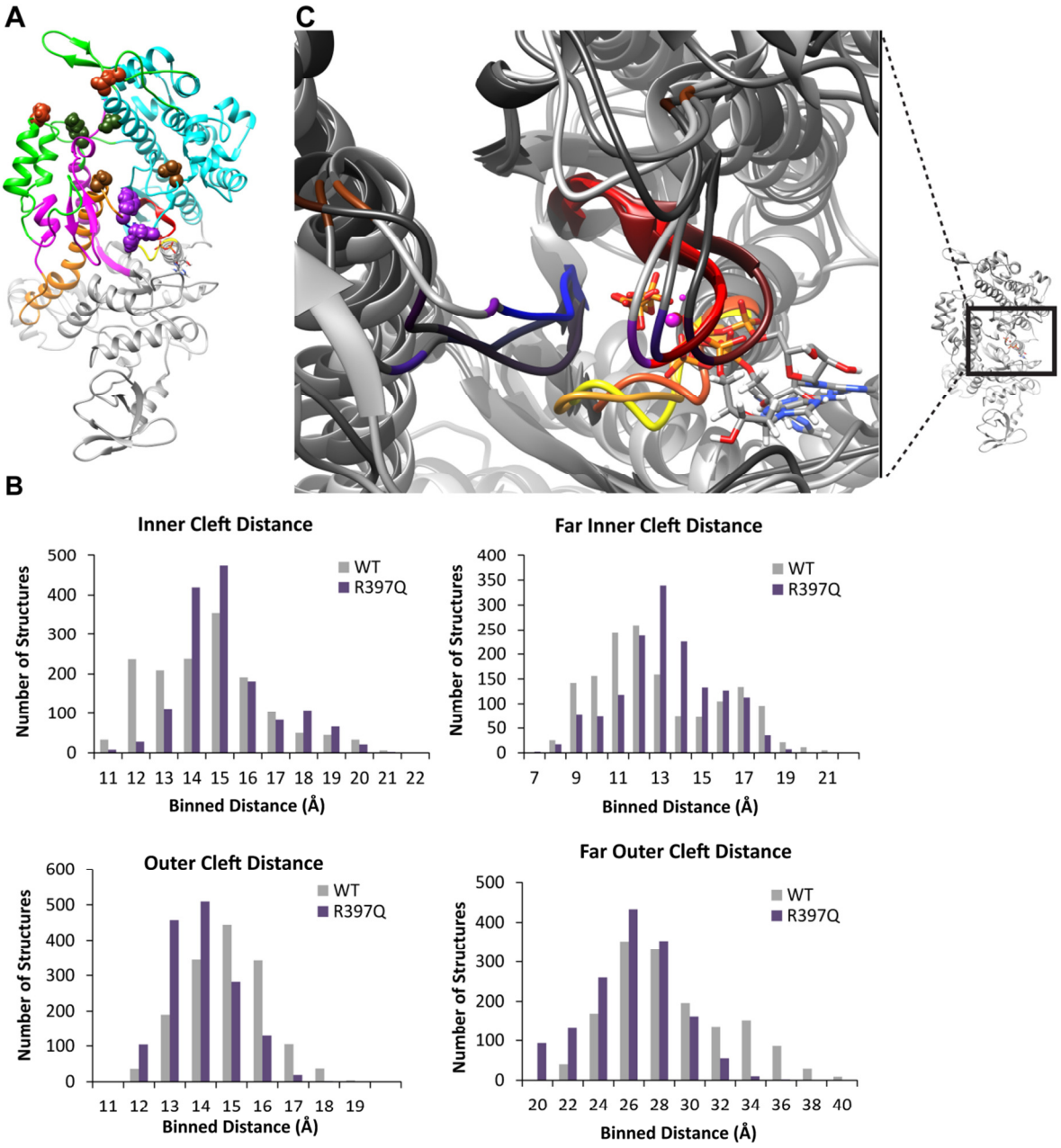

Figure 6.5. Cleft conformation analysis using residue-residue distance in mutant vs. WT simulations. Representative structure highlights the residues used in this analysis (shown as spheres) (A). Histogram of structures taken at 100 ps resolution highlight the structures from R397Q simulations populate a more closed-cleft (residues closer together) state , while inner cleft measurements are further apart (B). Representative 50ns structures highlight the movement of residues on the lower 50k region, 461 (purple) and 465 (brown), away from their partner on the upper 50k region, 232 (purple) and 277 (brown), in R397Q vs. dADP simulations vs. ADP simulations. ADP structure and colors are the lightest shades, dADP structures and colors are the middle shades, and R397Q structure and colors are the darkest shades. Reference structure is shown with detail region shown in boxed region (C).

6.3.4 Effects of R397Q on the nucleotide binding pocket

In order to further assess R397Q-induced alterations to the binding pocket, we calculated the number of contacts made between myosin and the nucleotide. Myosin loses contacts with ADP in the mutant simulations (Figure 6.6 A), which is reminiscent of what was observed in the binding pocket of dADP simulations. The extent of contact loss and the residues that underwent contact loss are similar in R397Q and dADP simulations vs. WT ADP. In particular, contacts are lost between ADP and residue Tyr135 (3% mutant vs. 81% WT and 26% dADP), Asn188 (6% mutant vs. 76% WT and 5% dADP), and Lys191 (10% mutant vs. 91% WT and 21% dADP) (Figure 6.6 B).

Additional contact analysis of interactions between the switch regions of myosin and Pi and Mg^{2+} show that there was a loss of contact between residues that have been shown to be critical in maintaining a "closed" binding pocket (Section 5.3.1) [55, 126–

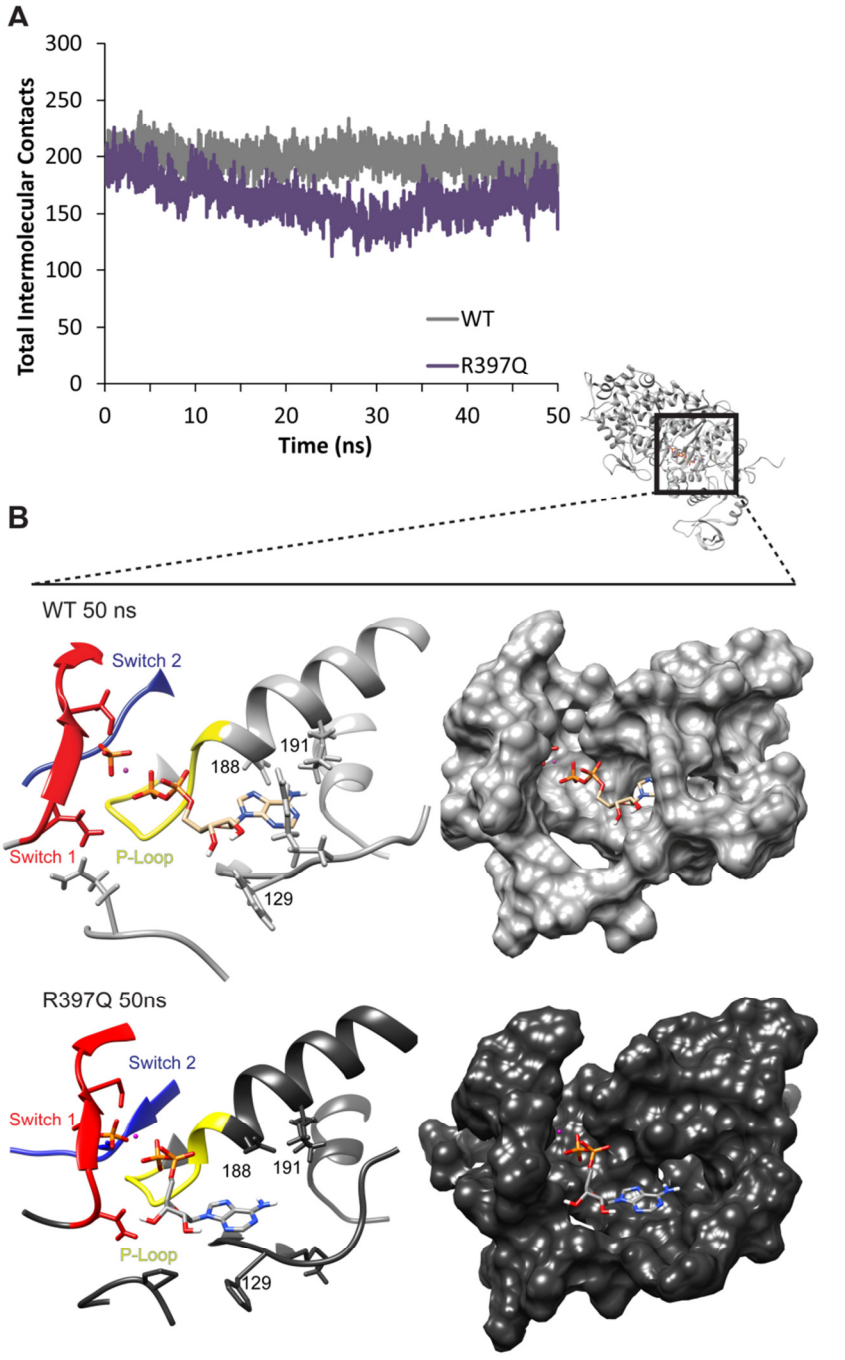

Figure 6.6. Effects of R397Q on the nucleotide binding pocket. The nucleotide binding pocket conformation is allosterically altered in R397Q simulations. (A) Total number of contacts made between myosin and the nucleotide, Pi, and Mg^{2+} averaged over the three simulations for each condition. (B) Ribbon diagram and surface renderings of representative binding pocket structures highlighting the conformational differences between the binding pocket in the R397Q (dark grey) and WT (light grey) simulations. Small myosin structure shows region of focus.

130, 132, 133]. The conformation of SW1 is largely dictated by its interaction with the nucleotide and influences myosin's interaction with actin, where the "open" conformation of SW1 binds actin more tightly than the "closed" conformation of SW1 [55, 129, 130]. SW1 is defined as "open" when Ser237 does not interact with the Mg^{2+} ion [126]. The Gly457 (SW2 residue) interaction with Pi is necessary for ATPase activity, and it is lost in the strong actin binding state when SW2 is in the "open" position [55, 126–128, 132, 133]. The orientation of the switch regions relative to the nucleotide for R397Q simulations, WT (dADP) simulations, and WT (ADP) simulations can be seen in Figure 6.5.

Contacts between Asn233-Pi (16% mutant vs. 39% WT) and between Gly457 (Switch 2)-Pi (9% mutant vs. 67% WT) were lost in all three mutant simulations. Contacts between Ser456 (Switch 2)-Pi and Ser237 (Switch 1)-Mg^{2+} were lost in mutant simulations 1, 2 (10% mutant 1,2 vs. 71% WT and 20% mutant 1,2 vs. 100% WT, respectively). Mutant simulation 3 maintained these contacts for 100% and 95% of the simulation time. These changes are similar to what was observed with dADP, although they occur to a lesser extent in R397Q simulations. The one exception is with the contact between Asn233 and ADP (switch 1-ADP), which was maintained in the mutant simulations and not in the dADP simulations. This loss of intermolecular contacts involving the switch regions is attributable to increased distance between the switch regions and the nucleotide, Pi, and Mg^{2+}. The center of mass of PB (phosphorous that is furthest away from adenine) moves away from the switch regions; the movement away from SW1 is more subtle than that of dADP, however, the movement away from SW2 is dramatic and comparable to what was observed in the dADP simulations.

Together, the movement of the nucleotide and the loss of key contacts between the nucleotide, PI, and Mg^{2+} demonstrate that the binding pocket favors an "open" conformation with the R397Q mutation. This can be seen in by examining the ribbon diagram and surface rendering of the binding pocket (Figure 6.6 B).

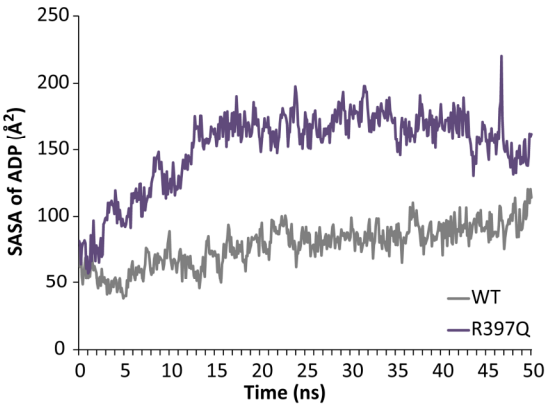

Figure 6.7. ADP SASA for WT vs. mutant myosin. Quantification of the exposure of the nucleotide to the solvent. Loss of contact between myosin and ADP in mutant simulations results in increased ADP SASA.

These alterations also manifest in the overall mobility of the nucleotide. The RMSD of ADP in mutant simulations is higher than ADP in WT simulations (5.0 ± 0.8 Å vs. 3.3 ± 1.2 Å, mutant vs. WT). The RMSD of dADP in the binding

pocket was 5.1 ± 0.7 Å, again demonstrating the similarities between the R397Q simulations and dADP simulations. The openness of the binding pocket also resulted in increased SASA of ADP in mutant simulations compared to WT (166.7 ± 40.7 $Å^2$ vs. 88.1 ± 22.6 $Å^2$, respectively) (Figure 6.7). For comparison, the SASA of dADP was 153.6 ± 6.03 $Å^2$.

6.4 Discussion

The R397Q simulations demonstrate that there are similar alterations to myosin induced by the R397Q mutation as induced by dADP binding to the binding pocket, which is particularly interesting because these two perturbations are in completely different areas of the protein. By most metrics, the magnitude of change is less with the mutant than with dADP (with the exception of intermolecular contacts lost, the RMSD of the nucleotide, and nucleotide SASA in the binding pocket), but the relationship between the mutant and dADP simulations versus WT (ADP) simulations is very similar. These findings are interesting because R397Q leads to severe HCM in humans (characterized by lower force per contraction), and dADP has a therapeutic effect that results in increased force per contraction. Furthermore, it is interesting that similar changes are observed with perturbations to the binding pocket (dADP) vs. the actin binding surface (mutant).

The simulations presented here predict that R397Q myosin binds actin more favorably than wild-type (although likely not as favorably as dADP-bound myosin), which would lead to faster rate of force development. There is experimental evidence that supports this hypothesis. In particular the kinetic analysis performed by Pogessi's group [29]. Here, they used affected human tissue samples and looked at myofibrilar kinetics. They showed faster rate of force development and faster relaxation with the mutant (but lower force) vs. WT. The difference between the physiological effects of R397Q (R403Q in humans) and dADP may, therefore, lie in the relationship between the rate of cross-bridge attachment and the rate of cross-bridge detachment. Based on the two state cross-bridge model (introduced in Section 1.3.2), we can state that force is proportional to $1/(1+(f_{app}/g_{app}))$ where f_{app} is the apparent rate of cross-bridge attachment and g_{app} is the apparent rate of crossbridge detachment. If, therefore, a perturbation to the system increases f_{app} more than g_{app}, we would predict and overall increase in force from the perturbation. If, on the other hand, a perturbation increased gap more than f_{app}, we would predict an overall decrease in force from that perturbation. The data from MD simulations of pre-powerstroke myosin predict that f_{app} is the highest in the dADP system, followed by R397Q, followed by WT (ADP). Physiological studies suggest that gap is the highest in the R397Q system, followed by WT

(ADP), followed by dADP-bound myosin (unpublished data). Therefore, relative to WT (ADP) R397Q increases f_{app} and g_{app} but $g_{app} > f_{app}$ predicting a decrease in force vs. WT. dADP, on the other hand, increases f_{app} but has less of an effect on g_{app}, so $f_{app} >> g_{app}$ predicting an increase in force vs. WT (ADP). While these simulations are of the pre-powerstroke conformation and do not have actin in the simulation, the binding pocket is so open in the R397Q simulations that it could indicate ADP release would be faster, which further supports this hypothesis.

CHAPTER 7. CONCLUSIONS AND FUTURE DIRECTIONS

7.1 Summary and Conclusions

The research presented in this dissertation is focused on characterizing a novel, myo-filament targeted inotrope, 2 deoxy-ATP. The primary goals of this research were to (1) to characterize the effects of increased dATP *in vivo* on cardiac function in both normal hearts and those following injury (myocardial infarction), and (2) to determine the effects of dATP binding on the structure of myosin in order to elucidate a molecular mechanism by which increased dATP concentration results in contractile enhancements. This work combined *in vitro, ex vivo,* and *in vivo* assessments of cardiac function with molecular dynamics simulations to better understand the therapeutic potential of dATP as well as its mechanism of action.

Overexpression of Ribonucleotide reductase (RR), the enzyme that catalyzes the production of deoxy nucleotides, was our approach to increase [dATP] *in vivo.* Three animal models were used to study the effects of elevated [dATP] on cardiac function and cardiac tissue morphology. First, we characterized a transgenic mouse model that had ubiquitous overexpression of RR from birth. This was the first animal model of RR overexpression. Thus, we sought to determine whether the functional effects of dATP that we observed *in vitro* were present *in vivo,* whether they persisted into adulthood, and whether there was any compensation associated with long-term elevation in [dATP]. Additionally, even though this was not a therapeutic model, we used this long-term expression model to determine whether there were pathological consequences (in particular on myocardial energetics) associated with elevated [dATP]. The results from this study confirmed that overexpression of RR *in vivo* resulted in significant improvements in basal cardiac function, *in vivo, ex vivo,* and *in vitro.* These results were consistent with predictions made based on our previous biochemical studies *in vitro.* This increase in cardiac performance occurred without pathological effets on myocardial energetics, or on myocardial morphology. There was no evidence of alteration to cell size, shape, or orientation, there was no change in the ratio of α- to β -myosin and there was no upregulation of ANP or BNP. These results motivated us to pursue the development of a therapeutically viable approach to elevate RR *in vivo.*

In order to achieve overexpression of RR *in vivo,* we developed an adeno-associated virus with a caradic-specific promoter that carried the human sequence for both RR subunits. In an initial study where we treated healthy mice with this virus, we sought to characterize its distribution and effect on levels of RR in the heart. Furthermore, we aimed to determine whether this gene therapy approach could increase

cardiac performance in healthy mice. While we did not observe an increase in cardiac function via echocardiography *in vivo,* we did observe a significant improvement in basal cardiac function *ex vivo*, with an increased LVDevP, and positive rate of pressure development. We determined that there were significant viral genomes present in the heart and in the liver, however, there was only overexpression of RR in the hearts of treated animals. This result confirms the efficacy of the cardiac-specific promoter in the AAV6-RR virus. We also assessed overall tissue morphology and did not observe any negative morphological consequences of treatment with AAV6-RR. This was the first study using a virus to overexpress RR *in vivo* and demonstrated that we could achieve cardiac-specific overexpression of RR and an elevation of cardiac function in adult animals treated with AAV6-RR. These data motivated us to determine whether treatment with AAV6-RR could improve cardiac function following myocardial infarction.

We administered treatment to animals four weeks following myocardial infarction and followed them via echocardiography for an additional eight weeks following treatment. Comparing mean fractional shortening values between groups did not show any significant effect of treatment, however we propose that this is largely attributable to the extremely high variability in function within each group. A repeated measures t-test was used to compare animals pre-treatment and post-treatment, effectively using each animal as its own control. By this measure, the RR-treated animals improved 4 weeks following treatment (on average, 24% improvement) vs. control (on average, 3% improvement). This difference was not significant at the final endpoint (17% improvement for RR-treated vs. 6% improvement for control animals). Ultimately, due to the large variability in cardiac function with each group, which was exacerbated by the infarct surgery, this study was underpowered. While there is evidence that treatment with AAV-RR may improve cardiac function following MI, a follow-on study must be performed to increase the number of animals in each group

In order to determine the mechanism by which dATP increases force, we performed molecular dynamics simulations of myosin in the pre-powerstroke state to study the effects of dADP.Pi (hydrolysis products of dATP) on the structure and dynamics of myosin. These simulations demonstrated that the removal of a single oxygen had profound effects on the conformation of myosin. Myosin lost contacts with dADP.Pi early on in the simulations, which was a result of movement of the nucleotide and switch regions away from each other. Some of the contacts lost are critical for the maintenance of a closed nucleotide binding pocket, indicating that dADP stabilizes pre-powerstroke myosin in a conformation with the

switch regions more open, and the nucleotide more exposed to the solvent. These changes were associated with the stabilization of a closed cleft in the dADP simulations, which is associated with strong actin binding. In the ADP simulations, on the other hand, the actin binding cleft opened over time. The stable closed cleft conformation observed in the dADP simulation, in turn, stabilized the exposure of polar residues on the actin binding surface of Loop 2. These residues are important in mediating early, electrostatic interactions with actin. In the ADP simulation these residues are less exposed, which is correlated with the opening of the cleft. Together, these data demonstrate that dADP stabilizes a conformation of myosin that has increased charge on the actin binding surface, suggesting more favorable electrostatic interaction with actin than myosin bound to ADP. This prediction was validated by *in vitro* motility experiments that showed increased numbers of moving actin filaments at high ionic strength when dATP was present. The molecular dynamics simulations provide a framework of molecular events that explain the results we have previously observed *in vitro*, as increased affinity of myosin for actin would increases the rate of cross-bridge attachment, and thus would increase force production.

In conclusion, the research in this dissertation describes the characterization of a novel myofilament-target inotrope, dATP, which acts via conformational changes to the structure and dynamics of myosin to confer increased force production without altering calcium handling. Animal models were used to characterize the efficacy of elevation of dATP *in vivo* via adeno-associated viral overexpression of RR, to study the distribution of virus, and to characterize any pathology associated with RR overexpression. This work demonstrated that AAV6-mediated overexpression of RR can increase basal cardiac performance in animals without deleterious effects on myocardial energetics, morphology, or calcium handling. Molecular dynamics simulations were used to study the mechanism by which dATP increases force production, and provided a novel molecular framework that explains a potential mechanism for the increased rate of cross-bridge attachment observed when myosin uses dATP as an energy substrate. Together, these data provide the ground work for further clinical development of elevation of dATP as a novel myofilament-target inotrope to improve left ventricular function in patients with cardiac disease.

7.2 Future Directions

There are several future studies that could be carried out to supplement this work. As previously mentioned, additional animals should be added to the groups in the mouse infarct study. This should help mitigate the large inter-animal variability in cardiac function observed. Additionally,

characterization of the effects of elevated [dATP] could be performed on a different animal model of systolic dysfunction, such as dilated cardiomyopathy (DCM). Transgenic mice with a DCM phenotype may be more homogenous than mice post-myocardial infarction, which would also help to resolve the effects of elevated dATP *in vivo.* Follow-on characterization of myocardial tissue with elevated [dATP] could include metabolomics analysis and a study of other ATPases in cardiomyocytes. These analyses could help to explore potential off-target effecs of elevated [dATP], and may be important for future clinical development of AAV6-RR as a therapy.

Additional work could also be done with the molecular dynamics simulations. Chapter 6 details one potential avenue of future work: the study of myosin mutations that affect cross-bridge binding. Amassing a database of how different mutations alter myosin structure and function could inform us about genotype-phenotype relationships that are yet unknown. Another avenue to consider is simulating additional states of the cross-bridge cycle with ADP vs. dADP. One interesting state would be the strongly bound state, post-Pi release (Actin-Myosin-Pi). These simulations could provide details about how dADP (or mutations) alter cross-bridge detachment. These high-resolution atomic models could also be used in concert with lower-resolution models of larger time- and space- scale. For example, these simulations could inform the building of a model of a single regulatory unit. Together these models could provide deeper understanding of the mechanisms of the cross-bridge cycle.

REFERENCES

1. WHO | Fact sheet on Cardiovascular diseases (CVDs) (2012).

2. Roger VL et al. (2012) Heart disease and stroke statistics--2012 update: a report from the American Heart Association. *Circulation* 125:e2–e220.

3. Lilly LS, M.D. (2011) *Pathophysiology of Heart Disease: A Collaborative Project of Medical Students and Faculty* (Lippincott Williams & Wilkins).

4. Heidenreich PA et al. (2011) Forecasting the future of cardiovascular disease in the United States: a policy statement from the American Heart Association. *Circulation* 123:933–44.

5. Roger VL et al. (2004) Trends in heart failure incidence and survival in a community-based population. *JAMA* 292:344–50.

6. Berthiaume F, Maguire TJ, Yarmush ML (2011) Tissue engineering and regenerative medicine: history, progress, and challenges. *Annu Rev Chem Biomol Eng* 2:403–30.

7. Vunjak-Novakovic G et al. (2010) Challenges in cardiac tissue engineering. *Tissue Eng Part B Rev* 16:169–87.

8. Teerlink JR et al. (2009) Agents with inotropic properties for the management of acute heart failure syndromes. Traditional agents and beyond. *Hear Fail Rev* 14:243–253.

9. Abraham WT et al. (2005) In-hospital mortality in patients with acute decompensated heart failure requiring intravenous vasoactive medications: an analysis from the Acute Decompensated Heart Failure National Registry (ADHERE). *J Am Coll Cardiol* 46:57–64.

10. Hasenfuss G, Teerlink JR (2011) Cardiac inotropes: current agents and future directions. *Eur Hear J* 32:1838–1845.

11. Regnier M, Martyn DA, Chase PB (1998) Calcium regulation of tension redevelopment kinetics with 2-deoxy-ATP or low [ATP] in rabbit skeletal muscle. *Biophys J* 74:2005–15.

12. Regnier M, Homsher E (1998) The effect of ATP analogs on posthydrolytic and force development steps in skinned skeletal muscle fibers. *Biophys J* 74:3059–71.

13. Regnier M, Lee DM, Homsher E (1998) ATP analogs and muscle contraction: mechanics and kinetics of nucleoside triphosphate binding and hydrolysis. *Biophys J* 74:3044–58.

14. Regnier M, Rivera AJ, Chen Y, Chase PB (2000) 2-deoxy-ATP enhances contractility of rat cardiac muscle. *Circ Res* 86:1211–7.

15. Schoffstall B, Chase PB (2008) Increased intracellular [dATP] enhances cardiac contraction in embryonic chick cardiomyocytes. *J Cell Biochem* 104:2217–27.

16. Schoffstall B, Clark A, Chase PB (2006) Positive inotropic effects of low dATP/ATP ratios on mechanics and kinetics of porcine cardiac muscle. *Biophys J* 91:2216–26.

17. Smith SH, Fuchs F (2002) Length dependence of cardiac myofilament Ca(2+) sensitivity in the presence of substitute nucleoside triphosphates. *J Mol Cell Cardiol* 34:547–54.

18. Takenaka H, Ikehara M, Tonomura Y (1978) Interaction between actomyosin and 8-substituted ATP analogs. *Proc Natl Acad Sci U S A* 75:4229–33.

19. Weber A (1969) Parallel response of myofibrillar contraction and relaxation to four different nucleoside triphophates. *J Gen Physiol* 53:781–91.

20. Pate E, Nakamaye KL, Franks-Skiba K, Yount RG, Cooke R (1991) Mechanics of glycerinated muscle fibers using nonnucleoside triphosphate substrates. *Biophys J* 59:598–605.

21. Pate E, Franks-Skiba K, White H, Cooke R (1993) The use of differing nucleotides to investigate cross-bridge kinetics. *J Biol Chem* 268:10046–53.

22. White HD, Belknap B, Jiang W (1993) Kinetics of binding and hydrolysis of a series of nucleoside triphosphates by actomyosin-S1. Relationship between solution rate constants and properties of muscle fibers. *J Biol Chem* 268:10039–45.

23. Shimizu T et al. (1991) Nucleotide specificity of the enzymatic and motile activities of dynein, kinesin, and heavy meromyosin. *J Cell Biol* 112:1189–97.

24. Korte FS et al. (2011) Upregulation of cardiomyocyte ribonucleotide reductase increases intracellular 2 deoxy-ATP, contractility, and relaxation. *J Mol Cell Cardiol* 51:894–901.

25. Ylikallio E et al. (2010) Ribonucleotide reductase is not limiting for mitochondrial DNA copy number in mice. *Nucleic Acids Res* 38:8208–18.

26. Lai CM, Lai YKY, Rakoczy PE (2002) Adenovirus and adeno-associated virus vectors. *DNA Cell Biol* 21:895–913.

27. Zincarelli C, Soltys S, Rengo G, Koch WJ, Rabinowitz JE (2010) Comparative cardiac gene delivery of adeno-associated virus serotypes 1-9 reveals that AAV6 mediates the most efficient transduction in mouse heart. *Clin Transl Sci* 3:81–9.

28. Konkalmatt PR et al. (2012) Adeno-associated virus serotype 9 administered systemically after reperfusion preferentially targets cardiomyocytes in the infarct border zone with pharmacodynamics suitable for the attenuation of left ventricular remodeling. *J Gene Med* 14:609–20.

29. Belus A et al. (2008) The familial hypertrophic cardiomyopathy-associated myosin mutation R403Q accelerates tension generation and relaxation of human cardiac myofibrils. *J Physiol* 586:3639–3644.

30. Morrissey RP, Czer L, Shah PK (2011) Chronic heart failure: current evidence, challenges to therapy, and future directions. *Am J Cardiovasc Drugs* 11:153–71.

31. Overgaard CB, Dzavík V (2008) Inotropes and vasopressors: review of physiology and clinical use in cardiovascular disease. *Circulation* 118:1047–1056.

32. Birks EJ (2011) A changing trend toward destination therapy: are we treating the same patients differently? *Tex Heart Inst J* 38:552–4.

33. Douglas P, Morgan C, Lee H, Foster KR (2004) LVAD as destination therapy - the economic dilemma. *IEEE Technol Soc Mag* 23:23–27.

34. Hoover-Plow J, Gong Y (2012) Challenges for heart disease stem cell therapy. *Vasc Health Risk Manag* 8:99–113.

35. Gupta R, Losordo DW (2010) Challenges in the translation of cardiovascular cell therapy. *J Nucl Med* 51 Suppl 1:122S–127S.

36. Cleland JGF et al. (2011) The effects of the cardiac myosin activator, omecamtiv mecarbil, on cardiac function in systolic heart failure: a double-blind, placebo-controlled, crossover, dose-ranging phase 2 trial. *Lancet* 378:676–83.

37. Shen Y-T et al. (2010) Improvement of cardiac function by a cardiac Myosin activator in conscious dogs with systolic heart failure. *Circ Heart Fail* 3:522–7.

38. Locher MR, Razumova M V, Stelzer JE, Norman HS, Moss RL (2011) Effects of low-level α-myosin heavy chain expression on contractile kinetics in porcine myocardium. *Am J Physiol Heart Circ Physiol* 300:H869–78.

39. Herron TJ, Devaney EJ, Metzger JM (2008) Modulation of cardiac performance by motor protein gene transfer. *Ann N Y Acad Sci* 1123:96–104.

40. Moss RL, Razumova M, Fitzsimons DP (2004) Myosin crossbridge activation of cardiac thin filaments: implications for myocardial function in health and disease. *Circ Res* 94:1290–300.

41. Jaski BE et al. (2009) Calcium upregulation by percutaneous administration of gene therapy in cardiac disease (CUPID Trial), a first-in-human phase 1/2 clinical trial. *J Card Fail* 15:171–81.

42. Horowitz JD, Rosenson RS, McMurray JJ V, Marx N, Remme WJ (2011) Clinical Trials Update AHA Congress 2010. *Cardiovasc Drugs Ther* 25:69–76.

43. Hajjar RJ et al. (2008) Design of a phase 1/2 trial of intracoronary administration of AAV1/SERCA2a in patients with heart failure. *J Card Fail* 14:355–67.

44. Wang Y, Goldhaber JI (2004) Return of calcium: manipulating intracellular calcium to prevent cardiac pathologies. *Proc Natl Acad Sci U S A* 101:5697–8.

45. Elledge SJ, Zhou Z, Allen JB (1992) Ribonucleotide reductase: regulation, regulation, regulation. *Trends Biochem Sci* 17:119–23.

46. Brenner B (1988) Effect of Ca2+ on cross-bridge turnover kinetics in skinned single rabbit psoas fibers: implications for regulation of muscle contraction. *Proc Natl Acad Sci* 85:3265–3269.

47. Smith L, Tainter C, Regnier M, Martyn DA (2009) Cooperative cross-bridge activation of thin filaments contributes to the Frank-Starling mechanism in cardiac muscle. *Biophys J* 96:3692–702.

48. Gordon AM, Rivera AJ, Wang CK, Regnier M (2003) Cooperative activation of skeletal and cardiac muscle. *Adv Exp Med Biol* 538:371–8; discussion 378–9.

49. Regnier M et al. (2004) Cross-bridge versus thin filament contributions to the level and rate of force development in cardiac muscle. *Biophys J* 87:1815–24.

50. Adhikari BB, Regnier M, Rivera AJ, Kreutziger KL, Martyn DA (2004) Cardiac length dependence of force and force redevelopment kinetics with altered cross-bridge cycling. *Biophys J* 87:1784–94.

51. Hofmann PA, Fuchs F (1987) Evidence for a force-dependent component of calcium binding to cardiac troponin C. *Am J Physiol* 253:C541–6.

52. Van der Kamp MW, Shaw KE, Woods CJ, Mulholland AJ (2008) Biomolecular simulation and modelling: status, progress and prospects. *J R Soc Interface* 5 Suppl 3:S173–90.

53. Karplus M, McCammon JA (2002) Molecular dynamics simulations of biomolecules. *Nat Struct Biol* 9:646–52.

54. Lymn RW, Taylor EW (1971) Mechanism of adenosine triphosphate hydrolysis by actomyosin. *Biochemistry* 10:4617–24.

55. Geeves MA, Holmes KC (2005) The molecular mechanism of muscle contraction. *Adv Protein Chem* 71:161–93.

56. Rayment I et al. (1993) Three-dimensional structure of myosin subfragment-1: a molecular motor. *Science* 261:50–8.

57. Alpert NR, Mulieri LA, Warshaw D (2002) The failing human heart. *Cardiovasc Res* 54:1–10.

58. Maughan DW (2005) Kinetics and energetics of the crossbridge cycle. *Heart Fail Rev* 10:175–85.

59. Schaub MC, Hefti MA, Zuellig RA, Morano I (1998) Modulation of contractility in human cardiac hypertrophy by myosin essential light chain isoforms. *Cardiovasc Res* 37:381–404.

60. Xu X et al. (2008) Broad overexpression of ribonucleotide reductase genes in mice specifically induces lung neoplasms. *Cancer Res* 68:2652–60.

61. Ogut O, Brozovich F V (2000) Determinants of the contractile properties in the embryonic chicken gizzard and aorta. *Am J Physiol Cell Physiol* 279:C1722–32.

62. Karagiannis P, Babu GJ, Periasamy M, Brozovich F V (2003) The smooth muscle myosin seven amino acid heavy chain insert's kinetic role in the crossbridge cycle for mouse bladder. *J Physiol* 547:463–73.

63. Karagiannis P, Babu GJ, Periasamy M, Brozovich F V (2004) Myosin heavy chain isoform expression regulates shortening velocity in smooth muscle: studies using an SMB KO mouse line. *J Muscle Res Cell Motil* 25:149–58.

64. Rhee AY, Ogut O, Brozovich F V (2006) Nonmuscle myosin, force maintenance, and the tonic contractile phenotype in smooth muscle. *Pflugers Arch* 452:766–74.

65. Kolwicz SC, Tian R (2010) Assessment of cardiac function and energetics in isolated mouse hearts using 31P NMR spectroscopy. *J Vis Exp*.

66. Luptak I et al. (2007) Long-term effects of increased glucose entry on mouse hearts during normal aging and ischemic stress. *Circulation* 116:901–9.

67. Yan J et al. (2009) Increased glucose uptake and oxidation in mouse hearts prevent high fatty acid oxidation but cause cardiac dysfunction in diet-induced obesity. *Circulation* 119:2818–28.

68. Liu Y et al. (2012) Transcription factor CHF1/Hey2 regulates EC coupling and heart failure in mice through regulation of FKBP12.6. *Am J Physiol Heart Circ Physiol* 302:H1860–70.

69. Bottomley PA et al. (2009) Reduced myocardial creatine kinase flux in human myocardial infarction: an in vivo phosphorus magnetic resonance spectroscopy study. *Circulation* 119:1918–24.

70. Gupta A, Chacko VP, Schär M, Akki A, Weiss RG (2011) Impaired ATP kinetics in failing in vivo mouse heart. *Circ Cardiovasc Imaging* 4:42–50.

71. Liao R, Nascimben L, Friedrich J, Gwathmey JK, Ingwall JS (1996) Decreased Energy Reserve in an Animal Model of Dilated Cardiomyopathy : Relationship to Contractile Performance. *Circ Res* 78:893–902.

72. Homsher E, Lacktis J, Regnier M (1997) Strain-dependent modulation of phosphate transients in rabbit skeletal muscle fibers. *Biophys J* 72:1780–91.

73. Millar NC, Homsher E (1992) Kinetics of force generation and phosphate release in skinned rabbit soleus muscle fibers. *Am J Physiol* 262:C1239–45.

74. Tesi C, Colomo F, Piroddi N, Poggesi C (2002) Characterization of the cross-bridge force-generating step using inorganic phosphate and BDM in myofibrils from rabbit skeletal muscles. *J Physiol* 541:187–99.

75. Bers DM (2000) Calcium Fluxes Involved in Control of Cardiac Myocyte Contraction. *Circ Res* 87:275–281.

76. Herron TJ, McDonald KS (2002) Small amounts of alpha-myosin heavy chain isoform expression significantly increase power output of rat cardiac myocyte fragments. *Circ Res* 90:1150–2.

77. Martyn DA, Regnier M, Xu D, Gordon AM (2001) Ca2+ - and cross-bridge-dependent changes in N- and C-terminal structure of troponin C in rat cardiac muscle. *Biophys J* 80:360–70.

78. Wang YP, Fuchs F (1995) Osmotic compression of skinned cardiac and skeletal muscle bundles: effects on force generation, Ca2+ sensitivity and Ca2+ binding. *J Mol Cell Cardiol* 27:1235–44.

79. Tanner BCW, Daniel TL, Regnier M (2007) Sarcomere lattice geometry influences cooperative myosin binding in muscle. *PLoS Comput Biol* 3:e115.

80. Trumble WR, Sutko JL, Reeves JP (1981) Cardiac sarcolemmal and sarcoplasmic reticulum membrane vesicles exhibit distinctive (Ca-Mg)-ATPase substrate specificities. *J Biol Chem* 256:7101–4.

81. WHO (2011) *WHO | Global atlas on cardiovascular disease prevention and control* (World Health Organization).

82. Connolly JB (2002) Lentiviruses in gene therapy clinical research. *Gene Ther* 9:1730–4.

83. Odom GL, Gregorevic P, Chamberlain JS (2007) Viral-mediated gene therapy for the muscular dystrophies: successes, limitations and recent advances. *Biochim Biophys Acta* 1772:243–62.

84. Lai CM, Lai YKY, Rakoczy PE (2002) Adenovirus and adeno-associated virus vectors. *DNA Cell Biol* 21:895–913.

85. Jooss K, Chirmule N (2003) Immunity to adenovirus and adeno-associated viral vectors: implications for gene therapy. *Gene Ther* 10:955–63.

86. Xiaolan C et al. (2011) Human Cardiac Troponin T Regulatory Cassettes Facilitate High-Level Transient Expression in Differentiating Skeletal Muscle and Continuous Expression in Cardiac Muscle. *Mol Ther* 19:S1–S332.

87. Halbert CL, Allen JM, Miller AD (2001) Adeno-associated virus type 6 (AAV6) vectors mediate efficient transduction of airway epithelial cells in mouse lungs compared to that of AAV2 vectors. *J Virol* 75:6615–24.

88. Blankinship MJ et al. (2004) Efficient transduction of skeletal muscle using vectors based on adeno-associated virus serotype 6. *Mol Ther* 10:671–8.

89. Gregorevic P et al. (2004) Systemic delivery of genes to striated muscles using adeno-associated viral vectors. *Nat Med* 10:828–34.

90. Garbern JC, Minami E, Stayton PS, Murry CE (2011) Delivery of basic fibroblast growth factor with a pH-responsive, injectable hydrogel to improve angiogenesis in infarcted myocardium. *Biomaterials* 32:2407–16.

91. Fernandes S et al. (2010) Human embryonic stem cell-derived cardiomyocytes engraft but do not alter cardiac remodeling after chronic infarction in rats. *J Mol Cell Cardiol* 49:941–9.

92. Nowakowski SG et al. (2013) Transgenic overexpression of ribonucleotide reductase improves cardiac performance. *Proc Natl Acad Sci U S A* 110:6187–92.

93. Donnelly ML et al. (2001) Analysis of the aphthovirus 2A/2B polyprotein "cleavage" mechanism indicates not a proteolytic reaction, but a novel translational effect: a putative ribosomal "skip". *J Gen Virol* 82:1013–25.

94. Donnelly ML et al. (2001) The "cleavage" activities of foot-and-mouth disease virus 2A site-directed mutants and naturally occurring "2A-like" sequences. *J Gen Virol* 82:1027–41.

95. Shah AP et al. (2010) Genetic background affects function and intracellular calcium regulation of mouse hearts. *Cardiovasc Res* 87:683–93.

96. Davis J, Maillet M, Miano JM, Molkentin JD (2012) Lost in transgenesis: a user's guide for genetically manipulating the mouse in cardiac research. *Circ Res* 111:761–77.

97. Barnabei MS, Palpant NJ, Metzger JM (2010) Influence of genetic background on ex vivo and in vivo cardiac function in several commonly used inbred mouse strains. *Physiol Genomics* 42A:103–13.

98. Vaillant F et al. (2014) Mouse strain differences in metabolic fluxes and function of ex vivo working hearts. *Am J Physiol Heart Circ Physiol* 306:H78–87.

99. Michael JJ, Tal L, Tardiff JC, Chandra M (2013) Pseudophosphorylation of Cardiac Troponin I Residues 23/24 Decreases Myofilament Ca2+ Sensitivity in Transgenic Mice Containing D230N Mutation in α-Tropomyosin. *Biophys J* 104:482a.

100. Lakdawala NK et al. (2010) Familial dilated cardiomyopathy caused by an alpha-tropomyosin mutation: the distinctive natural history of sarcomeric dilated cardiomyopathy. *J Am Coll Cardiol* 55:320–9.

101. Tardiff JC (2010) Tropomyosin and dilated cardiomyopathy: revenge of the actinomyosin "gatekeeper". *J Am Coll Cardiol* 55:330–2.

102. Preller M, Manstein DJ (2013) Myosin structure, allostery, and mechano-chemistry. *Structure* 21:1911–22.

103. Smith CA, Rayment I (1996) X-ray structure of the magnesium(II).ADP.vanadate complex of the Dictyostelium discoideum myosin motor domain to 1.9 A resolution. *Biochemistry* 35:5404–17.

104. Levitt M, Hirshberg M, Sharon R, Daggett V (1995) Potential energy function and parameters for simulations of the molecular dynamics of proteins and nucleic acids in solution. *Comput Phys Commun* 91:215–231.

105. Schmidt MW et al. (1993) General atomic and molecular electronic structure system. *J Comput Chem* 14:1347–1363.

106. Eswar N et al. (2007) Comparative protein structure modeling using MODELLER. *Curr Protoc Protein Sci* Chapter 2:Unit 2.9.

107. Martí-Renom MA et al. (2000) Comparative protein structure modeling of genes and genomes. *Annu Rev Biophys Biomol Struct* 29:291–325.

108. Sali A, Blundell TL (1993) Comparative protein modelling by satisfaction of spatial restraints. *J Mol Biol* 234:779–815.

109. Fiser A, Do RK, Sali A (2000) Modeling of loops in protein structures. *Protein Sci* 9:1753–73.

110. Beck DA., Daggett V (2004) Methods for molecular dynamics simulations of protein folding/unfolding in solution. *Methods* 34:112–120.

111. Beck DAC, McCully ME, Alonso DOV, Daggett V in lucem Molecular Mechanics (ilmm). Univeristy of Washington, Seattle.

112. Levitt M, Hirshberg M, Sharon R, Laidig KE, Daggett V (1997) Calibration and Testing of a Water Model for Simulation of the Molecular Dynamics of Proteins and Nucleic Acids in Solution. *J Phys Chem B* 101:5051–5061.

113. Kell GS (1967) Precise representation of volume properties of water at one atmosphere. *J Chem Eng Data* 12:66–69.

114. Beck DAC, Armen RS, Daggett V (2005) Cutoff size need not strongly influence molecular dynamics results for solvated polypeptides. *Biochemistry* 44:609–16.

115. Lee B, Richards FM (1971) The interpretation of protein structures: Estimation of static accessibility. *J Mol Biol* 55:379–IN4.

116. Pettersen EF et al. (2004) UCSF Chimera--a visualization system for exploratory research and analysis. *J Comput Chem* 25:1605–12.

117. Racca AW et al. (2013) Contractility and kinetics of human fetal and human adult skeletal muscle. *J Physiol* 591:3049–61.

118. Razumova M V et al. (2006) Effects of the N-terminal domains of myosin binding protein-C in an in vitro motility assay: Evidence for long-lived cross-bridges. *J Biol Chem* 281:35846–54.

119. Margossian SS, Lowey S (1982) Preparation of myosin and its subfragments from rabbit skeletal muscle. *Methods Enzymol* 85 Pt B:55–71.

120. Kron SJ, Toyoshima YY, Uyeda TQ, Spudich JA (1991) Assays for actin sliding movement over myosin-coated surfaces. *Methods Enzymol* 196:399–416.

121. Pardee JD, Spudich JA (1982) Purification of muscle actin. *Methods Enzymol* 85 Pt B:164–81.

122. Potter JD (1982) Preparation of troponin and its subunits. *Methods Enzymol* 85 Pt B:241–63.

123. Kron SJ, Uyeda TQ, Warrick HM, Spudich JA (1991) An approach to reconstituting motility of single myosin molecules. *J Cell Sci Suppl* 14:129–33.

124. Clemmens EW, Entezari M, Martyn DA, Regnier M (2005) Different effects of cardiac versus skeletal muscle regulatory proteins on in vitro measures of actin filament speed and force. *J Physiol* 566:737–46.

125. Gordon AM, LaMadrid MA, Chen Y, Luo Z, Chase PB (1997) Calcium regulation of skeletal muscle thin filament motility in vitro. *Biophys J* 72:1295–307.

126. Cecchini M, Alexeev Y, Karplus M (2010) Pi release from myosin: a simulation analysis of possible pathways. *Structure* 18:458–70.

127. Geeves MA, Holmes KC (1999) Structural mechanism of muscle contraction. *Annu Rev Biochem* 68:687–728.

128. Preller M, Holmes KC (2013) The myosin start-of-power stroke state and how actin binding drives the power stroke. *Cytoskeleton (Hoboken)* 70:651–60.

129. Kintses B et al. (2007) Reversible movement of switch 1 loop of myosin determines actin interaction. *EMBO J* 26:265–74.

130. Naber N, Purcell TJ, Pate E, Cooke R (2007) Dynamics of the Nucleotide Pocket of Myosin Measured by Spin-Labeled Nucleotides. *Biophys J* 92:172–184.

131. Cecchini M, Houdusse A, Karplus M (2008) Allosteric communication in myosin V: from small conformational changes to large directed movements. *PLoS Comput Biol* 4:e1000129.

132. Furch M, Fujita-Becker S, Geeves MA, Holmes KC, Manstein DJ (1999) Role of the salt-bridge between switch-1 and switch-2 of Dictyostelium myosin. *J Mol Biol* 290:797–809.

133. Reubold TF, Eschenburg S, Becker A, Kull FJ, Manstein DJ (2003) A structural model for actin-induced nucleotide release in myosin. *Nat Struct Biol* 10:826–30.

134. Takács B et al. (2011) Myosin cleft closure determines the energetics of the actomyosin interaction. *FASEB J* 25:111–21.

135. Yang Y et al. (2007) Rigor-like structures from muscle myosins reveal key mechanical elements in the transduction pathways of this allosteric motor. *Structure* 15:553–64.

136. Fisher AJ et al. (1995) X-ray structures of the myosin motor domain of Dictyostelium discoideum complexed with MgADP.BeFx and MgADP.AlF4-. *Biochemistry* 34:8960–72.

137. Lorenz M, Holmes KC (2010) The actin-myosin interface. *Proc Natl Acad Sci U S A* 107:12529–34.

138. Behrmann E et al. (2012) Structure of the rigor actin-tropomyosin-myosin complex. *Cell* 150:327–38.

139. Furch M, Geeves MA, Manstein DJ (1998) Modulation of actin affinity and actomyosin adenosine triphosphatase by charge changes in the myosin motor domain. *Biochemistry* 37:6317–26.

140. Joel PB, Trybus KM, Sweeney HL (2001) Two conserved lysines at the 50/20-kDa junction of myosin are necessary for triggering actin activation. *J Biol Chem* 276:2998–3003.

141. Joel PB, Sweeney HL, Trybus KM (2003) Addition of lysines to the 50/20 kDa junction of myosin strengthens weak binding to actin without affecting the maximum ATPase activity. *Biochemistry* 42:9160–6.

142. Beck DAC, Alonso DO V, Inoyama D, Daggett V (2008) The intrinsic conformational propensities of the 20 naturally occurring amino acids and reflection of these propensities in proteins. *Proc Natl Acad Sci U S A* 105:12259–12264.

143. Homsher E, Wang F, Sellers JR (1992) Factors affecting movement of F-actin filaments propelled by skeletal muscle heavy meromyosin. *Am J Physiol* 262:C714–23.

144. Lundy SD et al. (2014) Cell-based Delivery of dATP Via Gap Junctions Enhances Cardiac Contractility. *J Mol Cell Cardiol*.

145. Wang S, Wolynes PG (2012) Active contractility in actomyosin networks. *Proc Natl Acad Sci U S A* 109:6446–51.

146. Campbell SG, Lionetti F V, Campbell KS, McCulloch AD (2010) Coupling of adjacent tropomyosins enhances cross-bridge-mediated cooperative activation in a markov model of the cardiac thin filament. *Biophys J* 98:2254–64.

147. Walsh R, Rutland C, Thomas R, Loughna S (2010) Cardiomyopathy: a systematic review of disease-causing mutations in myosin heavy chain 7 and their phenotypic manifestations. *Cardiology* 115:49–60.

148. Tyska MJ et al. (2000) Single-molecule mechanics of R403Q cardiac myosin isolated from the mouse model of familial hypertrophic cardiomyopathy. *Circ Res* 86:737–744.

149. Rayment I, Holden HM, Sellers JR, Fananapazir L, Epstein ND (1995) Structural interpretation of the mutations in the beta-cardiac myosin that have been implicated in familial hypertrophic cardiomyopathy. *Proc Natl Acad Sci U S A* 92:3864–3868.

150. Lowey S, Bretton V, Gulick J, Robbins J, Trybus KM (2013) Transgenic mouse α- and β-cardiac myosins containing the R403Q mutation show isoform-dependent transient kinetic differences. *J Biol Chem* 288:14780–7.

151. Moore JR, Leinwand L, Warshaw DM (2012) Understanding Cardiomyopathy Phenotypes Based on the Functional Impact of Mutations in the Myosin Motor. *Circ Res* 111:375–385.

152. Geisterfer-Lowrance AAT, Kass S, Tanigawa G (1990) A molecular basis for familial hypertrophic cardiomyopathy: a β cardiac myosin heavy chain gene missense mutation. *Cell* 62:999–1006.

153. Lankford EB, Epstein ND, Fananapazir L, Sweeney HL (1995) Abnormal contractile properties of muscle fibers expressing beta-myosin heavy chain gene mutations in patients with hypertrophic cardiomyopathy. *J Clin Invest* 95:1409–14.

154. Cuda G, Fananapazir L, Zhu WS, Sellers JR, Epstein ND (1993) Skeletal muscle expression and abnormal function of beta-myosin in hypertrophic cardiomyopathy. *J Clin Invest* 91:2861–5.

155. Sata M, Ikebe M (1996) Functional analysis of the mutations in the human cardiac beta-myosin that are responsible for familial hypertrophic cardiomyopathy. Implication for the clinical outcome. *J Clin Invest* 98:2866–73.

156. Bromley D, Anderson PC, Daggett V (2013) Structural consequences of mutations to the α-tocopherol transfer protein associated with the neurodegenerative disease ataxia with vitamin E deficiency. *Biochemistry* 52:4264–73.

157. Galderisi M et al. (2011) Recommendations of the European Association of Echocardiography: how to use echo-Doppler in clinical trials: different modalities for different purposes. *Eur J Echocardiogr* 12:339–53.

158. William Humphrey, Andrew Dalke, Klaus Schulten (1996) VMD – Visual Molecular Dynamics. *J Mol Graph* 14:33–38.

159. Eargle J, Wright D, Luthey-Schulten Z (2006) Multiple Alignment of protein structures and sequences for VMD. *Bioinformatics* 22:504–506.